UNIVERSIDADE DE SÃO PAULO
FFCLRP - DEPARTAMENTO DE FÍSICA
PROGRAMA DE PÓS-GRADUAÇÃO EM FÍSICA APLICADA A MEDICINA E BIOLOGIA

Estudos de técnicas ultrassônicas para análise de propriedades mecânicas de meios viscoelásticos

Theo Zeferino Pavan

RIBEIRÃO PRETO
2011

Theo Zeferino Pavan

Estudos de técnicas ultrassônicas para análise de propriedades mecânicas de meios viscoelásticos

Tese apresentada ao Departamento de Física da Faculdade de Filosofia Ciências e Letras de Ribeirão Preto para obtenção do título de Doutor em Ciências - Versão Corrigida

Orientador: Prof. Dr. Antonio Adilton Oliveira Carneiro

UNIVERSIDADE DE SÃO PAULO
PROGRAMA DE PÓS-GRADUAÇÃO: FÍSICA APLICADA A MEDICINA E BIOLOGIA

Ribeirão Preto

2011

FICHA CATALOGRÁFICA

Pavan, Theo Zeferino

Estudos de técnicas ultrassônicas para análise de propriedades mecânicas de meios viscoelásticos / Theo Zeferino Pavan ;
orientador Antonio Adilton Oliveira Carneiro- Ribeirão Preto, 2011.

111 p.: il.

Tese (Doutorado) - Universidade de São Paulo, 2011

1 - Ultrassom 2 - Elastografia 3 - Força de radiação acústica

4 - Viscoelasticidade 5 - Não-linearidade elástica

Dedico esta tese aos meus pais, José Geraldo Pavan e Narcisa Zeferino Pavan e à minha irmã, Tati Zeferino Pavan que são pessoas muito especiais e meus principais inspiradores e motivadores.

Agradecimentos

Em virtude de ter sido um trabalho de doutorado realizado em duas instituições, muitas pessoas importantes se fizeram presentes e são dignas de meus agradecimentos.

Inicialmente, agradeço ao meu orientador, professor Antonio Adilton O. Carneiro, grande mestre e incentivador desde que começamos a trabalhar juntos, no início de 2004. Poderia citar inúmeros acontecimentos em que o professor Adilton foi de singular importância. Cito duas passagens, uma no inicio e outra no final desse trabalho. A primeira aconteceu no final do meu curso de graduação, quando foi ele o principal entusiasta para que eu me aventurasse em um programa de doutorado direto. A segunda ocorreu quando ele me incentivou a redigir a tese em inglês, um enorme desafio, mas ao mesmo tempo uma grande oportunidade para evolução científica, mesmo tendo sido eu informado por todos que isso não seria possível. Mesmo assim ele decidiu me apoiar e tentar tudo que fosse possível.

Ao professor Timothy Jon Hall, por ter não somente aberto as portas de seu laboratório, na *University of Wisconsin*, Madison, EUA, mas também por ter realmente me orientado durante o período de doutorado *sandwich*. Durante minha estada na universidade, ele me propôs idéias, discutiu comigo experimentos e resultados, além de ter contribuído de maneira expressiva na redação de trabalhos científicos. Foi realmente uma honra ter trabalhado com o professor Tim durante esse período.

Ao professor Ernest L. Madsen, que foi uma pessoa de fundamental importância para a realização do trabalho nos EUA. Sem o seu apoio, não tenho dúvidas de que não teria sido possível realizar todo o trabalho descrito nos capítulos 2 e 3. Pude realmente aprender muito trabalhando em conjunto com o professor Ernie. Ele possui vasta experiência nos temas relacionados ao ultrassom e à construção de phantoms, além de ser uma pessoa “mão na massa” ou como dizem os americanos, *hands on it*. Foi para mim uma grande experiência conviver esse tempo com ele.

Ao professor Jim Zagzebski, pelas discussões científicas e pela oportunidade de acompanhar uma das disciplinas que ele ministrou no curso de pós-graduação em *Medical Physics*.

Ao professor Tomy Varghese, pelas discussões científicas.

Aos professores que participaram da banca da minha qualificação, Eder R. Moraes, Luiz Otávio Murta Jr. e Glauber Tomaz da Silva, pelas orientações e sugestões.

Aos amigos do laboratório GIIMUS, Baggio, Hermes, Thiago, Ebenezer, Tenysson, Marden, Raimundo, Rogério, Silvio, Alexandre, Larissa, Michelle, Marcelo e Diego, pelas valiosas discussões científicas e pelos momentos de descontração.

Aos amigos do *Ultrasoud lab.* em Madison, Matt McCormick, Matt Bayer, Ryan, Nick, Hao, Hayan, Lee, Kibo, Shyam, Amy, Lisa, Theresa, Janelle e Ted, pelas valiosas discussões científicas, pelos momentos de descontração e pela oportunidade de trocar experiências e cultura. Essa convivência com pessoas de tão diferentes de lugares, distantes entre si, mas todos com os mesmos objetivos, é algo que não tem preço.

A todos os amigos que estiveram presentes em minha vida durante essa caminhada. Precisaria de muito espaço para citar o nome de todos e correria o risco de esquecer alguém. Todos são muito especiais.

Aos amigos que conheci durante minha estada nos EUA. Todos tiveram muita importância na minha vida durante essa fase. Todos os que já estiveram por um tempo no exterior sabem que, geralmente, a comunidade brasileira local, junto com os agregados, é muito unida e forma um grupo grande de pessoas. Personifico o nome de todos na pessoa do Miller, que foi meu *roommate* durante quase todo o período que estive por lá e que acabou tornando-se um grande amigo.

Aos técnicos, Serginho, Aziane, Lourenço e Agnelo, pela ajuda nos procedimentos e montagens experimentais, além dos momentos de descontração.

Ao técnico Gary Frank, pela ajuda nos procedimentos experimentais, além de ensinamentos sobre ensaios mecânicos e sobre como construir os phantoms. E claro, pelas divertidas conversas nos corredores do departamento.

Ao cientista J.J., pelos ensinamentos sobre o processamento de imagens elastográficas e sobre simulação por elementos finitos.

Ao amigo Walfred Tedeschi, com quem não convivi durante o trabalho de doutorado, mas que foi de fundamental importância na minha formação científica, durante a graduação.

À Nilza, pela paciência em explicar os procedimentos burocráticos da Universidade.

À Beth Bierman e à Mary Wegner do *Department of Medical Physics* da *University of Wisconsin*, que me auxiliaram na parte burocrática da viagem aos EUA.

Ao professor Alexandre S. Martinez, pelo valioso auxílio no pedido da bolsa de doutorado

sandwich junto à CAPES.

À FAPESP, pela bolsa de doutorado direto concedida e pelas verbas para pesquisa, à CAPES pela bolsa de doutorado *sandwich* concedida e pelas verbas para pesquisa, ao CNPq pelas verbas para pesquisa. Quero agradecer aqui, novamente, ao professor Tim Hall, pelo auxílio financeiro nos últimos três meses que permaneci nos EUA.

Por fim, agradeço aos meus pais José Geraldo e Narcisa e à minha irmã Tati, que sempre foram meus maiores incentivadores. Esse trabalho teria menos sentido se não fosse pela presença deles em minha vida.

Resumo

Mudanças nas características mecânicas de tecidos biológicos geralmente estão relacionadas com algum tipo de patologia. Técnicas de imagens elastográficas são métodos quantitativos de se estimar as propriedades mecânicas de tecidos. Em geral, o objetivo destas técnicas de imagem é medir o movimento do tecido provocado por uma força interna ou externa. Por meio desse movimento, parâmetros viscoelásticos do meio em análise são reconstruídos. A força de excitação pode ser tanto quasi-estática, como dinâmica. O trabalho apresentado nesta tese aborda as técnicas de elastografia dinâmica e quasi-estática. Na abordagem quasi-estática, a elasticidade não-linear é estudada através de *phantoms* com características que simulam as do tecido humano. Na abordagem dinâmica, o movimento dinâmico promovido por força de radiação acústica é avaliado através de técnicas ultrassônicas e magnéticas. O comportamento elástico não-linear de materiais utilizados em *phantoms* para elastografia foi analisado através de ensaios mecânicos. Esses materiais foram projetados para apresentarem uma relação tensão/deformação que não dependesse do módulo de cisalhamento para pequenas deformações. Os materiais são compostos de misturas de agar e gelatina. Dispersão de óleo possibilitou um maior controle da não-linearidade e do módulo de cisalhamento. Esses materiais foram projetados para serem usados em *phantoms* com configurações heterogêneas. O esfeito da não-linearidade elástica dos materiais sobre o contraste, a relação sinal ruído e a relação contraste ruído de imagens elastográficas de um *phantom* contendo inclusões esféricas, sofrendo altas deformações (até 20%) foi investigada. As variações de contraste, para altas deformações, foram comparadas com resultados previstos por simulações de elementos finitos. Concluímos que *phantoms* para se avaliar a não-linearidade elástica são relativamente fáceis de serem produzidos, sendo que suas propriedades mecânicas podem ser antecipadas. Foi demonstrada a viabilidade de se medir movimentos vibratórios induzidos por feixes acústicos confocais através de um ultrassom Doppler de ondas contínuas. A interferência de feixes de ultrassom com pequena diferença de frequência provoca o aparecimento de uma força dinâmica no alvo. Foram obtidas imagens de uma esfera rígida imersa em um *phantom* viscoelástico, através da varredura de ambos os transdutores (confocal e Doppler) pelo plano focal do transdutor confocal. O comportamento dinâmico de uma esfera magnetizada induzido por força de radiação acústica foi medido através de um sensor magnetoresistivo. A Lei de Stokes para movimentos oscilatórios, considerando números de Reynolds de pequena magnitude, foi adotada para modelar a força de arraste. A partir da nova posição de equilíbrio em resposta à força de radiação de longa duração (poucos segundos), a amplitude dessa força foi estimada. Para se estimar a viscosidade da água, o movimento da esfera foi ajustado a um modelo de movimento-harmônico amortecido. Baseando-se nesses resultados os perfis de movimento calculados teoricamente tiveram boa concordância com os movimentos experimentais medidos quando a esfera foi deslocada por pulsos de força de radiação acústica de curta duração. O movimento de uma esfera rígida imersa em um *phantom* feito de gelatina, deslocada por força de radiação acústica, foi avaliado por meio de ecos ultrassônics obtidos com um sistema pulso/eco. A teoria utilizada para se estimar os parâmetros viscoelásticos do *phantom*, usando o movimento induzido na esfera, é uma extensão da teoria usada para se estimar a viscosidade da água.

Abstract

Changes in the mechanical properties of soft tissues may be related with pathological disorders. Elasticity imaging is a quantitative method of estimating the mechanical properties of the tissue. In general, the aim of this technique is to measure tissue motion caused by an external or internal force and use it to reconstruct the viscoelastic parameters of the medium. The excitation stress used can be (quasi-)static or dynamic. Both elastographic approaches are explored in this thesis work. In the quasi-static approach, the nonlinear elasticity is studied through tissue-mimicking phantom experiments. In the dynamic approach, the dynamic motion provided through acoustic radiation force is evaluated using ultrasonic and magnetic techniques. The development of phantom materials for elasticity imaging is reported. These materials were specifically designed to provide nonlinear stress/strain relationship that can be controlled independently of the small strain shear modulus of the material. The materials are mixtures of agar and gelatin gels. Oil droplet dispersions in these materials provide further control of the small strain shear modulus and the nonlinear parameter of the material. The Veronda-Westman model for strain energy density provided a good fit to all materials used in this study. These materials were designed for use in elastography phantoms where heterogeneous configurations are employed. The effects of phantom materials nonlinearity over the strain contrast, signal-to-noise ratio and contrast-to-noise ratio of a phantom containing spherical inclusions undergoing large deformations (up to 20%) were investigated. Each of the phantom background and inclusions materials has distinct small-strain shear modulus and nonlinear mechanical behavior. The changes in contrast over a large deformation range predicted by nonlinear FEA simulations were compared with that experimentally observed. This work illustrates that nonlinear elasticity phantoms are relatively easy to manufacture and their mechanical properties can be predicted. The feasibility of measuring vibration movement, through a mono-channel continuous wave Doppler system, induced by focused confocal beams, is demonstrated. The interference of two ultrasonic beams promotes a dynamic force to the target. The ability to form images of a rigid spherical inhomogeneity embedded in viscoelastic phantom by scanning both ultrasonic transducers (confocal and Doppler) across the confocal transducer focal plane is presented. The dynamic behavior of a rigid magnetic sphere induced by an acoustic radiation force was investigated. The drag force acting on the sphere during its motion was considered to follow a modified Stokes law for a low Reynolds number, accounting for phenomena related to its oscillatory movement. The movement of the magnetic sphere was tracked using a magnetoresistive sensor. From the new equilibrium position of the sphere in response to the long-duration (few seconds) static radiation force, the amplitude of this force was estimated. To access the water viscosity, the sphere movement was fitted to a harmonic-motion model. Based on the results for the acoustic force and water viscosity, a theoretical profile of the sphere displacement as a function of time due to short-duration acoustic radiation force agreed well with experimental results. The motion of a rigid sphere embedded in gelatin phantom, displaced by acoustic radiation force, was evaluated using the ultrasonic echoes from a pulse-echo system. The theory used to estimate the viscoelastic parameters of the phantom, from the oscillation of the rigid sphere is an extension of the relation used to estimate the water viscosity.

Contents

List of Figures

List of Tables

List of Abbreviations

AM	Amplitude Modulated
ARFI	Acoustic Radiation Force Impulse
CC	Cross-Correlation
CNR	Contrast-to-Noise Ratio
CW	Continuous Wave
DMA	Dynamic Mechanical Analysis
FEA	Finite Element Analysis
FWHM	Full Width at Half Maximum
GIIMUS	Grupo de Inovação em Intrumentação Médica e Ultrassom
HMI	Harmonic Motion Imaging
IDC	Infiltrating Ductal Carcinoma
MRI	Magnetic Resonance Imaging
NCC	Normalized Cross-Correlation
PRF	Pulse Repetition Frequency
PSF	Point Spread Function
RF	Radiofrequency
ROI	Region Of Interest
SNR	Signal-to-Noise Ratio

1 Introduction

Changes in the mechanical properties of soft tissues may be related with pathological disorders, i.e, breast tumors as fibroadenomas and carcinomas present viscoelastics properties that differs from that of the surrounding healthy tissue, i.e, glandular tissue and fat. Palpation of soft tissue's surface in order to detect abnormalities is a procedure being used for many years. Palpation of breast and prostate are two well known examples. However, when the abnormality lies deep beneath the surface or if is too small, palpation may not be efficient.

In Brazil, breast cancer is the number one cancer-related death among women population [1]. Mammography is a widespread procedure for detecting breast lesions. Improvements in this diagnostic modality have allowed better detectbility of small lesions when compared to either clinical or self palpation [2]. However, there are works reporting on a breast cancer undetectability between 10% to 15% by the mammography exam [3]. These lesions may still be indentified through ultrasound [3].

Elasticity imaging is a quantitative method for estimating the mechanical properties of the tissue and have been developing rapidly over the last 20 years. In general, the aim of this technique is to measure tissue motion caused by an external or internal force, and use it to reconstruct the viscoelastic parameters of the tissue. Magnetic resonance [4] and ultrasound [5] are commonly employed to detect this motion. The elasticity imaging approaches can be classified according to the excitation stress used. It can be either (quasi-) static or dynamic. The diagram shown in figure 1.1 illustrates the different methods for estimating the elastic properties of the tissue using ultrasound, classified based upon the employed excitation stress. Highlighted are the two elastographic approaches explored in this thesis; strain image and approaches using acoustic radiation force excitation.

The timeline evolution of the major elastographic imaging modalities, presented in this chapter, is shown in figure 1.2.

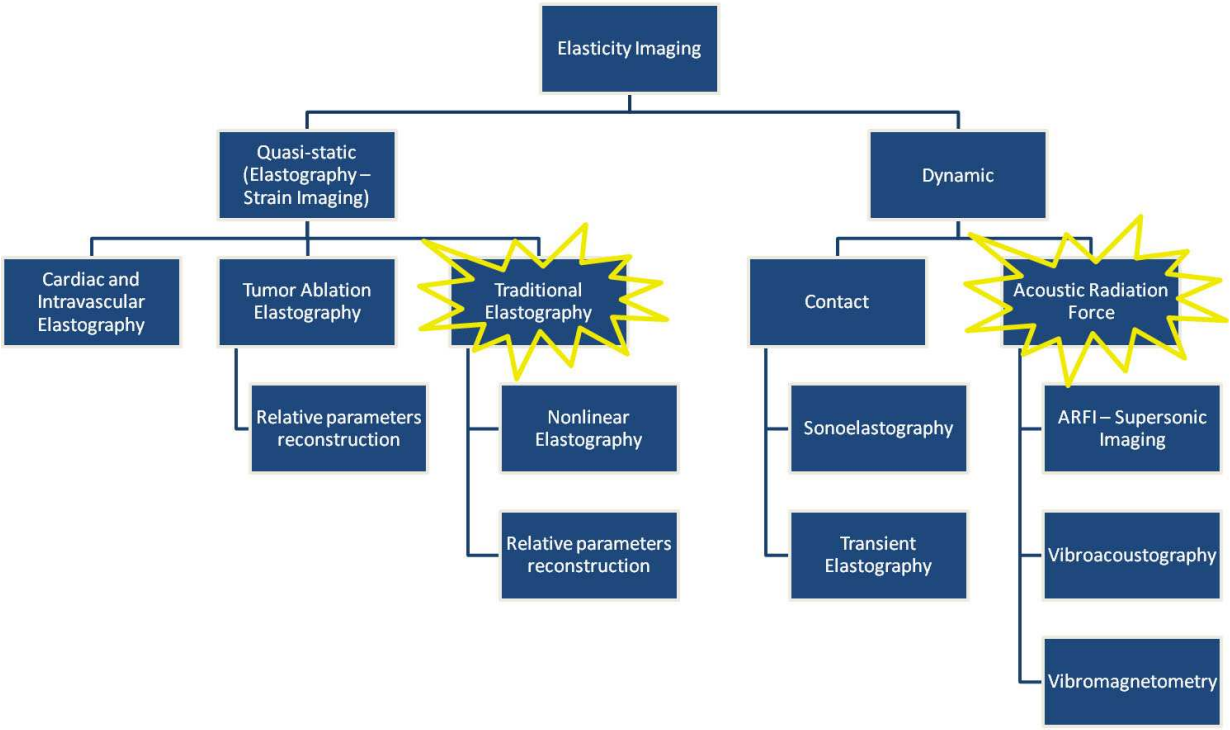

Figure 1.1: Elasticity imaging by ultrasound techniques classified according to the type of excitation stress applied to the medium being investigated. The highlighted categories are explored throughout the thesis.

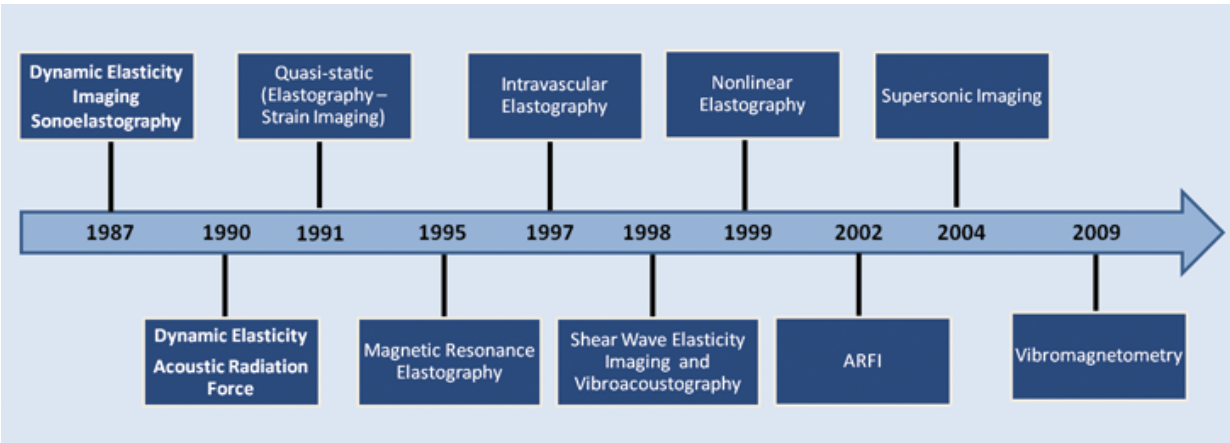

Figure 1.2: Over twenty years timeline showing the elasticity imaging evolution. Some of the well known elastographic approaches are shown. This introduction has a brief description of each category.

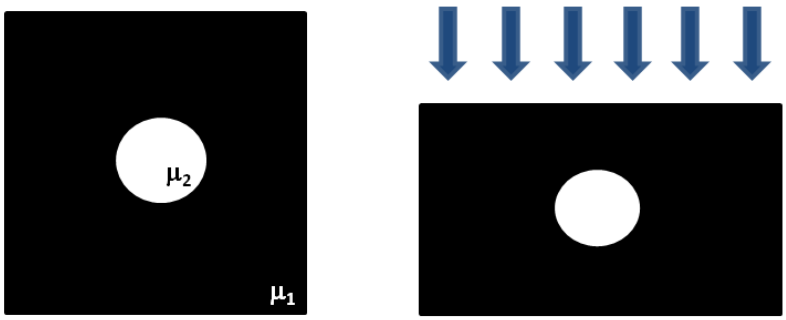

Figure 1.3: Depiction of the heterogeneous soft medium, with a circular inclusion, being deformed by a static external compression.

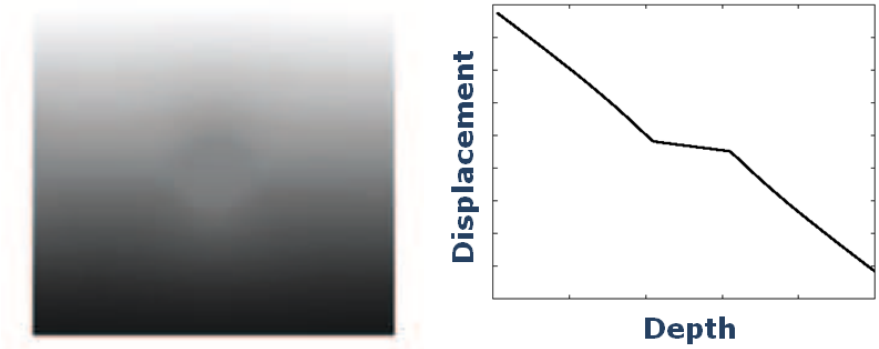

(a) (b)

Figure 1.4: Simulated displacement of the heterogeneous medium, where the inclusion is stiffer than the background. (a) Displacement map. (b) Displacement profile representing the central vertical line of the image.

1.1 Quasi-static elasticity imaging

Quasi-static elasticity imaging was first introduced by Ophir et al. [6], they named this modality as elastography which also became known as strain imaging. In elastography, a small deformation (usually <5%) is applied, either through an external compressor or physiologic function (breathing, cardiac, etc...). Anatomic maps are acquired before and after the deformation and the displacement map of the deformed tissue is estimated by comparing pairs of maps. The mechanical strain is estimated calculating the gradient of the displacement.

Consider an heterogeneous soft medium, where the background elastic shear modulus (μ_1) is different than that of the inclusion (μ_2). This medium experiences an external compression and deforms, as shown in figure 1.3. The displacement map obtained after applying 1% of compression, calculated via Finite Elements Method is shown in figure 1.4(a). The profile of the displacement image is shown in figure 1.4(b). In this simulation, the inclusion is stiffer than the background ($\mu_2 > \mu_1$).

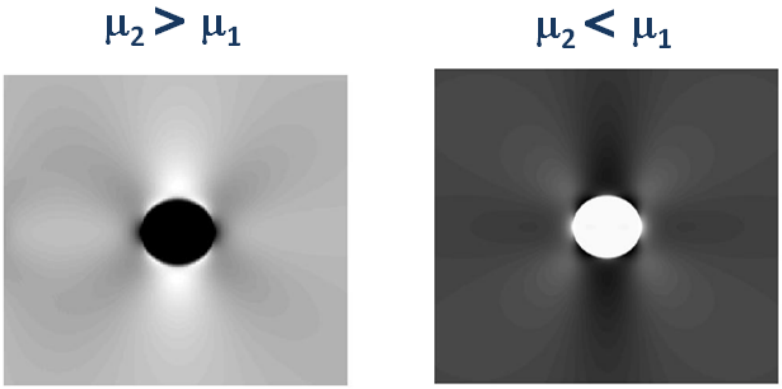

(a) (b)

Figure 1.5: Strain experienced by the heterogeneous medium obtained from the gradient of simulated displacement field. (a) Inclusion stiffer than the background. (b) Inclusion softer than the background.

The strain can be defined as the spatial gradient of the displacement, which is the slope of the displacement curve. From the plot in figure 1.4(b) we observe that the slope is different for materials presenting different elastic moduli. Consequently, the strain field values will be proportional to the stiffness as is shown in figure 1.5. Usually, when the strain image (or elastogram) is represented in grayscale, brighter colors represent higher strains.

When using ultrasound, the pre and post-deformed echo maps (or radiofrequency (RF) maps) can be compared, to estimate the displacement, via time-delay techniques. cross-correlation is a well known example, and was the first time-delay estimator to be used to correlate ultrasound echo data [7]. The normalized form of this algorithm (normalized cross-correlation (NCC)) is an efficient and precise algorithm; however, very time consuming [8]. Sum squared differences and sum absolute differences are other wildly used time-delay estimators. Block-matching (template-matching) algorithms have been used to improve the signal-to-noise ratio as an attempt of achieving good-quality real time strain images [9]. The 2-D block matching algorithm uses the output of a time-delay technique computed between a pair of RF maps for a rectangular kernel over a search region. The location where the time-delay output shows maximum correlation is considered to be the displaced position of the kernel between the post and pre-deformed pair of frames.

Figure 1.6 depicts a tissue mimicking phantom with a spherical inclusion. To generate the elastographic image of this phantom, echoes were acquired before and after a compression applied with the ultrasound transducer placed on the top part of the phantom. The pairs of RF data was processed using the cross-correlation mathematical metric via block-matching algorithm to determine the displacement field. Local axial strain was calculated applying a linear regression

to the displacement data. The estimated local strain is the slope of the linear regression curve. This elastographic image was generated applying 2.5% of deformation.

Inverse elasticity solutions to achieve relative elastic constants (i.e., Young's modulus and Poisson's ratio) distribution based on analytical and simulated approaches have been reported [10, 11, 12]. Imaging these intrinsic material properties of the tissue may provide additional information and have fewer artifacts than the strain image used to produce it; additionally, being generally easier to be interpreted [13].

Traditional elastography, where the motion is induced by a compression of the the ultrasound transducer against the body, has been shown to have successful results since the early developments of this technique, in muscle [14], prostate [15] and breast [16]. Monitoring myocardial mechanical properties during cardiac cycle could be important to early detection of cardiac abnormalities. In this case, the movement of the heart is used to determine the strain [17]. The same idea has been used to determine vessel strain through intravascular ultrasound RF data, where the motion is caused by the arterial contraction [18]. Another application of quasi-static elasticity, is to monitoring the stiffness change of the liver tissue during RF tumor ablation [19]. In this modality, the electrode is placed into the area of tissue to be ablated. In this elastographic approach, the displacement induced by the electrode movement is estimated. Inverse approaches to obtain the relative Young's modulus distribution have also been reported for this application [20].

1.1.1 Nonlinear elastography

Most of strain imaging involves deformations of up to 5% which is a region of nearly linear behavior. However, when the compression becomes large enough most human tissues present a significantly nonlinear stress/strain relationship [21, 22, 23].

Figure 1.7 shows a graph of stress/strain data of different breast tissues and tumors, adapted from the work of Wellmann [23]. The samples were evaluated through push indentation test, applying up to 10% of compression. This data show that fatty tissue behavior was more linear with applied strain than glandular tissue, benign (Fibroadenoma), and malignant tumor (Infiltrating ductal carcinoma). Among the analysed tissues, the Infiltrating ductal carcinoma (IDC) tumor presented the most evident nonlinear behavior, meaning that the increase in stiffness with applied compression was more pronounced. These results were in agreement with the results presented by Krouskop et al. [21]. In this work they measured the Young's modulus of breast tissues pre-compressing the samples of 1% and 20%. The percentual change in stiffnes in their case was also larger for the malignant tissue and lower for fat. They found differences in the

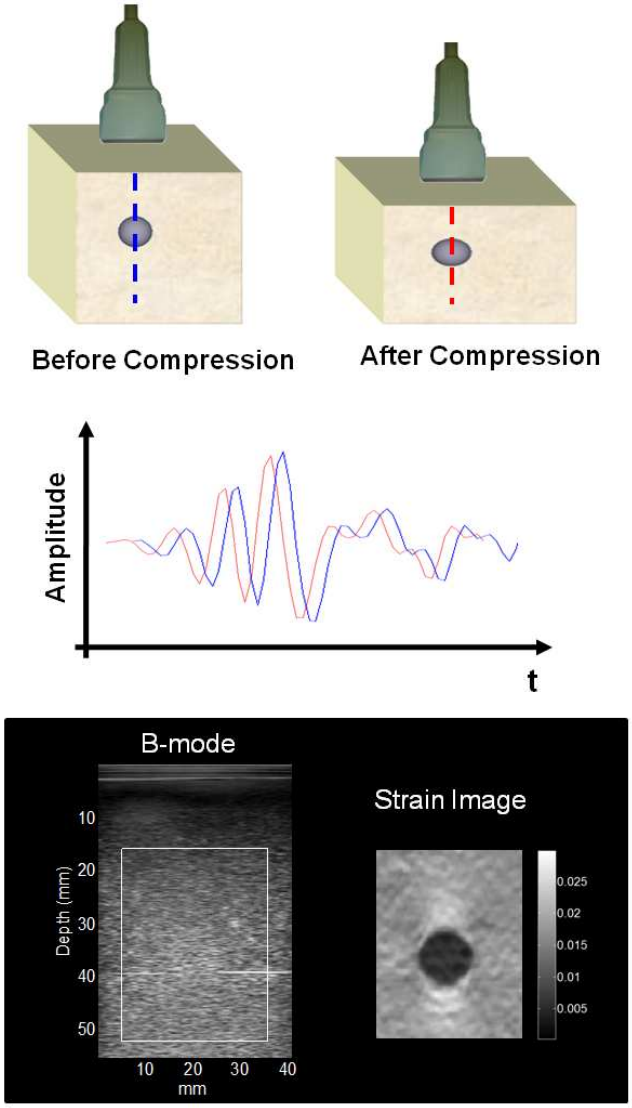

Figure 1.6: Procedure of the signal acquisition to elastographic image formation. The top part represents a pre and post-compression tissue mimicking phantom with an internal spherical inclusion stiffer than the background. The middle part represents a pre-deformation (blue line) and a post-deformation (red line) echo signals segments. The post-deformation data is phase shifted when compared to the pre-deformation echo. At the bottom, a B-mode and a strain image from the phantom are shown. In these images, the inclusion backscatter properties are similar to the background, resulting in a B-mode where the inclusion is barely visualized. On the other hand, the strain image had a good inclusion/background contrast.

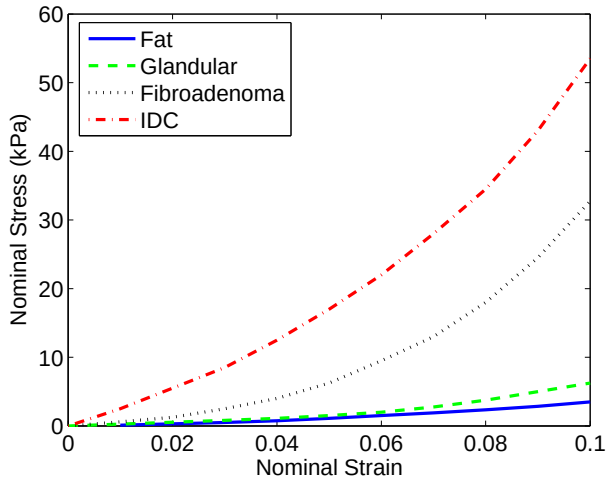

Figure 1.7: Stress/strain data adapted from the work of Wellman [23] for different types of breast tissues.

nonlinear behavior for prostate tissues as well.

Tissue nonlinear behavior may affect on the strain contrast of elastographic images when larger deformations are allowed. Hall et al. [24] observed deformation-dependent strain image contrast while performing *in vivo* breast elasticity imaging and conjectured that this changing contrast could be explained with differences in the elastic nonlinearity of the composite tissues. Change in strain-contrast of benign and malignant tumors for different amount of compression was observed.

Reconstructing tissue's nonlinear parameters distribution based on strain energy functions could enhance the capability of differentiating tumors. These nonlinear parameters arise from hyperelastic constitutive equations, which are based on strain energy functions. The energy functions, usually, are presented in exponential or polynomial form. Examples of hyperelastic models are: neo-Hookean, Mooney-Rivlin [25], Ogden [26], Yeoh [27], Veronda-Westmann [28], and Arruda-Boyce [29]. The efficiency of some of these models to fit breast tissues stress/strain data was verified by O'Hagan and Samani [30]. The Veronda-Westmann was adopted to fit stress/strain data of elastophraphy phantom materials [31]. The insights provided by this study are the basis for stable elastography phantoms with stiffness and nonlinear stress/strain relationships in the background that differ from those in the target. Chapter 2 of this thesis gives a more detailed description about the mechanical tests and hyperelastic modeling of the materials used to manufacture phantoms. The nonlinear elasticity phantom construction, and how the nonlinear behavior affects the strain image contrast with applied compression are presented in chapter 3.

Approaches that take advantage of the strain stiffening properties to improve elastography

image interpretation have been reported [32, 33, 34].

1.2 Dynamic elasticity imaging

Dynamic elasticity imaging can be classified by the excitation displacement source, which can be by contact or by remote acoustic radiation force. Sonoelastography [35] is a contact technique where an external source induces low-frequency (1Hz - 1kHz) vibrations in the tissue and the amplitude and phase of the resulting shear wave is measured through Doppler ultrasound. Transient elastography [36] is a technique where a point source vibrator generates a pulsed force on the tissue surface. The transient compressional and shear waves are then evaluated through ultrasound echoes and cross-correlation algorithm.

Sugimoto et al. [37] proposed the first attempt to detecting movement induced by acoustic radiation force to characterizing biological tissues. Several works adopting acoustic remote force and ultrasound detection to characterizing elastic behavior of materials were published since then.

1.2.1 Acoustic radiation force impulse (ARFI) imaging

Nightingale et al. [38] proposed the acoustic radiation force impulse (ARFI) technique, where the remote force is promoted through short duration ($<$1ms) acoustic radiation pulses, using conventional scanner array, to generate localized displacements in the tissue. The displacements are tracked via ultrasonic correlation-based methods within a region of interest using the same array transducer employed to generate the acoustic radiation force. Spatial and temporal response of the medium, to the applied force, are related to its mechanical characteristics. The displacement magnitude is inversely proportional to the local tissue stiffness and is typically on the order of few micrometers [38]. The volume of the region of interest, in the tissue, where the radiation force is applied is determined by the focal characteristics of the ultrasonic transducer employed.

ARFI image is generated using several pushing locations and tracking the displacement versus time along the A-line corresponding to the focus location of the pushing beams. The data obtained from the tissue maximum displacement, the time taken to reach its peak displacement and the recovery velocity can be used to form the ARFI image [38].

B-mode, elastogram and ARFI images of an anthropomorphic breast phantom [39] is shown in Figure 1.8. Inclusions mimicking fat (softer than the background) and fibroadenoma (stiffer

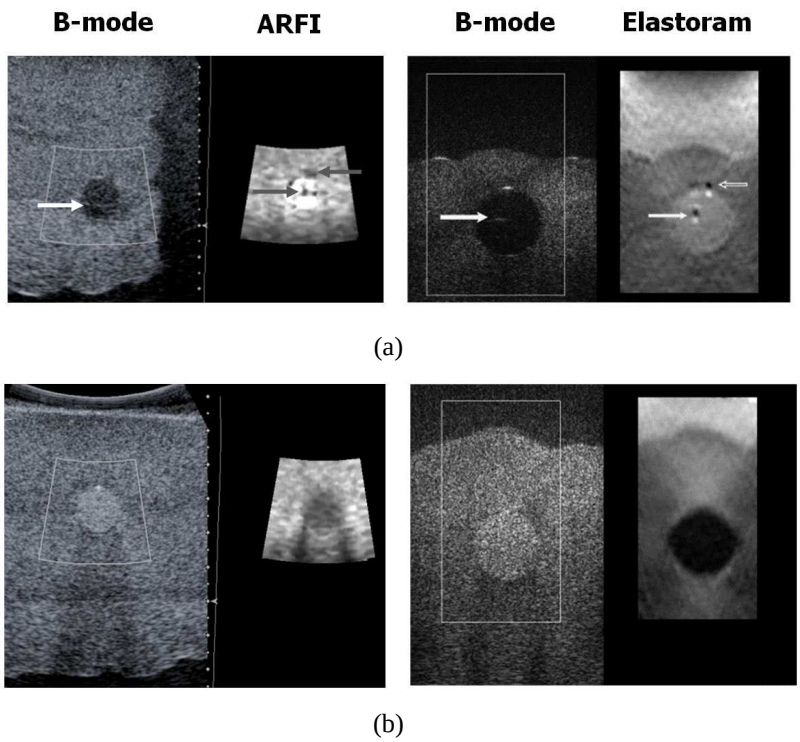

Figure 1.8: Elasticity and B-mode images obtained from the anthropomorphic breast phantom. Left: B-mode and ARFI images. Right: B-mode and elastogram. Inclusions mimicking (a) fat and (b) fibroadenoma. For a more complete description of the phantom construction and the strain image estimation, the reader is referred to Ref. [39]

than the background) are shown in figure 1.8(a) and figure 1.8(b), respectively. To generate the elastograms, the phantom was compressed of 1% of the phantom height and the displacements were estimated through a 2-D modified block-matching algorithm [9]. The RF data was aquired using a SONOLINE ™ Antares (Siemens Medical Solutions Icn., Mountain View, CA) ultrasound scanner. The ARFI images were obtained with the Acuson S2000 ultrasound system (Siemens Medical Solutions Icn., Mountain View, CA) using the implementation of ARFI to the system. For a more complete description of the phantom construction and the strain image estimation, the reader is referred to Ref. [39].

ARFI and strain images, in both cases, show, overall, similar features. Even some artifacts caused by echo signal decorrelation, due to specular reflection, appearing in the elastogram (solid arrow) can be visualized in the the ARFI image (figure 1.8(a)). No comparison about the image quality can be made in this case, since the data used to create the strain images were processed offline [39], while the ARFI images were obtained in quasi-real time manner. The system takes few milliseconds to display the ARFI image.

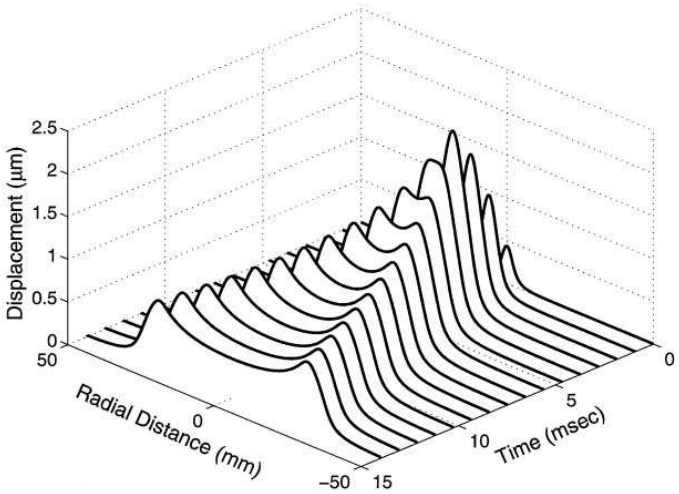

Figure 1.9: Simulated time evolution of the shear displacement along the radial position. Plot originally appeared in Ref. [40], Fig. 13(b).

1.2.2 Shear wave elasticity imaging (SWEI)

Focused acoustic radiation force generates shear waves which travels along the medium perpendicularly to the applied force. The displacement increases initially in time, after the exciting ultrasonic pulse had arrived at the focal area, and starts to decay, due to the formation of a cylindrical wave propagating away from the axis of excitation [40]. Estimating the velocity and attenuation of these shear waves are ways of estimating the medium elasticity [40, 41]. Spatially monitoring the shear wave speed along the tissue is a force-independent technique for reconstructing the shear moduli; consequently, obtaining images representing absolute values for the elasticity. Sarvazyan et al. [40] explored the possible modalities for generating and tracking these shear waves. They, theoretically, evaluated the profile and characteristics of the wave propagation in soft medium and compared to experimental results. Simulated displacement in a elastic medium, obtained by Sarvazyan et al. ([40], Fig. 13(b)), due to the shear wave propagation is shown in figure 1.9.

Modulated acoustic radiation force can generate narrowband low-frequency shear waves. Shear wave speed measured at different frequencies can be fitted to a viscoelastic model i.e., Voigt model. Measuring the frequency dependence of the speed and the attenuation of shear waves, generated by pulsed static radiation force, can also be used to estimate shear elasticity for a range of frequencies [42].

1.2.3 Supersonic shear imaging

Bercoff et al. [43] proposed the supersonic shear imaging, where the acoustic force is generated by an array transducer promoting the dispersion of shear waves in the medium, as discussed in section 1.2.2. The innovation of their method is that the shear source creates successively focused pushing beams at different depths. Consider that speed of the moving source is greater than the induced shear waves speed, a phenomenon similar to the sonic "boom" created by a supersonic aircraft appear in the soft tissue [44]. All resulting shear waves interfere constructively along a Mach cone, creating two plane and intense shear waves propagating in opposite directions.

To track the shear waves propagation, which frequency is usually around 300Hz, they use a ultrafast frame rate scanner. In this beamforming approach, all elements composing the transducer should emit the ultrasound waves at the same time, forming a transmitted plane wave. The image is then formed by weighting and geometric correcting the received echoes, achieving frame rates up to 10k frames/second. More detailed explanation can be found, for example, in Ref. [45]. Imaging the shear waves along time enables recovering information about the medium elasticity, and via inversion algorithms, to form images corresponding to the tissue elasticity absolute values distribution [43].

1.2.4 Vibroacoustography

The vibration caused by tapping an object emits a sound, which depends on the object's mechanical properties. Based on this idea, Fatemi and Greenleaf [46] proposed a method named as vibro-acoustography. In this method a confocal ultrasound transducer with two elements is, usually, employed. The central disk and annular elements of this transducer are driven with slightly different frequencies. The ultrasound beams interact in the focal zone producing an amplitude modulated force which induces vibrations, with frequency lower than 50kHz, to the target in the range from few nanometers to micrometers [46]. The emitted sound is then measured through a hydrophone.

Figure 1.10(a) shows a depiction of a experimental setup used to acquire the data to form a vibro-acoustography image. The sample to be analyzed is placed at the confocal transducer focal point and the signal is detected through a low frequency hydrophone. Figure 1.10(b) shows an image obtained with a vibroacoustography system built at the GIIMUS [1] Lab. The sample is composed of three small stainless steel spheres (diameter of 0.66 mm), attached to a

[1]GIIMUS: Grupo de Inovação em Intrumentação Médica e Ultrassom at the Departamento de Física e Matemática, FFCLRP, Universidade de São Paulo

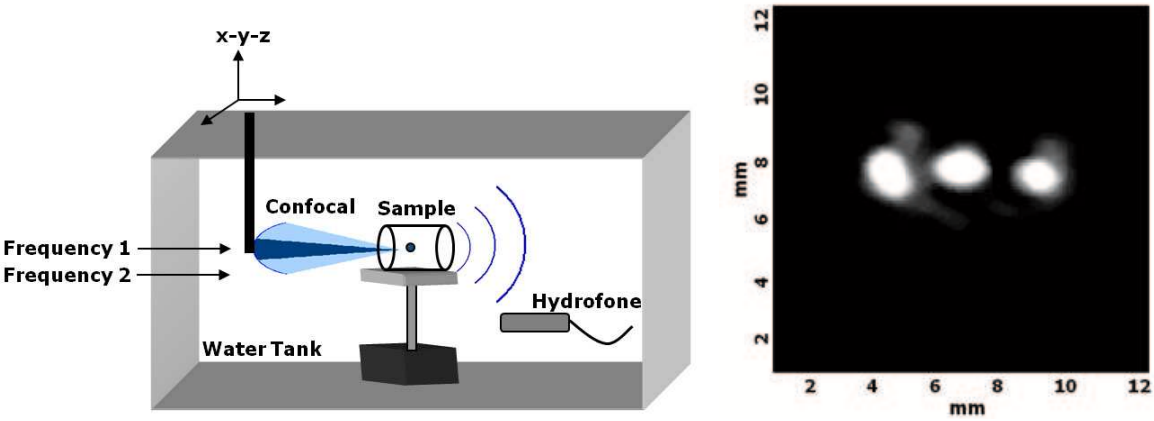

(a) (b)

Figure 1.10: (a) Depiction of a vibroacoustography system. (b) Vibroacoustography image of three small stainless steel spheres (radius of 0.66 mm), attached to a thin plastic wrap, separated by 3 mm (distance between spheres centers) from each other.

thin plastic wrap, separated by 3 mm (distance between spheres centers) from each other. The entire object was placed in a water tank and the sheet surface was scanned in a raster format at 0.1 mm increments in either direction and excitation frequency $\Delta f = 20$ kHz. The amplitude of the acoustic emission signal were calculated at each point relative to the reference signal data.

1.2.5 Vibromagnetometry

Vibromagnetometry, introduced by Carneiro et al. [47], is a technique based on acoustic excitation of a magnetized target and magnetic measurement of the induced displacement. In their introductory work, the authors discussed theoretical aspects of the oscillatory movement of a rigid sphere, embedded in viscous and visco-elastic media, displaced by dynamic acoustic radiation force with frequency range of 0-0.5 MHz. The magnetic field variation at different distances away from the magnetic sphere (made of NdFeB) due to its oscillatory movement was evaluated. Simulations were based on the theory for mechanical impedance, developed by Oestreicher [48], for the oscillations of a rigid sphere in incompressible viscous fluid and viscoelastic medium. The amplitude of the dynamic radiation force was calculated using the theory developed by Silva et al. [49].

Based on the idea of using acoustic radiation force to move a magnetized object and measuring its position through a magnetic sensor, we developed a device to monitoring acoustic pressure and force [50]. A cubic magnet was attached to a thin latex sheet, which was connected to a magnetoresistive sensor. The pressure transducer was calibrated based on the output of a needle hydrophone.

1.3 Thesis organization

Chapters 2 and 3 explore the quasi-static elastography, more specifically, the nonlinear elasticity approach through tissue-mimicking phantom evaluation. The experiments and data analyses were conducted at the Ultrasound Lab. of the University of Wisconsin-Madison.

- Chapter 2 covers the development of phantom materials for elasticity imaging. These materials were specifically designed to provide nonlinear stress/strain relationship that can be controlled independently of the small strain shear modulus of the material. These materials were designed for use in elastography phantoms where heterogeneous configurations (e.g, spherical targets in a uniform background) are employed.

- Chapter 3 investigates the effects of phantom materials nonlinearity over the strain contrast, signal-to-noise ratio and contrast-to-noise ratio of a phantom containing spherical inclusions undergoing large deformations (up to 20%). The changes in contrast over a large deformation range predicted by nonlinear FEA simulations are compared with that experimentally observed.

Chapters 5, 6 and 7 explore the dynamic elastography approach where the ultrasonic radiation force is used to excite the medium under investigation. The dynamic response of a rigid spherical inhomogeneity, embedded in viscoelastic medium and viscous fluid, is evaluated using ultrasonic and magnetic techniques. The experiments and data analyses were conducted at the GIIMUS Lab. of the Universidade de São Paulo.

- Chapter 4 presents the acoustic field characterization of the focused transducer used in the experiments of chapters 5, 6 and 7. Measurements of the axial and radial profiles through a needle hydrophone are discussed.

- Chapter 5 demonstrates the feasibility of measuring vibration movement, through a monochannel continuous wave Doppler system, induced by a confocal transducer. The interference of two ultrasonic beams promote a dynamic force to the target. The ability to form images of a rigid spherical inhomogeneity embedded in viscoelastic phantom by scanning both ultrasonic transducers (confocal and Doppler) across the confocal transducer focal plane is presented.

- Chapter 6 investigates the dynamic behavior of a rigid magnetic sphere, suspended in water in a simple pendulum configuration, caused by acoustic radiation forces. The induced micro-order displacement is tracked using a magnetoresistive sensor. From the tracked

displacement the water viscosity is acceded. The drag force acting on the pendulum during its motion is considered to follow a modified Stokes law for a low Reynolds number, accounting for the phenomena related to its oscillatory movement.

- Chapter 7 presents methods and simulations to measure micro-order displacement using ultrasonic echoes from a vibratory target. The motion of a rigid sphere embedded in gelatin phantom, displaced by acoustic radiation force, is evaluated using the ultrasonic echoes from a mono-channel pulse-echo system. The theory to estimate the viscoelastic parameters from the oscillation of a rigid sphere in visco-elastic medium is covered. This theory is an extension of the relation used to estimate the water viscosity in chapter 6.

- Chapter 8 summarizes the main results and discussions of the thesis work and provides a discussion of future analyzes and experiments to improve the presented work. Perspectives to the elastographic approaches covered in the thesis are also discussed.

2 Nonlinear elastic behavior of phantom materials for elastography

2.1 Introduction

Quasi-static ultrasound elastography is an imaging technique that has been developing rapidly over the last 15 years. More challenging procedures of obtaining and analyzing data are being pursued. Since algorithms are becoming faster and more efficient and the available technology is improving, higher strains are being applied during the echo signal acquisition [51]. The most common method for obtaining elastography images (elastograms or strain images) is to correlate echo signals acquired before and after uniaxial deformation [5, 52].

Most of strain imaging involves deformations of up to 5% which is a region of nearly linear behavior. However when the compression becomes large enough most human tissues present a significantly nonlinear stress/strain relationship without a permanent change in microscopic structure [53, 22]. Breast tumors for instance can exhibit different nonlinear behavior [21]. Attempts to determine which hyperelastic model is capable of fitting breast tissues stress/strain data have been reported [30]. However, the relationship between biological structures and nonlinear stress/strain behavior is not completely understood. It is known that the stress/strain relationship for all networks composed of semiflexible filaments is nonlinear and in cases of stiffer filaments such as collagen, they always stiffen for strains lower than 20% [54].

Approaches that take advantage of the strain stiffening properties to improve elastography image interpretation have been reported [32, 33, 34].

In order to further develop methods for estimating tissues' nonlinear parameters with elastic imaging techniques, the nonlinear stress/strain properties of phantom materials must be better understood. Agar and gelatin are common materials used in manufacturing phantoms to be used in strain imaging [55]. The ultrasonic properties and elastic long-term stability of these materials are well established. It has been shown that agar/gelatin mixtures provide a way of obtaining a reasonably stable material properties [56]; moreover, regarding agar/gelatin mixtures, when

the inclusion and background have the same gelatin concentration, the gelatin provides a good bond between the inclusion and background and stable geometry, i.e., the inclusion does not change volume due to osmosis [56]. Therefore all of the agar/gelatin materials produced in this work had the same gelatin concentration in the agar/gelatin component.

Agar is a well known material for its nonlinear stress/strain relationship [55, 57], while for gelatin the stress/strain relationship is nearly linear [55]. Erkamp et al. [58] adopted the Mooney-Rivlin strain energy density to obtain a nonlinear model to fit the force vs. displacement curves for both materials. Although the Mooney-Rivlin model provides a good fit to the stress/strain data, this approach has a large number of parameters (usually more than 3) to be determined. In order to overcome this problem the Veronda-Westmann model [28, 59], which has only two parameters (nonlinear parameter and shear modulus at zero strain), was used here and has been applied in biological nonlinear modulus reconstructions [34]. This model used assumes uniaxial deformation, isotropic and incompressible material. It is common to assume that aqueous gel phantom materials are incompressible or nearly incompressible soft solids for the experimental conditions typical of elastography (see, for example, Refs. [55, 58, 60]). Although the nonlinear elastic behavior of agar gels and gelatin gels has been reported, the nonlinear elastic behavior has not been described for mixtures of agar and gelatin. Madsen et al. [56] reported nonlinearity of agar/gelatin materials at higher agar concentrations and low strain ranges (see table 5 of [56]), but strain values did not exceed 6%. Further, the stability of heterogeneous configurations of agar/gelatin mixtures containing oil droplets has been reported [56], but the nonlinear stress/strain relationship for these materials has not.

We report an investigation into the nonlinear stress/strain relationships of agar/gelatin mixtures and how that elastic behavior is affected by varying the volume fraction of oil in the dispersion. These materials are being designed for future use in elastography phantoms where heterogeneous configurations (e.g, spherical targets in a uniform background) are anticipated. Thus, materials should be designed with long-term stability in mind. A report on the time-dependent elastic behavior of these materials will follow.

2.2 Materials and methods

Agar is a gel-forming polysaccharide with a sugar skeleton. These gels are normally classified as a crosslinked network meaning the gel network is formed during congealing from an aqueous solution. In the solution state, the agar molecules are randomly distributed as a coil structure. After gelation, the collagen becomes a three dimensional network of double helix fibrils. A good review of these features and a model reporting how they relate to agar rheological

characteristics can be found in [61].

The double helix concentration is assumed to be proportional to the agar concentration. This assumption suggests that the agar elastic modulus can be analyzed by the percolation theory [62] as described below.

Mixtures of agar and gelatin were previously analyzed [63, 64] where it was observed that a granular pattern of agar gel (mainly) was formed into the gelatin matrix. The granule sizes were in the magnitude order of micrometers. The explanation given is that since the gelation temperature of agar is higher than that of gelatin, the agar becomes a gel before the gelatin.

From those analyses several questions are easily raised: 1) What is the nonlinear stress/strain behavior of agar/gelatin mixtures compared to plain agar and plain gelatin? 2) How does the nonlinear behavior of agar/gelatin mixtures depend on agar dry-weight concentrations? 3) Is the stiffness of agar/gelatin mixtures for different agar concentrations consistent with percolation theory? 4) If oil dispersions are made with agar/gelatin mixtures, how does the oil concentration affect the nonlinear elastic properties of the final material? The studies reported here were designed to answer these questions.

2.2.1 Nonlinear behavior

Some polymer gels as well as tissues are normally assumed to be hyperelastic. There are several constitutive relations which were developed in order to model the nonlinear behavior of this kind of material. These models are normally described based on the strain energy W, which is the potential energy stored in the material due to a deformation. In a simple system, W equals the force acting on an object times its displacement. In a continuum system, the stored potential energy (see, for example, Refs. [53, 22]) can be represented in the same way. However, in this work, we consider a strain energy density W:

$$W = \int_{\lambda_{i=1}}^{\lambda} \sigma_i d\lambda_i, \tag{2.1}$$

where λ is the applied Cauchy stress, $\lambda_i = 1 + \varepsilon_i$ (ε_i is the strain) and W has units of energy per unit volume or force per unit area. Since strain energy density does not depend on body motions, it is normally represented as a function of the strain invariants. Those parameters appear from the deformation gradient (F) and the right Cauchy-Green tensor (C), respectively, given by eqs. (2.2) and (2.3). For a better understanding of the following definitions (eqs. (2.2)

to (2.7)), the reader is referred to Ref. [53, p. 271 to 287]

$$F = \begin{bmatrix} \frac{\partial x}{\partial X} & \frac{\partial x}{\partial Y} & \frac{\partial x}{\partial Z} \\ \frac{\partial y}{\partial X} & \frac{\partial y}{\partial Y} & \frac{\partial y}{\partial Z} \\ \frac{\partial z}{\partial X} & \frac{\partial z}{\partial Y} & \frac{\partial z}{\partial Z} \end{bmatrix} = \begin{bmatrix} \lambda_1 & \lambda_{12} & \lambda_{13} \\ \lambda_{21} & \lambda_2 & \lambda_{23} \\ \lambda_{31} & \lambda_{32} & \lambda_3 \end{bmatrix} \tag{2.2}$$

$$C = F^T F. \tag{2.3}$$

The deformation gradient was represented in terms of Cartesian coordinates where (x, y, z) locates a point of interest in the current configuration and (X, Y, Z) locates the same point in its original configuration. Assuming uniaxial deformations, the three strain invariants (I_1, I_2, I_3) derived from C can be represented by the following equations:

$$\begin{aligned} I_1 &= trace(C) = \lambda_1^2 + \lambda_2^2 + \lambda_3^2 \\ I_2 &= \frac{1}{2}\left\{[trace(C)]^2 - trace(C^2)\right\} = \lambda_1^2\lambda_2^2 + \lambda_2^2\lambda_3^2 + \lambda_1^2\lambda_3^2 \\ I_3 &= det(C) = \lambda_1^2\lambda_2^2\lambda_3^2. \end{aligned} \tag{2.4}$$

The second Piola-Kirchhoff stress tensor S is one definition of stress that is useful in non-linear elasticity constitutive formulations:

$$S = \frac{\partial W}{\partial E_S} = 2\frac{\partial W}{\partial C}, \tag{2.5}$$

where $E_S = \frac{1}{2}(F^T F - I)$ is the Green-Lagrange strain tensor. The Cauchy stress can be represented as a function of S:

$$\sigma = \frac{1}{detF} F \cdot S \cdot F^T. \tag{2.6}$$

All the materials in this paper are considered to be incompressible which means that the volume V is constant when the material is deformed, and therefore $detF = \lambda_1\lambda_2\lambda_3 = 1$. Knowing that the samples used in the mechanical tests were cylinders and considering that the volume did not change during the test, it is reasonable to state that (eq. (2.2) and eq. (2.4) and [53, p. 283]) $\lambda_1 = \lambda$ and $\lambda_2 = \lambda_3 = 1/\sqrt{\lambda}$. Therefore, the invariants become $I_1 = \lambda^2 + 2/\lambda$, $I_2 = 2\lambda + 1/\lambda^2$ and $I_3 = 1$. λ is named as stretch ratio and can be understood as $\lambda = (L + \Delta L)/L$ where L is the sample length (thickness) at zero deformation stress $L + \Delta L$ is the length at some nonzero deformation stress and ΔL is the deformation. Using those relations and eqs. (2.3) to (2.6), the

stress can be written in terms of λ and W:

$$\sigma = 2\left[\frac{\partial W}{\partial I_1}\left(\lambda^2 - \frac{1}{\lambda}\right) + \frac{\partial W}{\partial I_2}\left(\lambda - \frac{1}{\lambda^2}\right)\right]. \tag{2.7}$$

In this case, the area of the sample used to calculate the stress must be corrected for the fact that the (incompressible) material has a deformation-dependent surface area. The experimental methods employed in this study involve a controlled deformation in the axial direction, so the corrected instantaneous cross-sectional area (A_c) can be written as

$$A_c = \frac{AL}{L + \Delta L}, \tag{2.8}$$

where A is the initial cross-sectional area.

The Veronda-Westman model

Several semi-empirical representations of W exist [22]. These models are normally classified into polynomial or exponential models. The polynomial model of many terms, known as Mooney-Rivlin, is suitable for a large range of materials. However, having many terms (and parameters to estimate) in the hyperelastic strain model is a drawback when creating materials to make a specific sort of phantom.

The Veronda-Westman model [28] for hyperelastic strain is one example of the exponential approach. This model is a good tradeoff between accuracy and complexity and also has an advantage of having only two independent parameters to be determined. W for this model can be written as

$$W = \mu_0\left[\frac{e^{\gamma(I_1-3)}}{\gamma} - \frac{1}{2}(I_2 - 3)\right], \tag{2.9}$$

where μ_0 is the shear modulus at zero strain and γ is the nonlinear term. Gokhale et al. [59] provide a detailed understanding of the Veronda-Westman model. Substituting eq. (2.9) into (2.7) and using the strain invariants, we can relate the axial component of the Cauchy stress to the overall strain as

$$\sigma = 2\lambda^2\mu_0 e^{\gamma(\lambda^2-2\lambda^{-1}-3)} - \frac{2}{\lambda}\mu_0 e^{\gamma(\lambda^2-2\lambda^{-1}-3)} + \frac{\mu_0}{\lambda^2} - \mu_0\lambda. \tag{2.10}$$

The Young's modulus is given by $E = \partial\sigma/\partial\varepsilon$ therefore E can be written in terms of λ:

$$E = 2\mu_0\left\{e^{\gamma(\lambda^2-2\lambda^{-1}-3)}\left[2\lambda + \lambda^{-2} + 2\gamma(\lambda^3 - 2 + \lambda^{-3})\right] - \frac{1}{2} - \lambda^{-3}\right\}. \tag{2.11}$$

Note that $\mu_0 = E_0/3$ where E_0 is the Young's modulus in the limit as the strain goes to zero, and the Poisson's ratio ≈ 0.5 corresponding to incompressibility.

2.2.2 Percolation theory

De Gennes [65] suggested that percolation theory can describe rheology of the solution-gel transition. The gelation process changes the viscoelastic characteristics of the material. The shear modulus after the transition can be denoted as a function of intermolecular crosslinking probability p:

$$\mu \propto (p - p_c)^t \,, \tag{2.12}$$

where p_c is the percolation threshold (which characterize the transition from solution to gel) and t is the critical exponent. In this work the agar concentration was varied. For agar, it is known that concentration of crosslinks at a fixed temperature is proportional to the concentration of double helix fibrils and that is assumed to be proportional to the agar dry-weight concentration [55, 62].

The percolation theory of gelation implies that the value of t in eq. (2.12) lies in the range 1.8-2.0 for all gel materials [66, 67]. Some authors found critical exponents for gelatin gel to be in good agreement with percolation theory [66, 67]. Fugii et al. [62] similarly applied percolation theory to evaluate the elastic properties of the agar gel as a function of its dry-weight concentration.

The fact that percolation theory predicts that the shear modulus increases proportionally to the dry-weight concentration following a power law behavior suggests that the shear modulus dependence on dry-weight percentage concentration is truly independent of the compression applied to the gel (see figure 2.4). From that it follows that gels have the same nonlinearity independent of the material dry-weight concentration.

2.2.3 Materials production

Four types of materials were produced, namely, agar-based material, gelatin-based material, (agar + gelatin)-based materials and oil dispersions in agar + gelatin.

Agar-based material

A molten agar solution was obtained by mixing 2 g granulated agar (Fisher Scientific, Pittsburgh, PA, cat. No. BP1423) into 100 mL 18 MΩ cm deionized water at room temperature and heating in a "double boiler" to 90 ^{0}C until transparency existed. The molten agar was then cooled to 50 ^{0}C by immersing the beaker in 18 ^{0}C water with stirring. Liquid Germall-plus® (International Specialty products, Wayne, NJ, USA) was added (1.5 g per 100 mL solution) to prevent fungal and bacterial contamination. The agar dry-weight concentration of this plain agar sample was 1.93%.

Gelatin-based material

Gelatin solutions were obtained by mixing 8 g of 200 Bloom gelatin (derived from calfskin; Vyse Gelatin Company, Schiller Park, Illinois) per 100 mL of 18 MΩ cm deionized water (7.4% by weight gelatin) at room temperature and heating in a "double boiler" to 90 ^{0}C until transparency existed. The molten gelatin was then cooled to 50^{0}C and 1.5 g of the preservative Liquid Germall-plus® was added per 100 mL of solution. Then the molten gelatin was further cooled to 36 ^{0}C and formalin solution which is 37% formaldehyde was added such that 0.047 g were present for each gram of (dry-weight) gelatin. Formalin was used for cross linking the gelatin which increases the gelatin's melting point and the elastic modulus [55]. The solutions were poured into small molds to congeal for 3 or 4 days. The resulting samples were cylinders 2.6 cm in diameter and 1.0 cm thick. One sample of plain gelatin was manufactured containing 7.3% dry-weight gelatin.

(Agar + gelatin)-based material

To obtain the agar/gelatin mixtures, molten agar/water solution and molten gelatin/water solution (7.4% by weight gelatin) were mixed together, each at a temperature of about 90 ^{0}C, in a proportion of 40% by volume of gelatin solution and 60% by volume of agar-plus-water solution. The mixture was cooled to 50 ^{0}C and 1.5 g of Liquid Germall-plus® was added per 100 mL of mixture. The mixture was further cooled to 36 ^{0}C and 0.047 g formalin added for each dry-weight gram of gelatin. The mixture was then poured into cylindrical molds to cool and congeal for 3 or 4 days. A more detailed description of the procedure can be found in [56].

The gelatin/water solution used was always 7.4% dry-weight. The agar solution was made with different dry-weight percentages from 1 to 4.8%. The dry-weight percentage gelatin in the mixture was 3.0% and the dry-weight percentages of agar were 0.6 to 2.8%. The final

Table 2.1: Final concentration used to make the agar/gelatin samples.

Sample	Agar (%)	Gelatin (%)	Germall-plus (%)	Formaldehyde (%)
1	0.58	2.94	1.46	0.138
2	1.15	2.94	1.46	0.138
3	1.71	2.93	1.46	0.138
4	2.27	2.93	1.45	0.138
5	2.81	2.92	1.45	0.138

Table 2.2: Materials compounding the gel matrix used to make the oil droplets in agar/gelatin samples.

Sample	Agar (%)	Gelatin (%)	Germall-plus (%)	Formaldehyde (%)
1-3	0.58	2.94	1.46	0.138
4-6	1.15	2.94	1.46	0.138
7-9	1.71	2.93	1.46	0.138
10-12	2.27	2.93	1.45	0.138

concentrations - accounting for the added formalin and Liquid Germall-plus® - are shown in table 2.1.

It is important to note that the gelatin concentrations are the same for all samples so that if a phantom is to be manufactured with an inclusion, the inclusion and background of phantoms will have the same dry-weight concentrations of gelatin to minimize osmotic pressure differences. Equal gelatin concentration in the inclusion and background also helps to bond the inclusions to the background [68, 56].

In order to manufacture the fourth type of material (oil dispersions), plain gelatin (7.4%) was poured into plain agar (0.99, 1.96, 2.91 and 3.85% by weight), as shown in table 2.2. The gel was poured into safflower oil and gently stirred with an appropriated spoon. A surfactant (Ultra Ivory® Proctor and Gamble Company, Cincinnati, OH, USA) was added so that emulsification was sufficient to produce microscopic oil droplets that would not separate from the aqueous gel during either the congealing process or the mechanical test. This test consists in compressing the phantom sample as described in section 2.2.4. The volume of the surfactant is approximately 1% of the safflower oil volume. The detailed procedure to obtain the oil in aqueous gel materials was previously described [56, 69]. The oil volume percentages produced were 0%, 20% and 50%. Therefore, 12 samples were obtained. The oil volume percentages in each of the 12 samples are shown in table 2.3.

All samples were stored submersed in safflower oil to prevent dehydration.

Table 2.3: Oil volume percentage for the samples presented in table 2.2.

Sample	Oil volume (%)
1;4;7;10	0
2;5;8;11	20
3;6;9;12	50

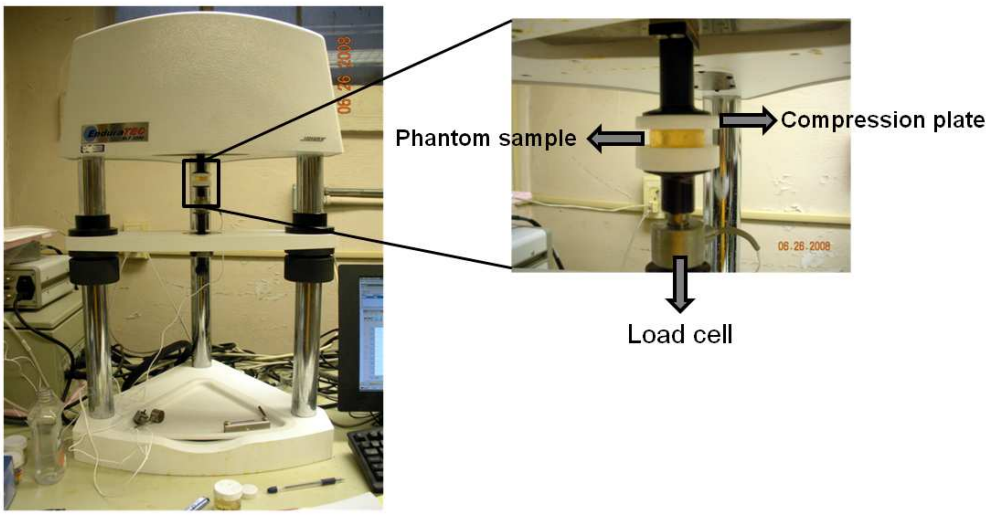

Figure 2.1: Photograph of the experimental setup adopted for the mechanical testes to evaluate the Young's modulus and stress/strain of the phantom samples.

2.2.4 Elastic measurements

Mechanical tests were performed on each of the samples to evaluate their stress/strain properties using a Bose EnduraTEC 3200 ELF system (Bose Corporation EletrectroForce Systems Group, Minnetonka, MN, USA) with a 1kg load cell and Teflon® platens larger than the sample surface. Low-amplitude, 1 Hz oscillatory compressive load was used to determine the complex Young's modulus. The photograph of the experimental setup is shown in figure 2.1. Large oscillatory deformations (compressions up to 25%) were employed to assess nonlinear characteristics. The loading cycle of the stress/strain curve was chosen for this purpose.

The same oil used to store the materials was also used to lubricate the platens during the tests to minimize friction between the plates and the sample.

After the upper platen established contact with the sample, the platen was lowered to the mean level of oscillation amplitude at a rate of 0.04 mm s^{-1}. The platen remained at the mean level for 5 s. In the next step the sample underwent a sinusoidal compression in the desired amplitude and frequency for 5 s before starting data acquisition. These procedures were done to "precondition" the sample [22, 55] and obtain consistent load-displacement measurements.

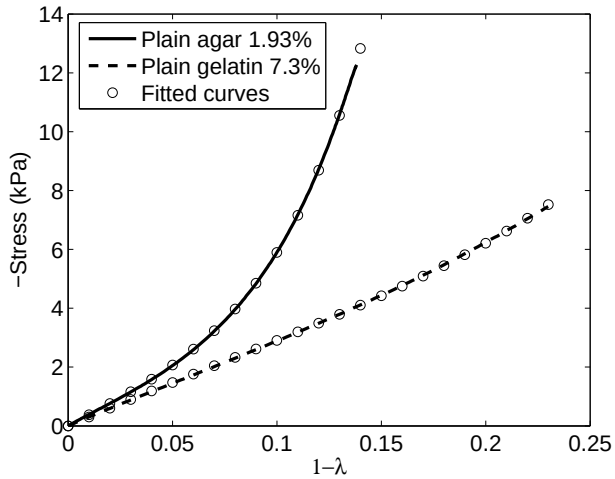

Figure 2.2: Stress (eq. (2.10)) versus stretch ratio (λ) of the plain agar and plain gelatin materials. The fitted Veronda-Westman model results are also shown for both cases.

Force and displacements data were then acquired.

Deformations up to 25% were adopted since this amount of deformation should be sufficient to evaluate the nonlinear parameters of tissues being imaged with an ultrasound scanner [34]. Deformation beyond 25% could also have damaged the phantoms, especially those containing agar which is a brittle material. However, no study to verify the fracture point was done.

Considering the use of a 1 kg load cell and the initial diameter of the samples being tested (2.6 cm), the maximum measurable stress in these experiments (not accounting deformation-dependent sample area) would be around 19 kPa.

The results described in this manuscript were obtained from measurements made at least 2 months after the sample production; that is a reasonable period for the materials to become stable [55, 56, 69]. Two sets of measurements were made for each sample on consecutive days. The results shown below are the average of these two measurements and the errors are the standard deviation (of only two measurements).

2.3 Results

Before evaluating the nonlinear properties of the agar/gelatin and oil-in-agar/gelatin materials, it is useful to first analyze the plain agar (1.93% dry-weight) and plain gelatin (7.4% dry-weight) materials. The stress versus stretch ratio (λ) for those materials are shown in figure 2.2. It is clear that the agar sample stiffens faster than the gelatin [55]. The data were fit to the Veronda-Westman constitutive model (eq. (2.10)) using a nonlinear least-squares and the

Table 2.4: Fitting parameters γ and μ_0 for the plain gelatin (7.3% dry-weight) and plain agar (1.93% dry-weight). R^2 stands for the coefficient of determination.

Sample	γ	μ_0 (kPa)	Model E (kPa)	DMA E (kPa)	R^2
Plain gelatin 7.3%	0.9 ± 0.1	10.1 ± 0.2	30.2 ± 0.6	28.9 ± 0.3	1.00
Plain agar 1.93%	9.0 ± 0.2	12.7 ± 0.1	38.8 ± 1.2	41.6 ± 1.9	0.99

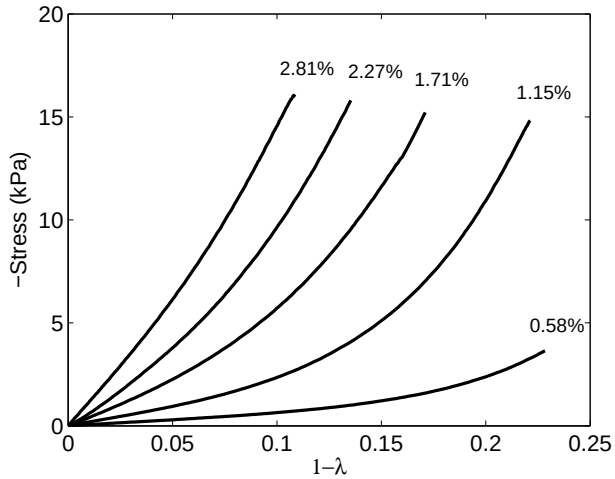

Figure 2.3: Stress versus stretch ratio for the set of agar/gelatin samples with five different dry-weight concentrations of agar.

Levenberg-Marquardt methods [70, 71]; resulting values for γ and μ_0 are shown in table 2.4. The values of Young's moduli ($3\mu_0$) at zero strain are compared to the Young's storage modulus acquired from the oscillatory DMA (dynamic mechanical analysis) at 1% pre-compression and 1% amplitude peak to peak.

The results of the mechanical tests for agar/gelatin samples (table 2.1) are presented in figure 2.3. Those data were fit to the Veronda-Westman model and the results are shown in table 2.5.

Table 2.5: Parameters γ and μ_0 obtained by fitting the data shown in figure 2.3 to the Veronda-Westman model (eq. (2.10)) and the corresponding coefficient of determination (R^2). A comparison of the model Young's modulus at zero strain ($3\mu_0$) to results estimated with the Enduratec DMA software is also provided.

Sample	γ	μ_0 (kPa)	Model E (kPa)	DMA E (kPa)	R^2
0.58% agar in gelatin	4.1 ± 0.2	1.8 ± 0.1	5.3 ± 0.1	6.3 ± 0.1	0.93
1.15% agar in gelatin	4.8 ± 0.1	6.7 ± 0.2	20.0 ± 0.7	23.7 ± 0.8	0.95
1.71% agar in gelatin	4.3 ± 0.1	15.8 ± 0.2	47.5 ± 0.4	44.7 ± 3.1	0.92
2.27% agar in gelatin	4.7 ± 0.5	25.0 ± 0.9	79.6 ± 9.3	82.2 ± 7.1	0.84
2.81% agar in gelatin	4.7 ± 0.7	39.3 ± 2.2	117.8 ± 6.7	132.0 ± 3.0	0.89

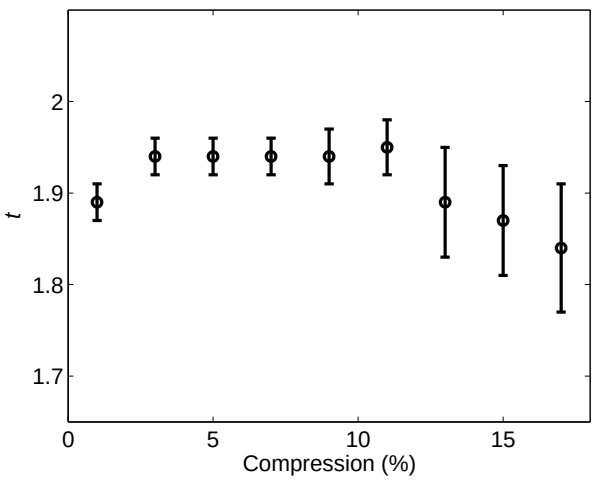

Figure 2.4: Critical exponent (t) versus the compression applied to the sample for the (agar + gelatin)-based material.

From the Young's moduli in table 2.5, the critical exponent t relating to percolation theory (eq. (2.12)) was $t = 1.89 \pm 0.02$ in agreement with that previously reported for agar or gelatin materials [55] suggesting that the stiffness of gelatin and agar mixtures for different agar dry-weight concentrations obeys percolation theory (that is, the mixtures have the same critical exponent as observed for the plain agar material).

The samples presenting a consistent nonlinear behavior (table 2.5) suggests that the shear modulus dependence on dry-weight percentage concentration is truly independent of the compression applied to the gel. That implies that, within this measurement range, the critical exponent would be the same regardless the applied compression to the material (see figure 2.4).

The stress/strain curves for the oil-in-agar/gelatin materials are represented in figure 2.5. The graphs were organized so that the samples with the same agar dry-weight concentration but different oil volume percentage are shown in the same plot.

The results in figure 2.5 are well represented by the Veronda-Westmann model ($R^2 > 0.92$). The nonlinear parameter (γ) obtained from the fits are shown in figure 2.6. The oil emulsification decreased the nonlinear behavior of the materials. Figure 2.7 shows the storage moduli obtained from the mechanical tests of the oil-in-agar/gelatin materials. Figure 2.7(a) represents the actual values obtained. Those values were fit to a power law in order to compare the percolation theory critical exponents (eq. (2.12)) for samples with different oil volume fraction (table 2.6). Figure 2.7(b) represents the 20% and 50% oil volume fraction materials' storage moduli relative to the values acquired for the case of 0% of oil. Those plots show that for a higher agar concentration the relative storage modulus reduction is more accentuated than that for lower agar concentrations.

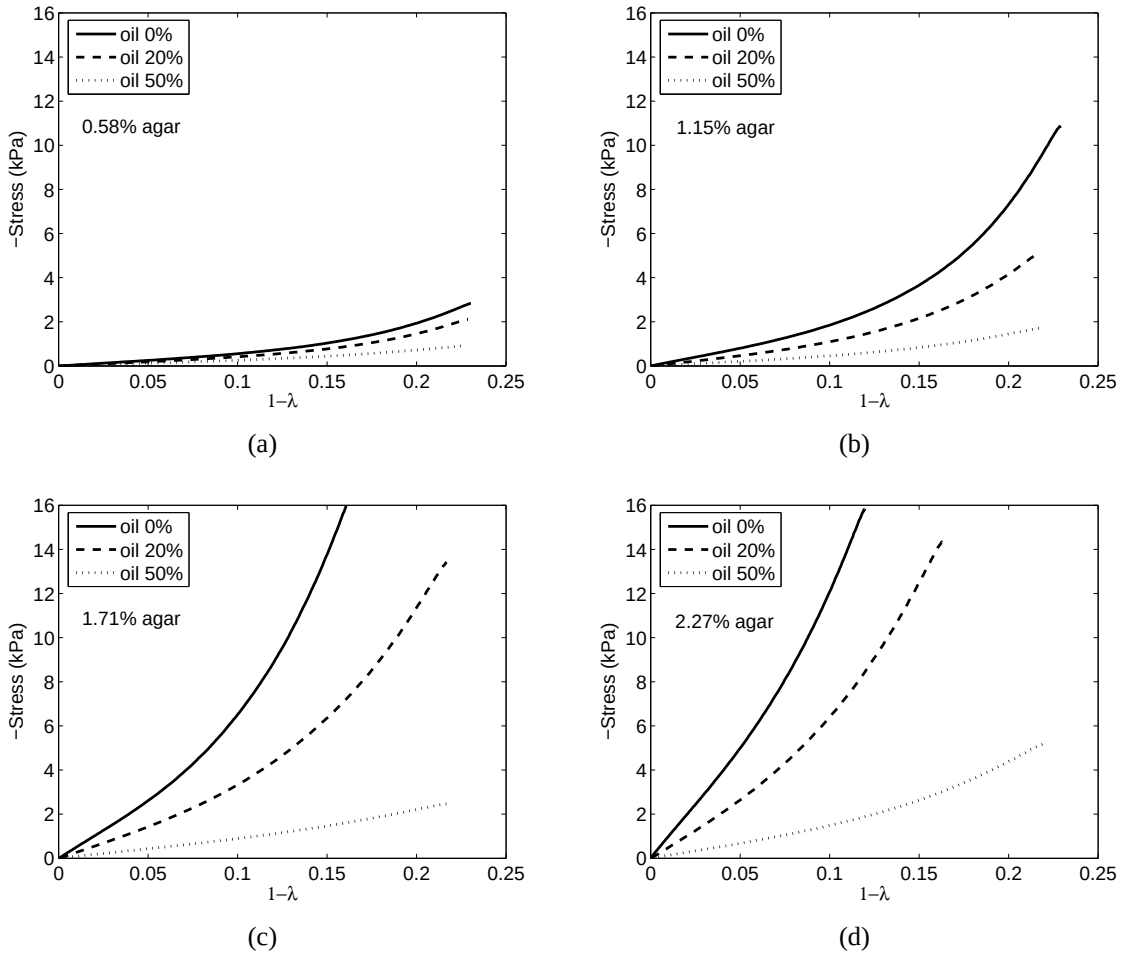

Figure 2.5: Stress versus stretch ratio for the twelve oil-in-agar/gelatin samples with 0%, 20% and 50% oil. The agar concentrations are (a) 0.58%, (b) 1.15%, (c) 1.71%, (d) 2.27%.

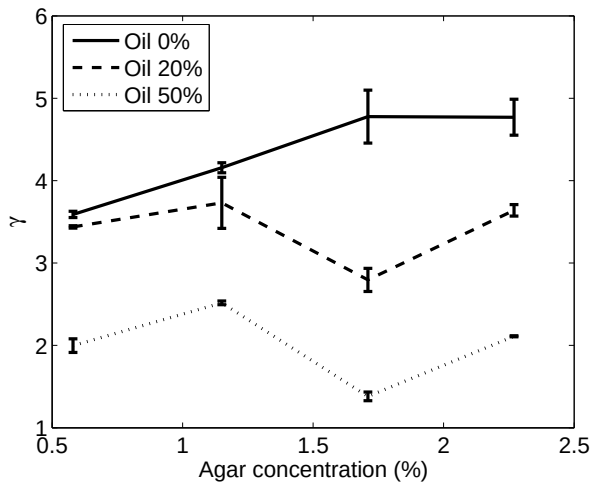

Figure 2.6: Nonlinear parameter (γ) versus agar concentration for the oil-in-agar/gelatin materials.

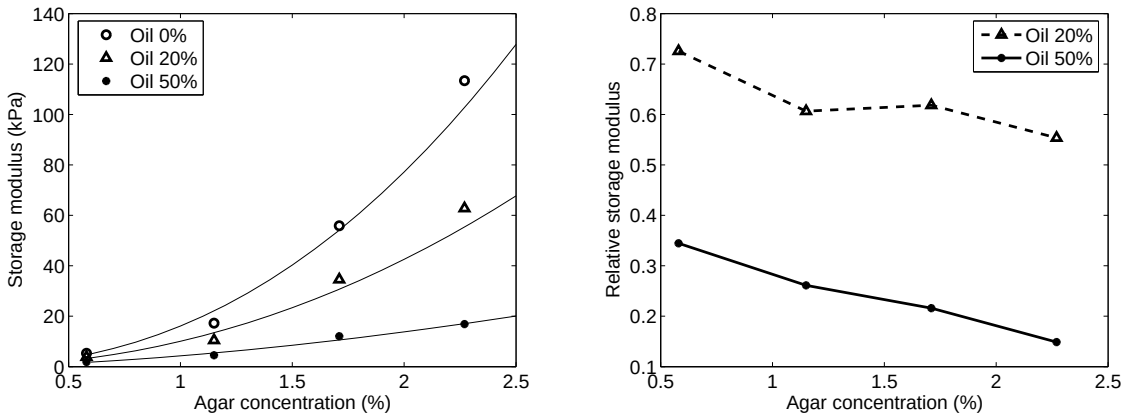

(a) (b)

Figure 2.7: Young's storage modulus (DMA calculation) versus agar concentration for the three oil emulsification volumes (1% of compression). (a) Curves corresponding to percolation theory power (t) law fits (table 2.6). (b) Curves representing the percentage storage modulus of the 20% and 50% oil volumes emulsification relative to the 0% oil volume versus the agar concentration.

Table 2.6: Critical exponents obtained for the oil-in-agar/gelatin samples.

Sample	t	R^2
Oil 0%	2.3 ± 0.2	0.98
Oil 20%	2.1 ± 0.2	0.97
Oil 50%	1.7 ± 0.2	0.98

The critical exponent for 0% oil ($t = 2.3 \pm 0.2$; table 2.6) is in the range of values found in the literature [62]. The fact that the exponents decreased for higher oil volume concentrations agrees with the results of the chart represented in figure 2.7(b).

2.4 Discussion

These results should enhance our ability to select materials for producing nonlinear elasticity imaging phantoms which mimic clinical situations. For example, knowing the appropriate model functions and how the parameters depend on constituent materials allows predicting stress/strain curves to be used as inputs to nonlinear finite-element simulations. Simulations and development of anthropomorphic phantoms are resulting tools for assessing the validity of promising nonlinear elastographic techniques [34].

2.4.1 Plain agar and plain gelatin

The nonlinear parameter of the plain agar (1.93% by weight) was ten times greater than that found for the plain gelatin (7.4% by weight; table 2.4). The fact that the coefficients of determination (R^2) for those two extreme cases were quite large indicates that the Veronda-Westmann model is a good model for the nonlinear stress/strain curves of these phantom materials. The shear moduli at no strain (obtained from the Veronda-Westmann model) were compared to the storage moduli calculated by the DMA method. The difference between the results obtained by the two methods was of 7.8% and 4.5% for the plain agar and plain gelatin, respectively, further suggesting that the Veronda-Westmann model is a good choice for these materials and experiments.

2.4.2 Agar/gelatin mixtures

The average nonlinear parameter values (γ) obtained for the various agar/gelatin mixtures (table 2.5) was 4.5 ± 0.3. No trend in γ was observed for different agar concentrations suggesting that the nonlinearity of the agar/gelatin mixtures did not depend on agar concentration in the range from 0.58% to 2.81%.

The Young's moduli for the agar/gelatin mixtures obtained from the Veronda-Westmann model were also in agreement with the storage moduli measured via DMA. The critical exponent t relating to percolation theory was in agreement with that found for plain agar [55]. Presenting a consistent critical exponent independent of the applied compression (up to 17%; figure 2.4) supports the fact that nonlinear behavior remained constant for the range of agar concentration tested.

Figure 2.6 shows that the presence of oil reduced the nonlinear behavior of the samples such that the higher the oil concentration, the lower the nonlinear parameter γ. The γ value for the 20% oil was about 75% of γ for the 0% oil samples, and that for the 50% oil sample was about 45% of the 0% sample.

The decrease in Young's storage moduli with addition of oil was more pronounced at higher concentrations of agar as shown in figure 2.7. This phenomenon was also observed by [72]; however, in their case only plain agar was examined. For both 20% and 50% oil in figure 2.7 the fractional decrease in stiffness followed a linear behavior with $Y = -0.084Ag + 0.75$ ($R^2 = 0.82$) for 20% oil and $Y = -0.105Ag + 0.40$ ($R^2 = 0.99$) for 50% oil where Y is the ratio of storage modulus with oil to that with no oil and Ag is the agar concentration (%). Though a power law relationship for stiffness versus the agar concentration still exists, the critical expo-

nent values (t) decreased with increasing oil in materials (table 2.6).

2.5 Summary

In this chapter, the hyperelastic behavior of materials commonly used to manufacture phantoms for elastography were analyzed. Special attention was given to their nonlinear behavior. The stress/strain curves for four sets of samples (plain agar; plain gelatin, agar/gelatin mixtures, oil-in-agar/gelatin mixtures) were fit to the Verona-Westmann nonlinear model. The elasticity of plain agar was more nonlinear than that of gelatin. The agar/gelatin mixtures showed a nonlinear behavior between that of gelatin and agar. It was observed that adding oil to the agar/gelatin mixtures decreased the stiffness of the gels and also decreased nonlinear behavior. The insights provided by this study could facilitate development of heterogeneous tissue mimicking phantoms for representing mechanical nonlinearities occurring in normal and abnormal tissues.

3 Nonlinear elasticity phantom containing spherical inclusions undergoing large deformations

3.1 Introduction

Elastography is an imaging technique that estimates elastic parameters of materials and soft tissues. This modality is typically implemented with either ultrasound [5] or MRI [4]. Most of the work in this field deals with small amplitude deformations (dynamic or quasi-static). Therefore, essentially linear elastic behavior is involved. However, most biological tissues demonstrate nonlinear stress/strain relationships for sufficiently large deformations [21, 22].

Hall et al. [24] demonstrated changing contrast of some in vivo breast lesions with increasing applied load and attributed those changes to differences in the nonlinear elastic properties of the constituent tissues. Varghese et al. [73] simulated strain images using an analytical plain strain approach to evaluate change in contrast and contrast-to noise-ratio (CNR) due to increasing on the Young's modulus with the applied deformation for either the inclusion or the background. They indicated that CNR could be enhanced or diminished depending on the deformation between a pair of frames or the pre compression applied.

There are also a few reports of attempts to differentiate materials based on the nonlinear stress/strain analysis. Skovoroda and coworkers did some of the initial work [74], but assumed a linear stress/strain behavior for large deformations. Erkamp et al. [32] used a phantom composed of linear material (the upper part) and a nonlinear material (the bottom part). They recognized that the contrast between the parts changed for increasing applied strain. They used stress/strain data as input to nonlinear finite elements analysis (FEA) simulation to compare simulated ultrasonic strain images with their phantom data. Nitta and Shiina [33] obtained a nonlinear parameter of tissues embedded in gelatin phantoms using strains up to 20%. They assumed the stress/strain curve to be exponential and transformed the values of strain obtained

into Young's modulus through FEA implementation using the incremental surface pressure obtained through a pressure sensor.

Measuring the speed of shear waves propagating in phantoms with different levels of initial deformation was also reported as a means of estimating the nonlinear behavior of those materials [75]. Sinkus et al. [76] studied the second harmonics of the time-dependent shear displacement in an attempt to extract nonlinear behavior, but their work involved very small deformations where the differences in nonlinear behavior among tissues appears to be quite small. Gokhale et al. [59] proposed an algorithm to measure the nonlinear parameter obtained from the Veronda-Westmann hyperelastic model [28]. Their approach is more robust since it is an inverse problem based on the mechanical constitutive laws and displacement data at low and high applied strain. The algorithm was applied to breast *in vivo* data [34] of a fibroadenoma and an invasive ductal carcinoma. The reconstruction showed similar behavior of mechanical tests of excised tissue samples from other work [21].

Since hyperelastic models are being employed in nonlinear elastography, it is important to characterize those models using mechanical test data. Attempts to determine which hyperelastic model "best" fits breast tissues stress/strain data has been reported [30]. Although this is an excellent start, more work needs to be done.

A useful approach to characterizing and "optimizing" methodologies for studying nonlinear tissue elasticity is through tissue-mimicking phantom experiments. Agar and gelatin are well characterized materials used in manufacturing phantoms for elastography [55]. Agar/gelatin mixtures [56] and oil-in-gelatin dispersions [68] have been employed in heterogeneous phantoms. This chapter reports on a phantom containing spherical inclusions crated using information about the nonlinear behavior [31] of agar/gelatin mixtures and agar/gelatin with oil emulsification [31]. The phantom contains four spherical inclusions each with distinct small-strain Young's modulus and nonlinear mechanical behavior that is different from that of the background material. This phantom was subjected to large deformations (up to 20%) while scanning with ultrasound, and strain image contrast, contrast-to-noise ratio (CNR) and signal-to-noise ratio (SNR) were investigated as a function of applied deformation.

Nonlinear FEA simulations were created using stress/strain data from the mechanical tests of the phantom materials composing the inclusions and the background, and the simulated data were compared to the experimental images. Image quality metrics from both experiments and simulations were also compared. This work illustrates that nonlinear elasticity phantoms are relatively easy to manufacture and their mechanical properties can be predicted from independent measurements of the constituent materials.

3.2 Materials and methods

3.2.1 Phantom production

Phantoms containing cylindrical inclusions are the most popular configuration to test ultrasound imaging performance, including elastography. Methods to manufacture phantoms containing spherical inclusions arranged in a coplanar array were developed [77, 78] to achieve results more similar to what is clinically observed. The present work employed the technique described in those two papers to produce a phantom containing four spherical inclusions. Each of these spheres was manufactured using a different composition resulting in inclusions with unique stiffness and nonlinearity.

Each of the spherical inclusions was produced by lowering two parts of an acrylic mold - each with a 1cm diameter hemispherical depression - into the molten form of the tissue-mimicking (TM) material and closing the two parts to form a sphere; alignment pegs and holes assure that the two hemispheres produce a sphere.

The procedure for exact positioning of the four spheres in the background material is similar to that described previously [79]. First, a bottom section is made which is 10 cm x 10 cm in horizontal dimensions and 6.85 cm in height. The container for this section has two parts. One part is an acrylic frame with vertical sides and inner dimensions of 10 cm x 10 cm x 6.35 cm with a Saran Wrap® square glued over the bottom and a flat constraining surface beneath the Saran Wrap. The other part is a flat acrylic plate with four acrylic spherical caps projecting downward; the caps have a radius of curvature of 0.5 cm and project downward 1.5 mm. The centers of the spherical caps are at the corners of a 3 cm x 3 cm square. The plate is secured to the open (upper) end of the vertical frame, sealing the volume to be filled with molten TM background material. (Before closing the container, all inner surfaces are covered with a thin layer of petrolatum so that the congealed part does not adhere to the bounding surfaces.) The volume is filled with molten TM material through a sawed-off syringe barrel in a hole in one acrylic wall and allowed to congeal overnight (see Background 1 in figure 3.1(a)). Then the plate with the spherical caps is removed exposing a 10 cm x 10 cm area of background material with four spherical cap depressions, and the four spherical inclusions are “glued” into the spherical cap depressions with a small amount of molten background TM material. Then a square acrylic frame with vertical sides and inner dimensions 10 cm x 10 cm and height 3.65 cm and Saran Wrap on top is glued to the bottom acrylic part forming an enclosed 10 cm x 10 cm x 10 cm cubic volume. A constraining acrylic plate is on top of the Saran. Before the gluing is done the inner surfaces are coated with petrolatum. Also, there is a sawed-off filling

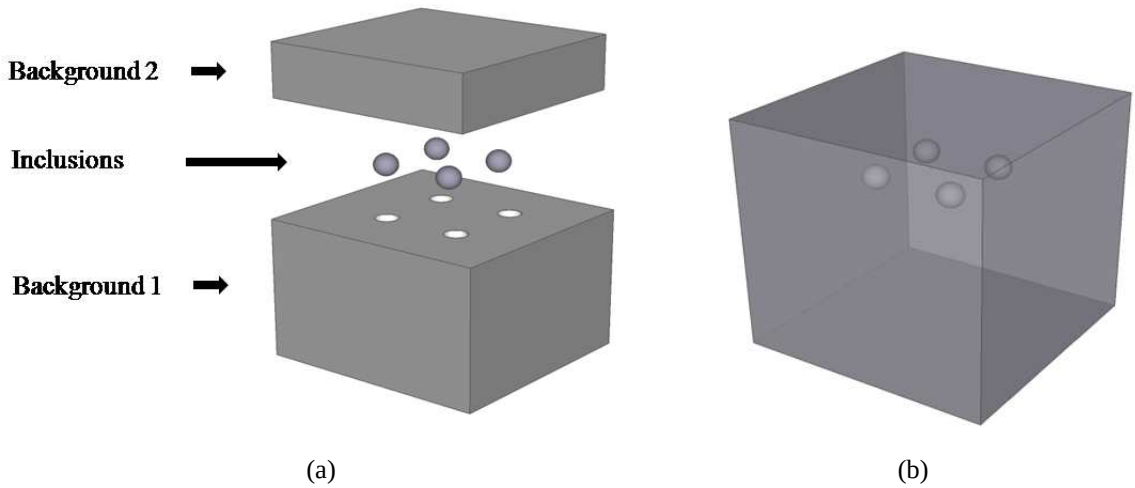

Figure 3.1: Three dimensional depiction of the phantom. (a) Parts that composed the phantom; (b) the phantom in its final form.

syringe in one acrylic wall. Allowing the "glue" for the spheres to harden and formalin cross-linking to be completed overnight, the remaining volume of the phantom is filled with molten TM background material surrounding the spheres (see Background 2 in figure 3.1(a)).

Figure 3.1(a) shows a 3D depiction of the parts which compose the phantom and figure 3.1(b) shows its final visualization. The upper part of the background is denoted as "Background 2" and the bottom part as "Background 1". Figure 3.2 shows diagrams of the phantom geometry configuration.

The background material was made using the agar gelatin mixture procedure [56]. The volume percents were 60% agar solution and 40% gelatin solution. The weight percents of all component materials in the background are shown in the top row of table 3.1.

The inclusions materials were all manufactured employing the same gelatin concentration as the background. The agar/gelatin materials in the four spheres all contain the same dry weight percent gelatin as is found in the background material. This uniform gelatin concentration prevents osmotic effects from causing water absorption or loss by the spheres [80]. One sphere (inclusion 1 in table 3.1) is a dispersion of oil droplets in the agar/gelatin material (50% oil by volume), while the other three spheres contain no oil and differ from the background material in dry weight agar concentration. The oil dispersion material decreases both the nonlinear behavior [31] and the Young's storage modulus [68, 31] of the material. Increasing the agar concentration does not greatly affect the nonlinear behavior [31]. Inclusion 1 was manufactured to be stiffer than the background and present a lower nonlinear behavior, and the other inclusions were manufactured to be stiffer then the background, and to present a similar nonlinear behavior.

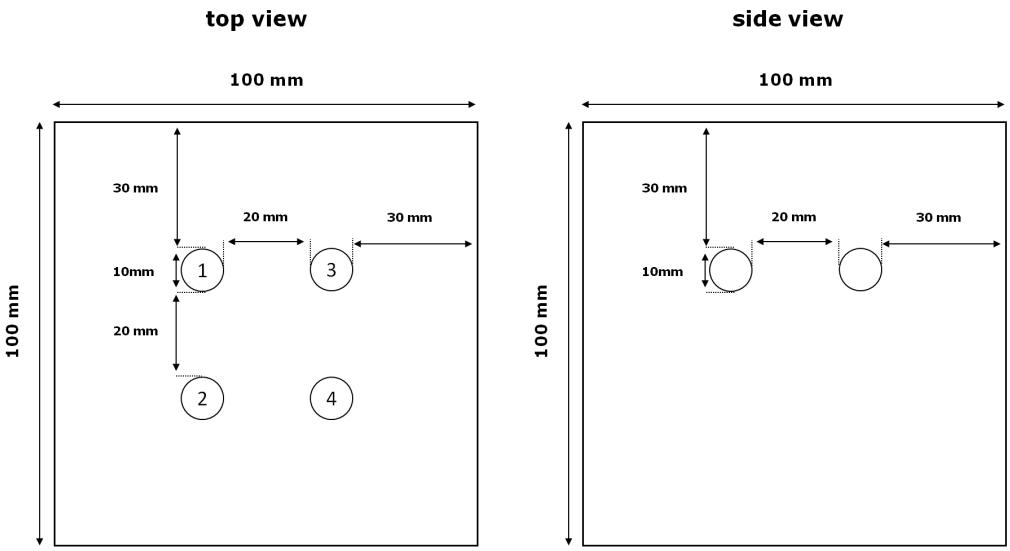

Figure 3.2: Diagram showing the phantom geometry.

Table 3.1: Weight percents of component in the agar/gelatin used to make the phantom background and the four spherical inclusions. Note that the table does not include 2.7 cc (liquid) Ultra Ivory® detergent (Procter and Gamble, Cincinnati, Ohio, USA) per liter of the agar/gelatin plus 50% oil in inclusion 1 (volume percents).

Sample	Agar (%)	Gelatin (%)	Formalin (%)	Germall Plus (%)	Glass beads (%)
Background	0.58	2.94	0.15	1.45	0.19
Inclusion 1	2.24	2.93	0.15	1.45	0
Inclusion 2	1.32	2.93	0.15	1.45	0.39
Inclusion 3	1.09	2.93	0.15	1.44	0.39
Inclusion 4	0.92	2.93	0.15	1.44	0.39

Table 3.1 shows the dry weight concentrations of the agar/gelatin material in the inclusions and background.

At the time of production of each TM material in the phantom, a cylindrical test sample of that material was also made for measurements of the Young's modulus. The cylinders are 2.6 cm in diameter and 1.0 cm in height.

3.2.2 Elastic measurements

Mechanical tests were made on the test cylinders. An EnduraTEC 3200 ELF system (EnduraTEC systems corporation, Minnetonka, MN, USA) with a 1 kg load cell was employed with a 1 Hz oscillatory compressive load applied parallel to the cylinder axis. Oil used to store the materials lubricated the platens during the tests to minimize friction between the platens and the sample. A detailed description of the procedure has been published [56].

Two elasticity measurement approaches were used. The first approach was to calculate the Young's modulus for different pre-compression values. The incremental level adopted was of 0.2 mm (2% of the uncompressed sample height) and for each pre-compression value the peak-to-peak amplitude of oscillation was 0.1 mm. The first pre-compression value was of 1% of the sample height followed by 3%, 5%, etc. When the test was finished, the complex Young's modulus for each pre-compression value was calculated using DMA (Dynamic Mechanical Analysis). The second approach was performed in order to acquire a stress/strain curve to be used as input to the FEA simulation, as will be clarified in section 3.2.5. To acquire the appropriate data the sample was pre-compressed to 12% and the peak to peak at 1 Hz amplitude of oscillation was 24% (plus and minus 12%). The methodology to obtain the stress/strain curve is the same as described by Pavan et al. [31].

3.2.3 Phantom experiment

In order to evaluate the change in contrast, CNR and SNR with the applied deformation, radiofrequency (RF) data were acquired during uniaxial deformation of up to 20% strain and subsequent decompression; i.e., data were acquired during loading and unloading. The frame rate was adjusted to acquire 80 frames during a load-unload cycle. This compression-decompression was performed using a compression plate attached to the ultrasound transducer, the transducer active elements lying in the plane defined by the contact surface of the compression plate. The plate covered the entire top surface of the phantom during the loading and unloading. The bottom of the phantom rested on a fixed plate parallel to the compression plate. A photograph of the experimental setup is shown in figure 3.3. The center of the image field was located over one of the spheres and the procedure was repeated for each sphere.

The experiment was accomplished using a SONOLINE ™ Antares (Siemens Medical Solutions USA, Inc. Malvern, PA) ultrasound scanner, which has a sampling rate of 40 MHz, using the VFX9-4 linear array excited with 8.89 MHz pulses.

Incremental displacement and strain estimation

The motion experienced by a specific region of the phantom between a pair of frames (RF maps) was estimated through a dedicated modified block matching motion tracking algorithm [51]. That approach can be basically explained in two steps:

1. Initial search: In this phase a global axial motion was determined to establish if the motion occurred towards or away from the transducer. Using this information and the information

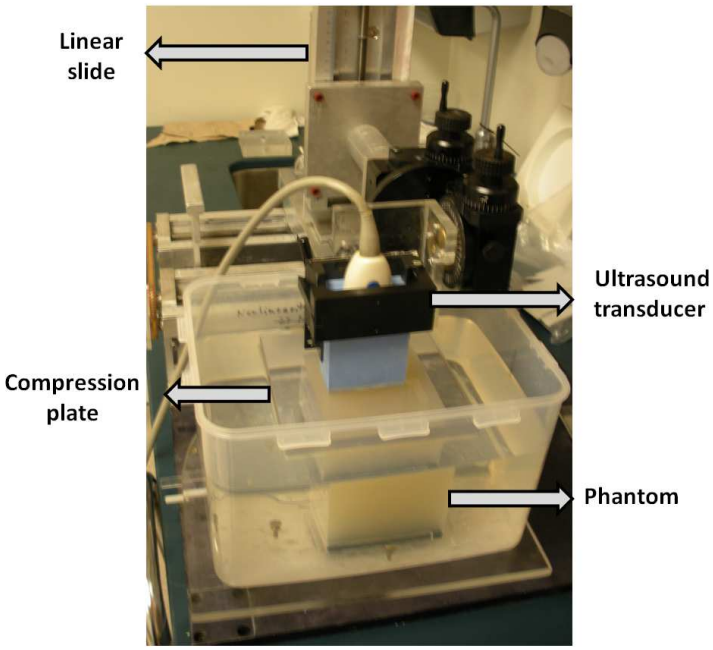

Figure 3.3: Photograph of the experimental setup to obtain the strain images.

of motion continuity, an initial search in the middle of the ROI specified by the user was performed. This strategy is analogous to the algorithm reported in Ref. [9]. Final corrections were made to increase the robustness of the results.

2. Guided search: The initial search adopted a search region of approximately 9 x 8 RF samples (approximately 0.5 x 1.0 mm^2). Using the displacement information obtained in the first step, the search region for the subsequent guided search could be reduced to 3 x 3 RF samples . Sub-sample displacements were obtained in both steps interpolating the results by a quadratic function.

Local axial strain was calculated using a 1.6 mm linear regression window to estimate the gradient of the displacement map. The estimated local strain was the slope of the linear regression curve. The motion was calculated between pairs of frames separated by approximately 1.5% frame-average strain. This frame pairing strategy has been shown to work very well in phantoms and soft tissues for motion tracking [81].

A second method for strain image formation was also used (see figure 3.4). Accumulated strain images were created by simply summing (pixel by pixel) the motion compensated (described below) local strains obtained while loading the phantom. (See figure 3.9(b) for the distinction between local strain and accumulated strain images contrasts.)

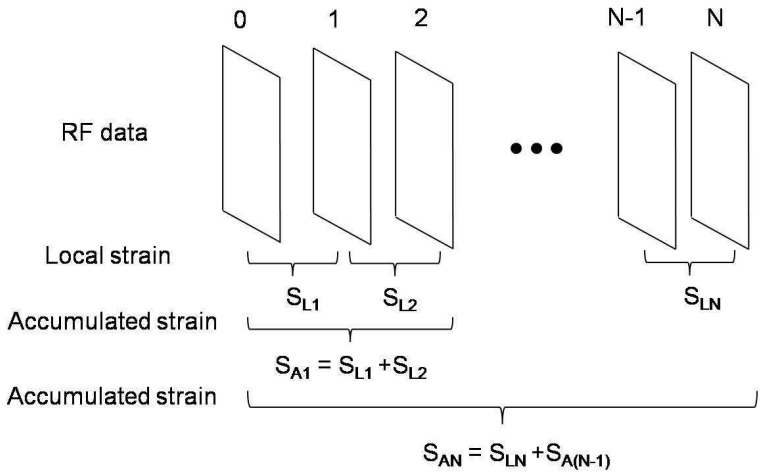

Figure 3.4: Schematic representation of how, the local and accumulated strain, were obtained.

Motion compensation

The phantom was deformed uniaxially to create local strains. Deforming the phantom results in reorganization of the scatterers and an apparent motion of the spherical inclusions toward the transducer. Therefore, to perform image analysis on the sequence of strain images, the motion must be compensated.

The current strain image frame was motion compensated by warping its coordinate system into the coordinate system of the strain image calculated for the first step of the loading process ($\sim$1.5%) using the accumulated displacements calculated up to this point. A 2D linear interpolating procedure was adopted to accomplish the warping process. Figure 3.5 illustrates the process of strain image motion compensation.

3.2.4 Statistical analysis

The three parameters commonly used to evaluate elastograms are the contrast, contrast-to-noise ratio (CNR) and signal-to-noise ratio (SNR). The true contrast (C_t) is defined as the ratio of the Young's modulus of the inclusion to that of the background. The observed contrast (C_0) is defined as the ratio of the strain experienced by the background ($\overline{e_B}$) to that of the inclusion ($\overline{e_I}$); strain is the parameter commonly measured in elastography

$$C_0 \equiv \frac{\overline{e_B}}{\overline{e_I}}. \tag{3.1}$$

The ratio between the observed strain image contrast and underlying modulus contrast (C_0/C_t) is defined as the contrast transfer efficiency (CTE) [82]. Analytical solutions for the

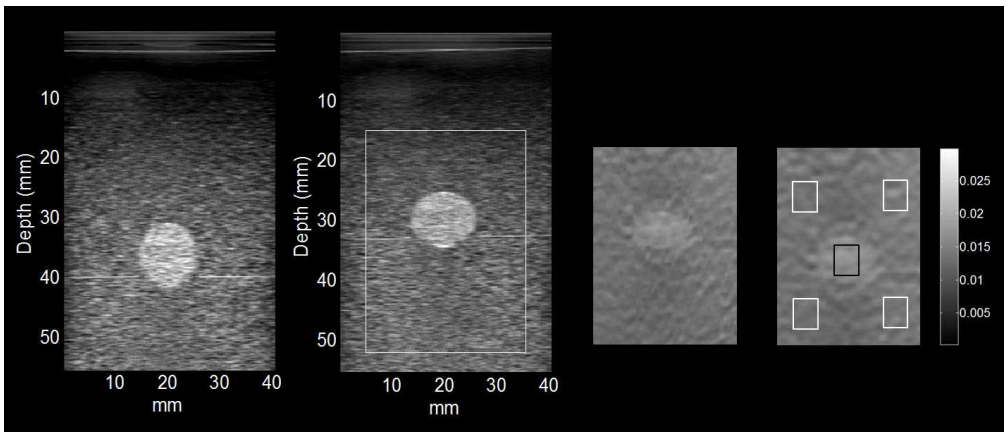

Figure 3.5: From the left to the right are: the B-mode image at no compression the B-mode image at 18.4% pre-compression, the strain images in the original coordinates and 18.4% pre-compression, and the strain image at 18.4% pre-compression with motion compensation. In the last strain image the ROI's are shown. The backgrounds ROI's were chosen to be on the corners in order to diminish the influence of the stress concentration on the contrast and the CNR. The ROI's adopted were the same for the simulations and experimental results.

strain distribution of a medium under uniform compression were described for both 2D cylindrical approaches: plane stress [11] and plane strain [83]. In the same paper Kallel et al. [83] analytically analyzed the observed contrasts and CTE as a function of the materials mechanical parameters. Bilgen and Insana [84] compared the behavior of the CTE curve versus the ratio of the shear modulus of the inclusion to that of the background between both 2D and the 3D spherical approaches using FEA simulation results. They found the background surrounding a cylinder deformed in plane strain has a different strain distribution than a 3D sphere does (the background surrounding a sphere is better approximated in 2D with a cylinder in plane stress), and that a cylinder in plane strain more closely approximates the strain contrast for a sphere that a cylinder in plane stress.

For a given region of interest (ROI) the elastographic SNR is defined as the mean strain ($\overline{e_{ROI}}$) divided by the standard deviation (σ_{ROI}) of the strain

$$\mathtt{SNR} \equiv \frac{\overline{e_{ROI}}}{\sigma_{ROI}}. \tag{3.2}$$

This is a measure of the local noise in a strain image. The CNR is a summary measure that quantifies the detectability of the inclusion in the elastogram

$$\mathtt{CNR} \equiv \frac{2(\overline{e_B} - \overline{e_I})}{\sigma_{eB}^2 - \sigma_{eI}^2}, \tag{3.3}$$

where σ_{eB}^2 and σ_{eI}^2 are the strain variances of the background and the inclusion respectively.

Contrast, CNR and SNR were computed for each image and used to compare equivalent

images obtained from the experiments with tissue mimicking phantom and those created with equivalent FEA simulations. The regions of interest (ROI's) used for image analysis are represented on the motion compensated strain image in figure 3.5. Experimental results for contrast (eq. (3.1)), SNR (eq. (3.2)) and CNR (eq. (3.3)) are the average of values calculated for the four ROI's, and the error bars are the standard deviation. No error bars are provided for the inclusions SNR values because only one ROI was used in the inclusion.

3.2.5 Nonlinear FEA simulation

FEA simulation is a widespread procedure to evaluate theory and algorithms in elastography. Most FEA simulations involved small compressions where it is reasonable to assume linear stress/strain relationships. To perform the 2D nonlinear FEA simulations, a commercial FEA package, ANSYS (ANSYS Inc., Pittsburgh, PA, USA), which has a nonlinear simulation tool, was used. Plane stress (one element dimension is much smaller than the other two) and plane strain (one element dimension is much larger than the other two) configurations were considered and the materials were assumed to be hyperelastic and nonlinear. Stress/strain experimental data is input, and the software fits the data according to the chosen nonlinear energy function (potential energy stored in the material due to a deformation). ANSYS has built into its simulation package some of the well-known nonlinear material models; we used the polynomial model, known as the Mooney-Rivlin model which is suitable for a large range of materials. The background and inclusion stress/strain data were well fit using the 5 terms Mooney-Rivlin polynomial function. During compression, the materials shear moduli are iteratively changed according to the nonlinear fitting.

The compressive forces have vertical directions as depicted in the diagram in figure 3.6(b). Since the simulation is 2D, the inclusions are modeled as being infinitely long 1 cm diameter cylinders perpendicular to the diagram. The final maximum compression applied was 20% of the 10 cm uncompressed height. Since the compression applied is relatively large, a high mesh density - especially close to the junctions between the inclusions and the background - was employed. This procedure helped to minimize distortion of the elements of the mesh. Figure 3.6 shows an example of axial strain simulation response for small (1%) and large (20%) compressions. In this case, the two cylindrical inclusions had different nonlinear characteristics as demonstrated by the difference in contrast at small and large applied compression.

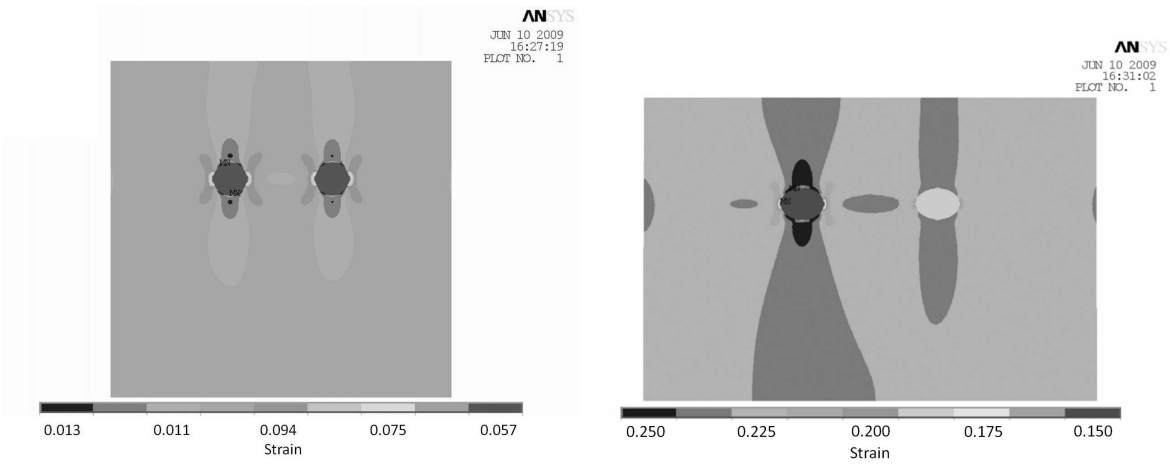

(a) (b)

Figure 3.6: Depiction of the 2D axial strain (ANSYS) at (a) 1% and (b) 20% (right) strain using the plane strain boundary condition.

Table 3.2: Young's storage moduli for pre-compressions of 1% and 23% for all materials in the phantom.

	Storage Young's Modulus (kPa)					
Pre-compression %	BKG 1	BKG 1	Inclusion 1	Inclusion 2	Inclusion 3	Inclusion 4
1	4.90	5.72	15.07	28.02	18.78	12.04
23	52.63	39.38	57.20	204.52	164.45	165.67

3.3 Results and discussion

3.3.1 Mechanical properties of the materials

The results of the storage moduli calculated by the DMA versus pre-compression level obtained from the mechanical tests are shown in figure 3.7. The graph shows the results for both parts of the phantom's background and for all four inclusions. The plots show that the Young's moduli for all materials increased with increasing pre-compression. Table 3.2 shows Young's modulus values at pre-compression levels of 1% and 23%. Figure 3.7 shows that inclusion 1 (an oil-in-gel dispersion) has less increase in Young's modulus with pre-compression compared to the other inclusions and to the backgrounds. On the other hand the materials containing no oil have rates of increase in Young's modulus similar to one another.

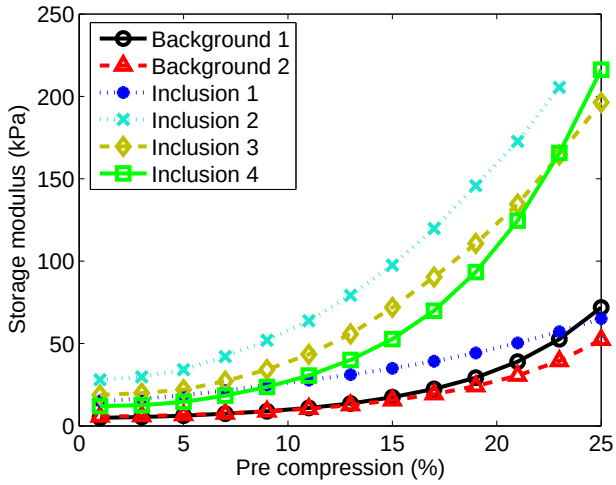

Figure 3.7: Storage moduli versus pre-compression level obtained via DMA, for the two parts of the background and all inclusions.

3.3.2 Experimental and simulation elastograms

Inclusion 1

A B-mode and local strain image of the oil-in-gel inclusion (inclusion 1), are shown in figure 3.8. The values appearing above each strain image indicate the pre-compression. At low pre-compressions the inclusion is stiffer (darker) than the background. However, at large pre-compressions the inclusion is less stiff (lighter) than the background. This observation is confirmed by the contrast and CNR graphs shown in figures 3.9(b) and 3.9(d), respectively. The dashed lines on the contrast graph shows the point ($\sim$10% and 10.5% pre-compression) where the inclusion and the background presented the same stiffness (contrast $\rightarrow$ 0 dB) which also corresponds to the lowest calculated CNR values. For higher compressions the contrast became negative resulting higher CNR (the inclusion was visible again). Figures 3.9(a) and 3.9(c) represent, respectively, the percentage pre-compression vs. frame number, and the SNR vs. percentage pre-compression.

From the figure 3.7 and table 3.2 it is clear that the backgrounds Young's moduli increased with the applied strain faster than the inclusion 1. For 1% pre-compression the Young's modulus ratios between the inclusion and the background are approximately of 1:3.1 and 1:2.6 for background parts 1 and 2 respectively, while for 23% pre-compression they were 1:1.1 and 1:1.45, respectively. From these data, it is expected that with increasing pre-compressed the phantom background became stiffer faster than the inclusion causing the contrast to decrease and then invert (changing from dark to bright compared to the background).

The strain images in figure 3.8 and the contrast graph in figure 3.9(b) confirm the expec-

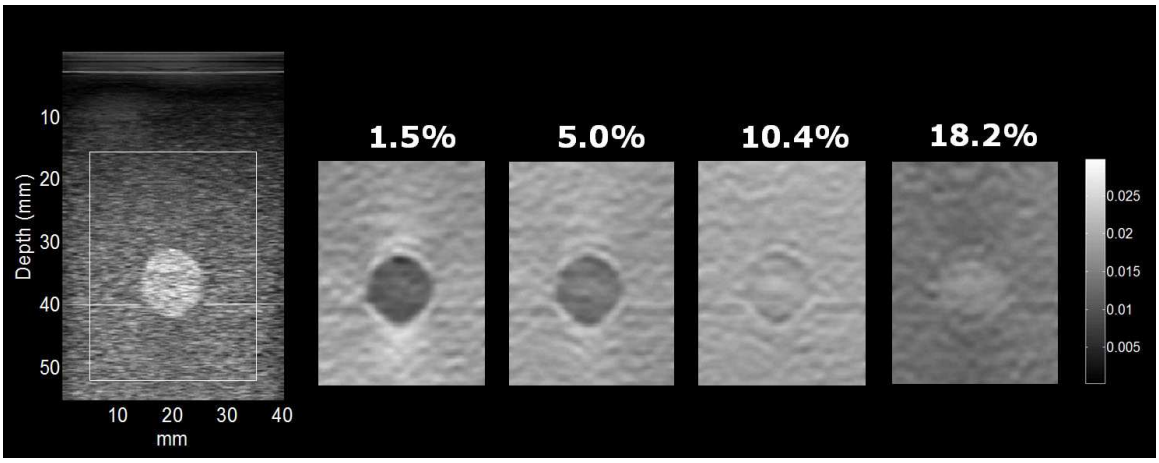

Figure 3.8: A B-mode image of the inclusion 1 (left) and four strain images for different pre-compression axial strain (in percent) are represented. The strain image contrast changes with the applied pre-compression.

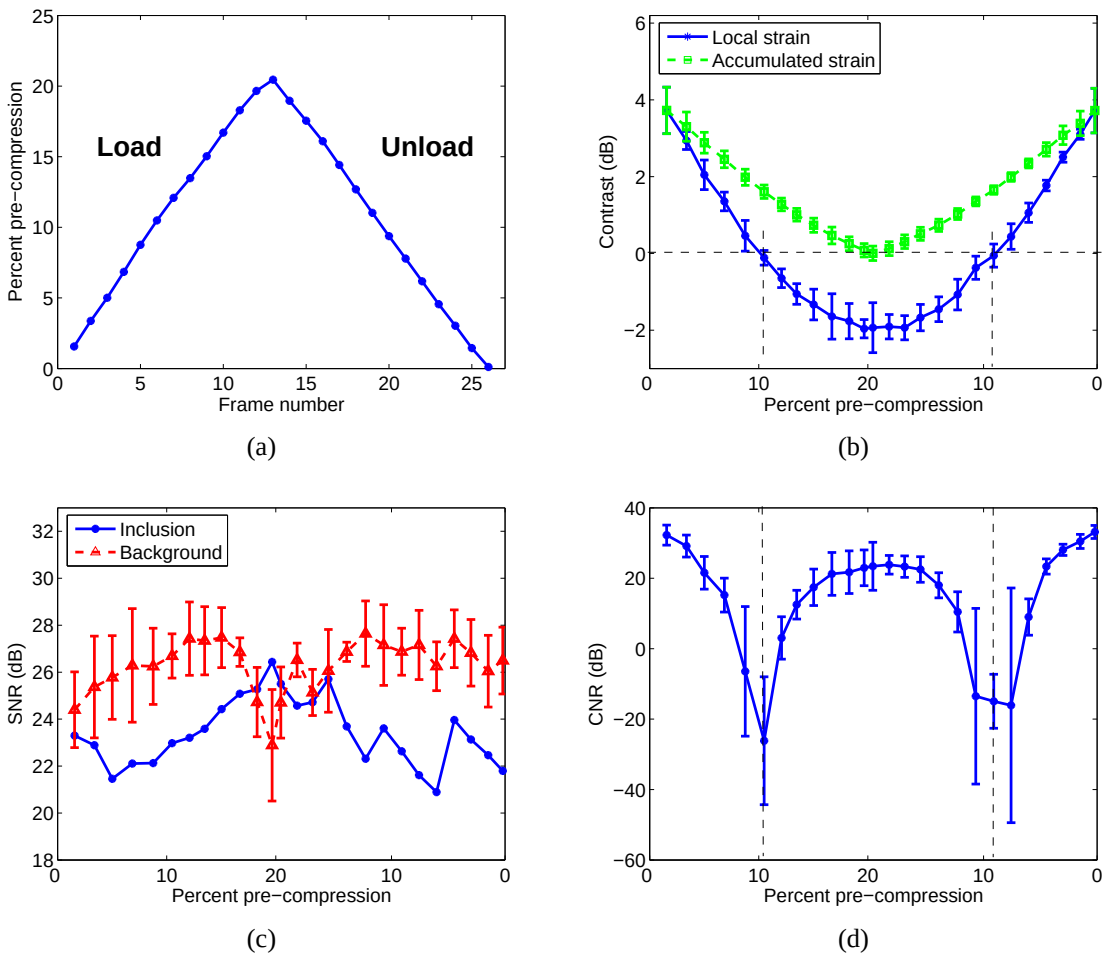

Figure 3.9: Quantitative results obtained for the inclusion 1 using the ROI's represented in figure 3.5: (a) accumulated average strain for each frame (b) contrast for the local strain and for the accumulated strain during load and unload (c) SNR for the inclusion and the background calculated from the local strains and (d) CNR calculated from the local strains data.

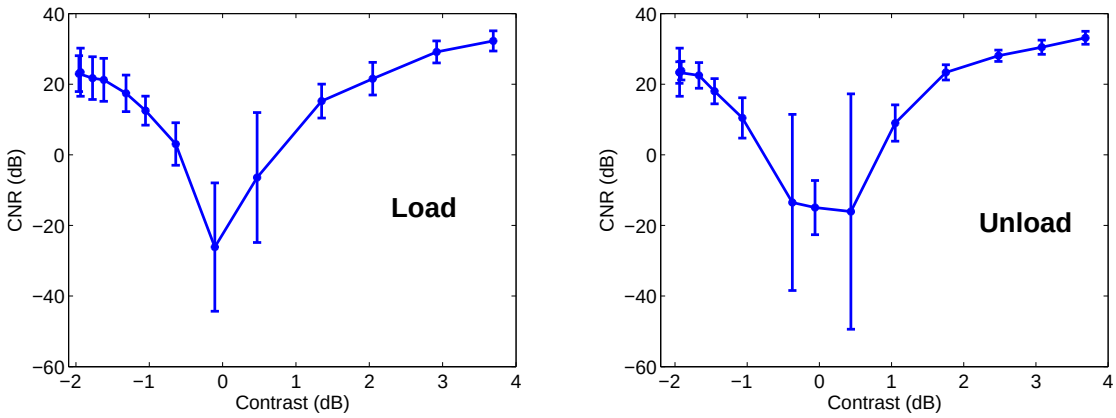

(a) (b)

Figure 3.10: Plots of the CNR versus contrast: (a) loading path; (b) unloading path. The CNR becomes very small (negative dB) when contrast is near zero.

tations of deformation-dependent strain image contrast for inclusion 1, and a contrast reversal was observed for overall averaged strain of around 10%. In figure 3.9(d), the contrast reversal is indicated by the point of lower and negative CNR. The behavior of the CNR data versus contrast (figure 3.10) is in agreement with the behavior of the upper bounds between the contrast and CNR analytically analyzed (plane strain) by Varguese and Ophir [85]. The CNR and the contrast decreased while the inclusion remained stiffer than the background. At larger deformations, beyond this point, the inclusion became softer therefore again becoming visible as suggested by the CNR increase. In Varguese and Ophir [85] theory, the CNR was forced to be null for elastograms presenting no contrast between the inclusion and the background (contrast $\rightarrow$ 0dB). In our case the CNR for near-zero contrast ($\sim$ 0 dB), is negative (in dB; very small) and with larger error bars, meaning that the inclusion could not be visualized.

The SNR curves (figure 3.9(c)) demonstrated that the background SNR remained fairly constant ($\sim$25 dB) throughout all images, while the inclusion SNR increased for larger accumulated strains. It can be understood by the fact that the amount of strain experienced by the background between a pair of frames used in the processing was quite constant ($\sim$ 1.5%). On the other hand, the strain experienced by the inclusion increased with the applied strain since it became softer, allowing the SNR to increase.

The contrast in accumulated strain images (plotted in figure 3.9(b)) versus the loading path from 0 to 20% was used for comparison with two versions of 2D FEA simulation. Figure 3.11 shows plots of experimental strain image contrast versus pre-compression for inclusion 1 compared to FEA-predicted contrast based on the material property measurements (shown in table 3.1 and figure 3.7). Error bars on the experimental contrast values were obtained from the four ROI's in the background (figure 3.5). The error bars on the FEA curves are the range of values

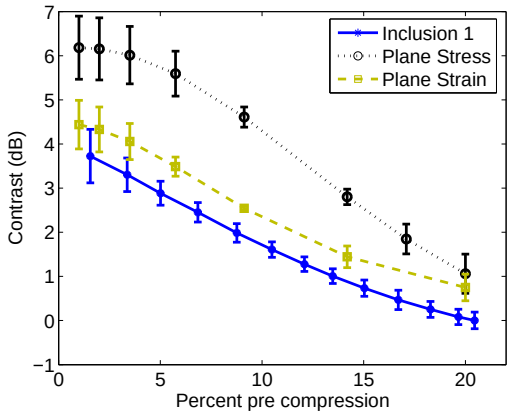

Figure 3.11: Comparison between 2D FEA simulations and experimental axial accumulated strain contrasts for the inclusion 1. FEA results are shown for the plane stress and plane strain boundary condition.

obtained from the simulation using stress/strain data from the part 1 and 2 of the background, while the points indicate contrast obtained using the mean values. The agreement was quite good when plane strain boundary conditions were adopted. However, there was a nearly constant 0.7 dB contrast overestimation for the plane strain case over the entire 0-20% range of pre-compression. Strain image contrast predicted with plane stress boundary conditions were in much poorer agreement. This is consistent with predictions from Bilgen and Insana [84].

Inclusions 2, 3 and 4

Figures 3.12(a), 3.12(b) and 3.12(c) show B-mode images and local strain images for inclusions 2, 3 and 4. Two local strain images are shown for each inclusion: one for low and the other for large accumulated strains. The accumulated axial strains are again indicated above each elastogram. The contrast decreased for all three cases; however, none of spheres became less stiff than the background (negative contrast). This fact is confirmed by the contrast curves (Figures 3.13(a) and 3.13(b)). Those two graphs demonstrate that initially the inclusions had distinctly contrasts which tended to become similar to each other with the applied strain. Figures 3.13(c) and 3.13(d) show the CNR for all cases. This parameter was always above 0 dB meaning that the inclusions could be visualized for applied overall strains up to 20%.

The Young's modulus values for inclusions 2, 3 and 4 (figure 3.7 and table 3.2) show that the elastic nonlinearity of these materials were similar to that for the backgrounds. Table 3.3 represents storage modulus ratios between inclusion and background for pre-compression levels of 1% and 23%.

At first thought one might think that the strain image contrast for each of these inclusions

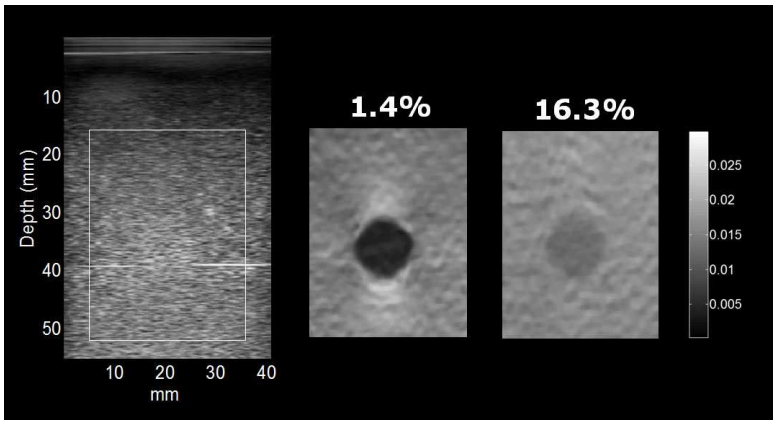

(a)

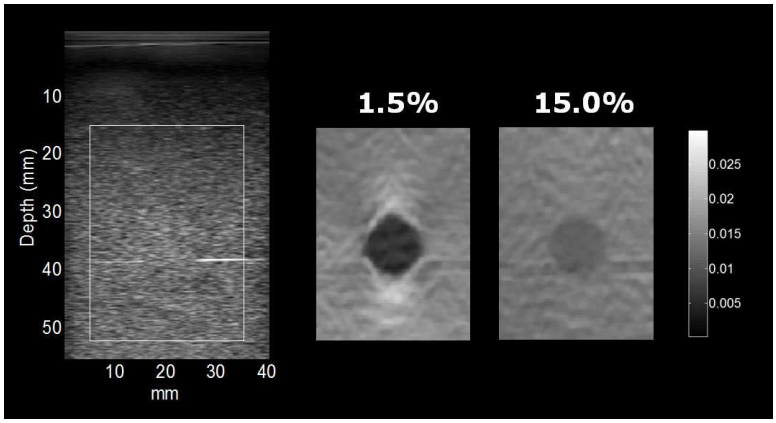

(b)

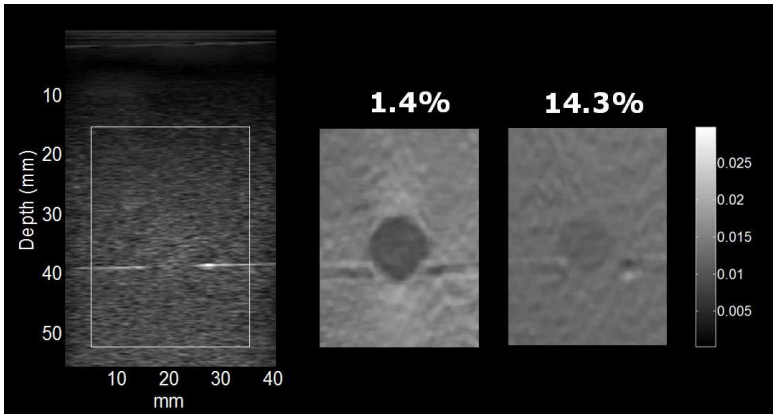

(c)

Figure 3.12: B-mode (left) and incremental strain images for inclusions 2, 3 and 4 corresponding to figures (a), (b) and (c), respectively. The images in the center and right side are respectively, local strain images for small ($\sim$ 1.5%) and large ($\sim$ 15%) pre-compression.

Table 3.3: Young's modulus ratios between the inclusions and the backgrounds for low (1%) and high (23%) pre-compression.

	Inclusion 2		Inclusion 3		Inclusion 4	
Pre-compression	1%	23%	1%	23%	1%	23%
Background 1	1:5.7	1:3.9	1:3.8	1:3.1	1:2.5	1:3.2
Background 2	1:4.9	1:5.2	1:3.3	1:4.2	1:3.1	1:4.2

would be constant regardless of pre-compression since the nonlinear behavior of inclusions and backgrounds were similar. However, the strain images in figure 3.12 and the contrast graphs in figures 3.13(a) and 3.13(b) show that the contrast decreased for higher pre-compression for all three inclusions. Oberai et al. [34] found similar results in their nonlinear reconstructions. In their case the fibroadenoma strain images had higher contrast for low applied strains, but their nonlinear reconstruction showed that the inclusion had about the same nonlinear behavior as the surrounding tissues.

The explanation provided by Oberai et al. [34] was simple and is consistent with our observations. Assume for the moment that the overall strain in the background was 1% and that the stress experienced by the inclusion was almost the same as the stress in the background. Assume also that the inclusion is ten times stiffer than the background. The strain experienced by the inclusion is lower (approximately 0.1%) than that in the background (ignoring the details of contrast transfer efficiency). Now consider what happens when the strain experienced by the background is 15% (as in figure 3.12). Again assume that the incremental stress in the inclusion and background are the same. The fact that the background was softer permits it to experience higher strains, and since it has a nonlinear stress/strain relationship, it stiffens more than the inclusion. Since the background has stiffened relative to the inclusion, its modulus is now closer to that of the inclusion and they undergo strains that are more similar (lower strain image contrast) than at lower pre-compression. This behavior was the observed in figures 3.13(a) - 3.13(b) where inclusion 2 (harder) presented the highest decrease in contrast, while inclusion 4 (softer) presented the lowest.

As with contrast, the CNR also decreased with applied strain (figures 3.13(c), 3.13(d)). The CNR versus contrast plots (figure 3.14) were again in agreement with the behavior of the upper bounds between the contrast and CNR [85]. In the regions where the contrasts values coincide, the CNR values do also. The plots in figure 3.14 illustrate that the range of contrast among these nonlinear inclusions and background was much higher for the harder inclusions.

Figure 3.15 shows the elastographic SNR's in the backgrounds and inclusions as a function

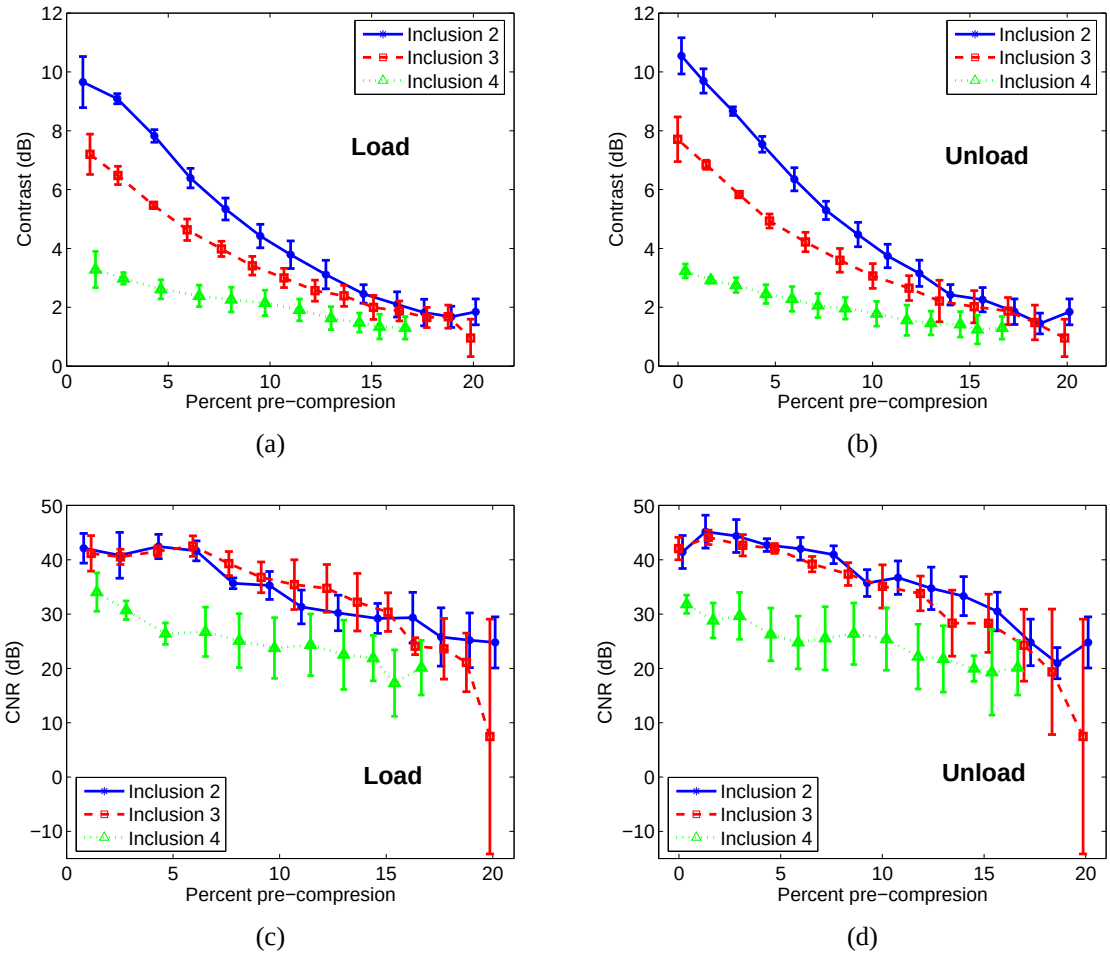

Figure 3.13: The contrast of the local strain images versus the pre-compression for inclusions 2, 3 and 4 in loading (a) and unloading (b). CNR of the local strain images versus pre-compression are shown in loading (c) and unloading (d).

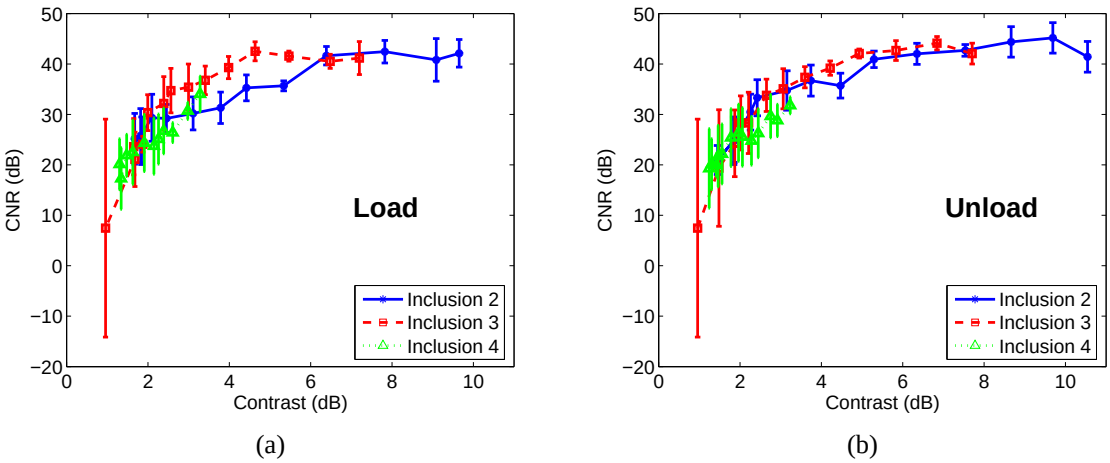

Figure 3.14: Plots of the CNR versus contrast for the inclusions 2, 3 and 4: (a) loading path; (b) unloading path.

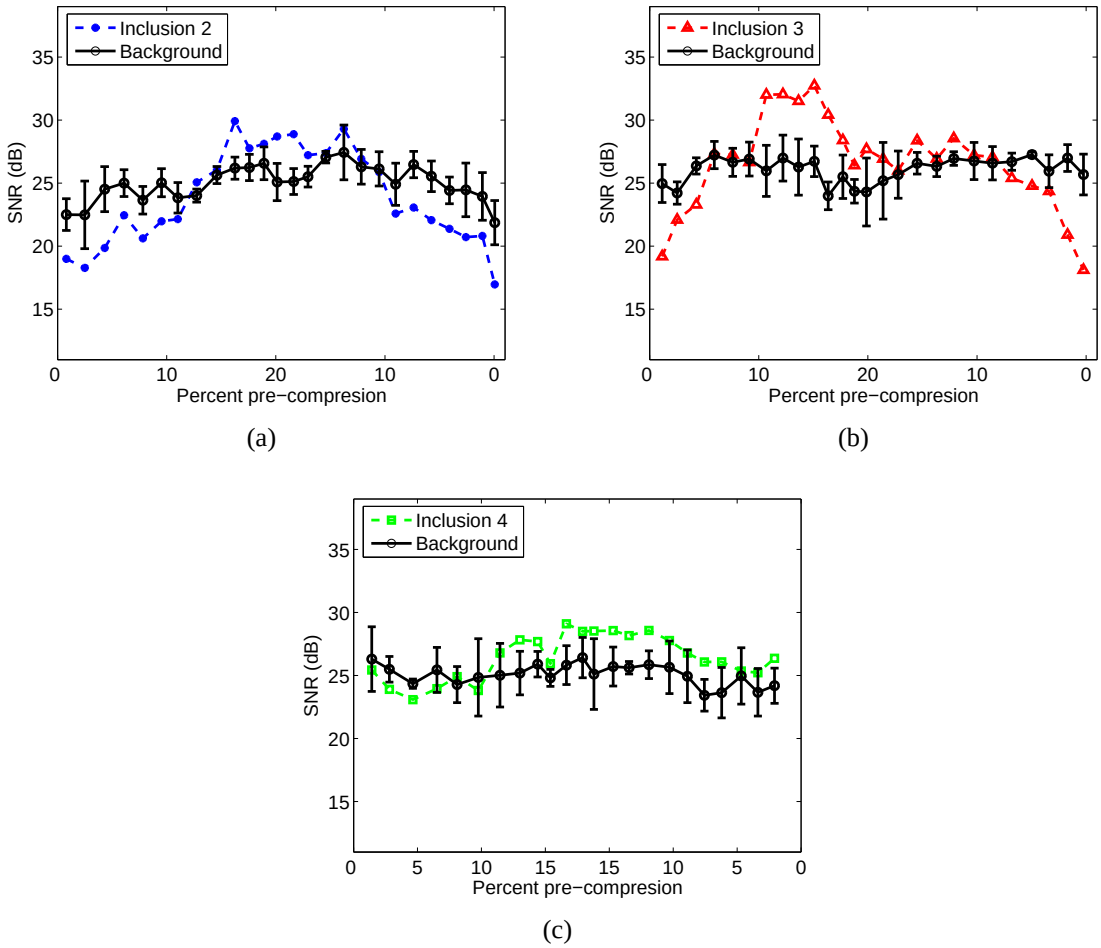

Figure 3.15: Backgrounds and inclusions SNR's: (a) inclusion 2; (b) inclusion 3; (c) inclusion 4.

of applied pre-compression. As discussed in section 3.3.2 the SNR curves demonstrated that the background SNR remained fairly constant (∼25dB) throughout the images for all inclusions, while the inclusion SNR increased for larger accumulated strains. The range of values experienced by the inclusions 2 and 3 (harder) are higher than the values for the inclusion 3. It can be understood by the fact that the strain experienced by harder inclusions is lower resulting in lower signal values, causing SNR below 20 dB, while softer inclusions experienced higher strain resulting in SNR higher than 30 dB. In addition to that, the SNR for lower strains can also be decreased by the fact that the strain filter theory states that for lower strains (<1.5%) the upper bounds for the SNR are smaller [86].

The comparison between the experimental strain image contrast and that from the FEA simulations (plane stress and plane strain) are shown in figure 3.16 for inclusions 2, 3 and 4. Quantitative agreement was quite good for all inclusions when the plane stress configuration was adopted. However, there was contrast underestimation of 1 dB to 2 dB in the plane strain case.

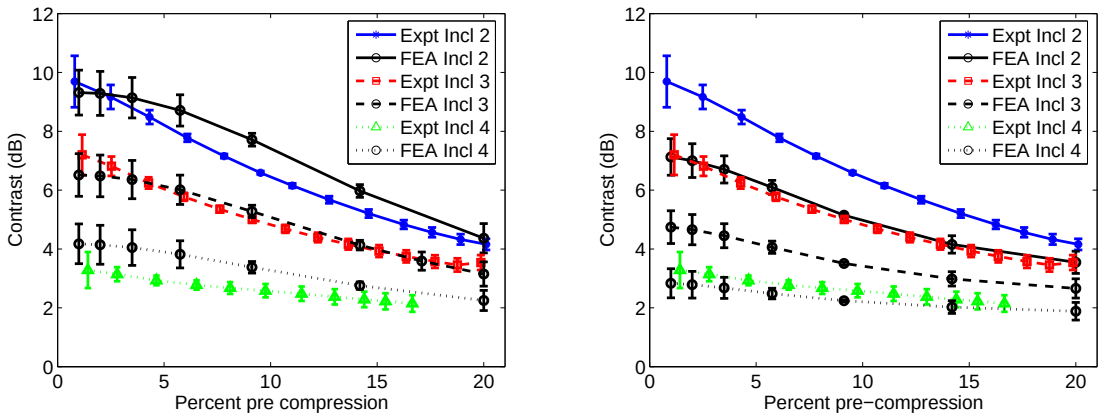

(a) (b)

Figure 3.16: Comparison between the FEA simulated and the experimental accumulated axial strain contrasts versus percent pre-compression obtained for the inclusions 2, 3 and 4: (a) shows the plane stress FEA; (b) shows the plane strain FEA.

It is worthwhile to compare the results obtained with Inclusions 1 and 3. As shown in table 3.2, these materials have similar elastic modulus at small strain but very different nonlinearity. Since the nonlinearity of the background is higher than that for inclusion 1, they have similar elastic modulus at 10% strain and therefore Inclusion 1 provides zero contrast at that deformation. However, since inclusion 3 has nonlinearity similar to the background, it retains contrast relative to the background at the maximum strain applied (20%).

3.4 Summary

This chapter presented an experimental approach to evaluate changes in contrast, SNR and CNR between inclusion and background for large deformations (up to 20%) when the stress/strain relationship for the materials is nonlinear.

The change in contrast over a large deformation range predicted by the FEA simulations was consistent with that experimentally observed. An inclusion with lower nonlinearity than the background demonstrated strain image contrast inversion. Stiffer inclusions presented faster decrease in contrast than softer inclusions when both have the same nonlinear behavior as the background. These differences can all be explained by analyzing the relative nonlinear behavior of the constituent materials.

The nonlinear elastic behavior of the media being imaged may not improve the quality of the strain images but might provide additional information which can be useful to differentiate types of materials or tissues.

4 Acoustic pressure field of a spherical focused transducer

4.1 Introduction

Commonly, the radiation pattern generated by a flat circular transducer is found through the integration of the Green's function over the transducer, as formulated by Rayleigh. For a focused transducer, the Rayleigh formula is an approximation and is good if the radius of the transducer is larger than the wavelength [87].

The intensity distribution is not trivial, hence the double integral is indicated to solve the problem [87]. Efforts were done to reduce the solution to a single integral [88, 89]. Chen et al. [90] proposed a numerical solution, which is a summation of a one integral solution. Based on this solution, the pressure fields presented in this chapter and the point spread functions (PSF) of a imaging system where a confocal transducer - center disk and an outer ring that introduce two coaxial confocal ultrasonic beams to the same focal spot (figure 4.1(a)) - is employed, were developed [91].

This chapter provides a brief introduction about the acoustic pressure field produced by

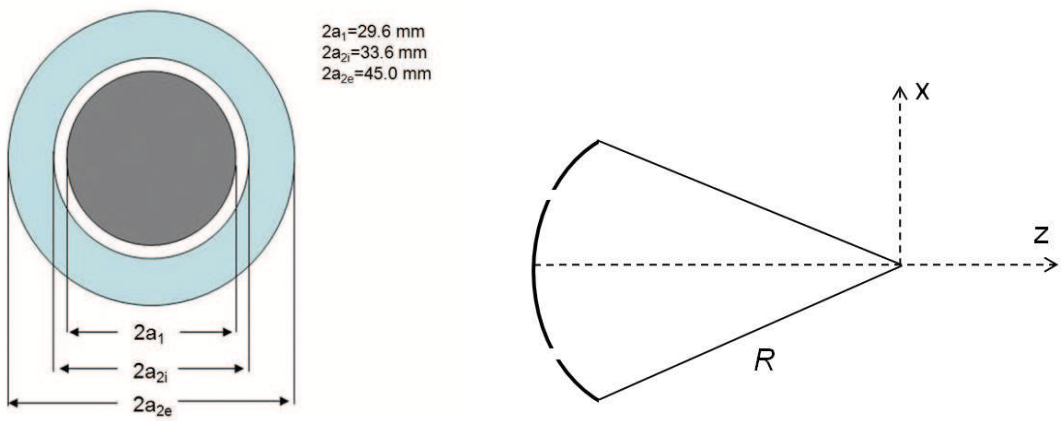

(a) (b)

Figure 4.1: Diagram showing the confocal transducer and beam forming geometries.

spherically focused sources composing a confocal transducer being driven by continuous wave (CW). The experimental results were compared to the solution proposed by Chen et al. [90].

4.2 Materials and Methods

4.2.1 Mathematical background

Single-element spherical focused transducer

Consider the central disk of the confocal transducer of radius a_1 and focal length (radial curvature) R, as shown in figures 4.1(a) and 4.1(b). We assume the ultrasonic beam is propagating in a lossless medium. The resulting pressure amplitude function at the focal plane and the pressure amplitude function along the transducer axis are [90]

$$p(r,t) = p_0 \frac{\pi a_1^2}{\lambda_0 R} jinc\left(\frac{r a_1}{\lambda_0 R}\right) \cos(\omega_0 t + \psi_0(r)) \tag{4.1}$$

$$p(z,t) = p_0 \frac{R}{z} \left| 1 - \exp\left(\frac{i\pi a_1^2}{2\lambda_0 R} \cdot \frac{z}{R+z}\right) \right| \cos(\omega_0 t + \psi_0(a_1,z)) \tag{4.2}$$

where $r = \sqrt{(x^2+y^2)}$ is the radial distance, $p_0 \equiv \rho_0 c v_0$ can be understood as the equivalent pressure amplitude on the transducer surface, v_0 is the amplitude of the velocity at the transducer surface, ρ_0 and c are, respectively, the density and sound speed in the medium, ω_0 is the angular central frequency, λ_0 is the acoustic wavelength, $jinc(x) = J1(2\pi x)/\pi x$, $J1(\cdot)$ is the cylindrical Bessel function of order 1, $\psi_0(r)$ and $\psi_0(a_1,z)$ are the phase functions.

Confocal trasnducer

The pressure from a two-elements spherically focused transducer consisting of a central disk (radius a_1) and an outer ring (inner radius a_{2i} and outer radius a_{2e}) arranged in confocal and coaxial geometry is evaluated. Consider that the elements of the confocal transducer are simultaneously excited by separate unmodulated CW sinusoidal signals with frequencies $\omega_1 = \omega_0 + \Delta\omega/2$ and $\omega_2 = \omega_0 - \Delta\omega/2$. The pressure of the amplitude modulated field that arises in the region where the beams interact at the focal plane is

$$p(r,t) = P_1(r)\cos(\omega_1 t + \psi_1(r)) + P_2(r)\cos(\omega_2 t + \psi_2(r)). \tag{4.3}$$

$P_1(r)$ and $P_2(r)$ are amplitude functions given by [92]

$$P_1(r) = p_0 \frac{\pi a_1^2}{\lambda_1 R} jinc\left(\frac{r a_1}{\lambda_1 R}\right) \tag{4.4}$$

and

$$P_2(r) = p_0 \frac{\pi}{\lambda_2 R}\left[a_{2e}^2 jinc\left(\frac{r a_{2e}}{\lambda_2 R}\right) - a_{2i}^2 jinc\left(\frac{r a_{2i}}{\lambda_2 R}\right)\right]. \tag{4.5}$$

Following the same procedure, the resulting pressure field along the z axis can be written as:

$$p(z,t) = P_1(z)\cos(\omega_1 t + \psi_1(z)) + P_2(z)\cos(\omega_2 t + \psi_2(z)). \tag{4.6}$$

Rewriting (4.2), the amplitude functions $P_1(z)$ and $P_2(z)$ can be given as:

$$P_1(z) = p_0 \frac{R}{z}\left|1 - \exp\left(\frac{i\pi a_1^2}{2\lambda_1 R}\cdot\frac{z}{R+z}\right)\right| \tag{4.7}$$

and

$$P_2(z) = p_0 \frac{R}{z}\left|\exp\left(\frac{i\pi a_{2i}^2}{2\lambda_2 R}\cdot\frac{z}{R+z}\right) - \exp\left(\frac{i\pi a_{2e}^2}{2\lambda_2 R}\cdot\frac{z}{R+z}\right)\right|. \tag{4.8}$$

The eqs. (4.1), (4.2), (4.3) and (4.6) describe the pressure distribution at the focal plane, and along the ultrasonic beam axis for a single element spherically focused transducer and an annular array confocal transducer. The pressure field of the central disk composing the transducer, shown in figure 4.2, was evaluated and compared with the theoretical predictions. The experimental procedure is described in section 4.2.2. From the equations describing the pressure field of the confocal transducer, the PSF of the system was evaluated and is described in chapter 5.

4.2.2 Experiment

The confocal transducer with focal depth of 7 cm has dimensions according to figure 4.1(a). The confocal transducer construction is shown in figure 4.2. The photographs of the PZT4 elements and the transducer in its final shape are shown in figures 4.2(a) and 4.2(c), respectively.

The central disk element acoustic field was measured in a water tank with dimensions of 1.60 x 80 x 80 cm using a needle hydrophone (HNP-0400, Onda). A three axes motorized system placed over the tank was used to scan the acoustic field. This system was controlled through a control board (PCI - 7340, National Instruments), and LabView software. The transducer cen-

(a) (b) (c)

Figure 4.2: Confocal transducer construction. (a) PZT4 elements arranged in confocal geometry; (b) assembling the ultrasonic transducer parts; (c) confocal ultrasonic probe used in the experiments.

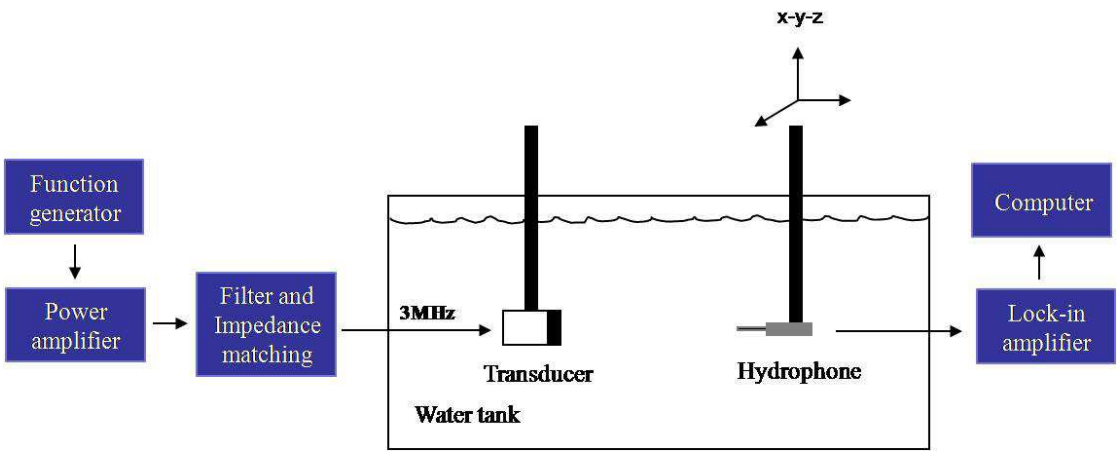

Figure 4.3: Simplified diagram showing the experimental setup used for measuring the acoustic field.

tral disk was driven with CW through an arbitrary waveform generator (AFG320,Tektronix), and a homemade 20 dB radiofrequency (RF) amplifier. To avoid noise and other interfering signal a bandpass filter with 30% of bandwith and central frequency coinciding with the transducers central frequency (3 MHz) was used before driving the transducer.

The receiving needle hydrophone was mounted on the x-y-z system. This hydrophone was positioned so that its axis of symmetry was horizontal and passed through the center of the transmitter. To obtain the image representation of the acoustic field, the hydrophone was moved across the scanning plane. The acoustic pressure was received by the hydrophone at each scanning position and recorded through a RF Lock-in amplifier (SR-844, Standford Research Systems). Figure 4.3 shows a diagram of the experimental setup.

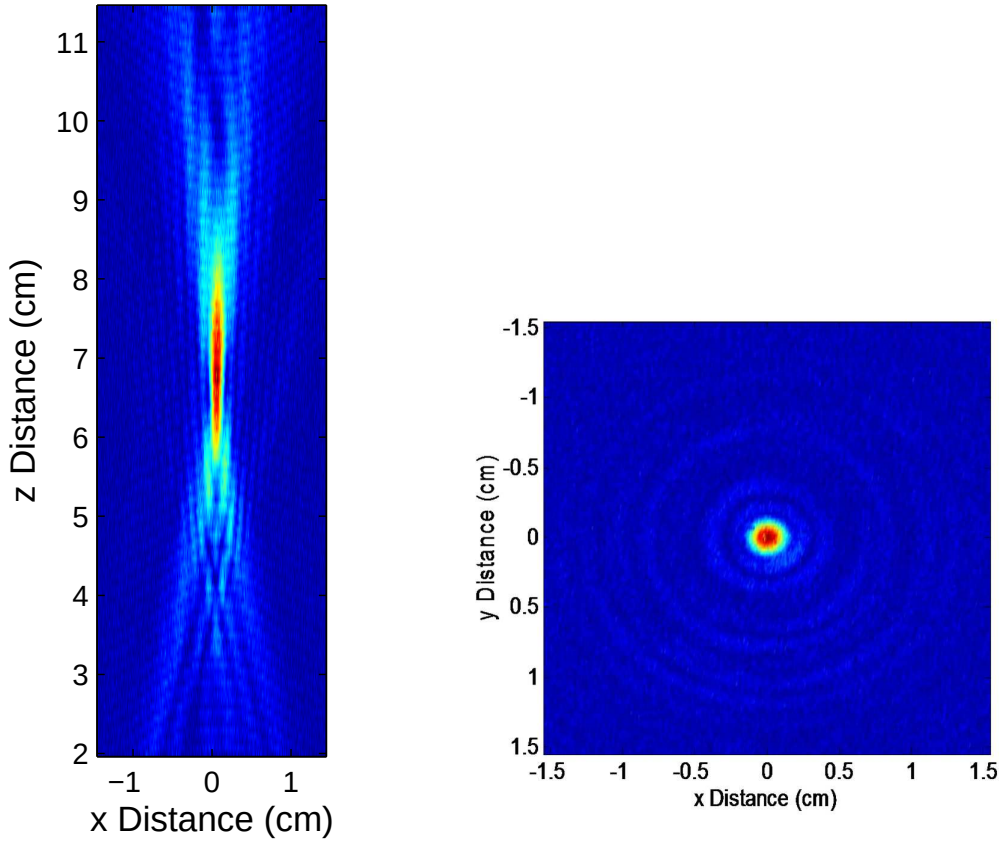

(a) (b)

Figure 4.4: Transducer central disk acoustic pressure field images (a) x-z plane and (b) x-y plane.

4.3 Results and discussion

The acoustic field images of the transducer central disk are shown in figure 4.4(a) (perpendicular to the transducer surface passing through its center, x-z plane) and figure 4.4(b) (parallel to the transducer surface at the focal point, x-y plane). The distance values displayed on the images are the axial and lateral distances from the center of the confocal transducer.

For the adopted transducer geometry, the pressure field is symmetrical about the z axis; therefore, only the profiles along the z and x axes were evaluated. Figure 4.5(a) and figure 4.5(b) show the plots of the normalized (to unity) pressure profiles of the axial and lateral axes, respectively. The dashed lines are the experimental and solid lines the theoretical results.

The theory developed by Chen et al. [90] to describe the acoustic radiation pressure pattern produced by a single-element focused transducer was experimentally verified through the measurement of the confocal ultrasonic transducer acoustic pressure field. The axial z profile

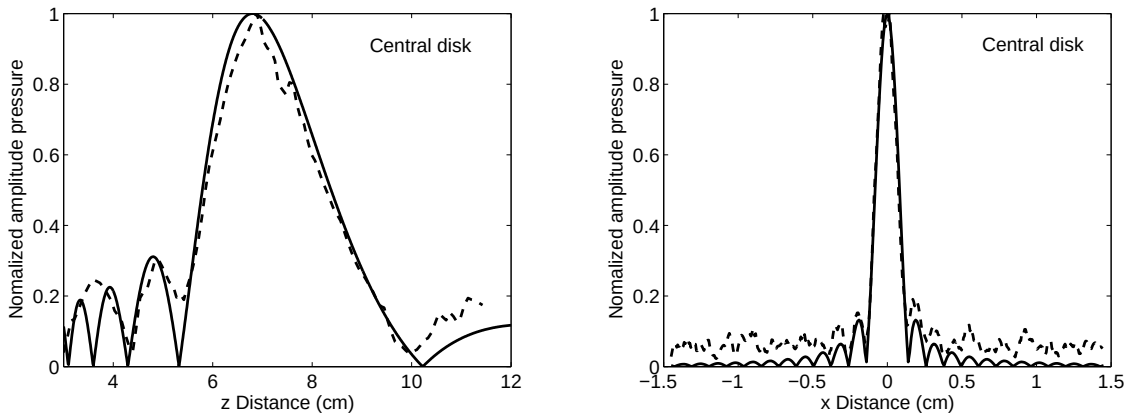

(a) (b)

Figure 4.5: Normalized pressure amplitude (a) axial and (b) lateral profiles. Dashed lines are the experimental and solid lines are theoretically simulated results.

(figure 4.5(a)) main lobe agree well with theoretical prediction, whereas the small lobes closer to transducer differed a bit. The measured main and side lobes of the lateral x profile agree well with the simulated result (figure 4.5(b)).

In this chapter, the pressure field profile of a transducer commonly used in vibro-acoustography [92] was studied. This confocal geometry provide a beam interference where the two beams meet. This interference generates a confined oscillatory force with frequency equivalent to difference of frequencies driving the two ceramics. Furthermore, no oscillatory force is exerted on the transducer element itself; hence, no interfering signal is produced by the transducer. In vibro-acoustography the acoustic signal emitted by the vibrating object target is recorded by a hydrophone [92].

4.4 Summary

The axial and lateral pressure amplitude profiles agreed quite good with the theoretical plots obtained based on the numerical solution of the Green's function [90]. The transducer axial focus dimension was almost ten times greater then the lateral, meaning that an imaging system using this kind of transducer will have a better lateral resolution.

5 Continuous wave Doppler measurement of acoustic radiation force-induced vibration

5.1 Introduction

Several ultrasound elasticity imaging systems were developed in the last few years. Some of them employ acoustic radiation force as a means of internally pushing the tissue, such as: vibro-acoustography [46], acoustic radiation force impulse (ARFI) imaging [38] and harmonic motion imaging (HMI) [93]. In Vibro-acoustography and HMI, amplitude modulated (AM) ultrasonic forces are used to vibrate the target [46, 93].

In HMI, this vibration is promoted by a focused single-element transducer transmitting ultrasonic waves, and the movement is detected trough a mono-channel pulse-echo ultrasound system [93]. In vibro-acoustography, a confocal ultrasound transducer with two elements is employed. The central disk and annular elements of this transducer are driven with slightly different frequencies. The ultrasonic beams interact in the focal zone, producing an AM force, which induces vibrations, in the range from few nanometers to micrometers, to the tissue [46]. Usually, the response is measured through a hydrophone [46] or a laser Doppler vibrometer [91]. The fact that the hydrophone is not directional and the laser is not capable of measuring inside opaque media, as the biological tissue, are intrinsic restrictions of these methods. Zheng et al. [94] proposed a method using a pulse-echo single channel ultrasound system, a Doppler algorithm and the Kalman filter to estimate the amplitude and phase of the micro-vibrations induced by dynamic radiation force, generated by the confocal transducer. The authors measured the parameters of the shear waves induced by the oscillatory movement.

Continuous wave (CW) Doppler ultrasound is an alternative method to detect the vibration. This apparatus is easily found (e.g. fetal Doppler) and the response is fast, since the echoes are electronically processed, using quadrature demodulation, in real-time. Vibration measurement using CW Doppler has been used as alternative, to optical sensor, e.g., for measuring vibrations

of rough surfaces [95].

For a vibrating target, the Doppler analysis can involve more complex techniques than the usual, and has been the center of debate [96, 97]. This chapter does not intend to go into details on the different techniques available to estimate the vibration parameters through CW Doppler systems. The goal is to demonstrate the feasibility of measuring vibrations induced by focused confocal beams, and the ability to form images of a rigid spherical inhomogeneity embedded in viscoelastic phantom by scanning both ultrasonic transducers (confocal and Doppler) across the confocal transducer focal plane. For a detailed description of different methods to estimate the oscillatory motion parameters, the reader is referred, for example, to Ref. [98]

5.2 Materials and methods

Here, the dynamic acoustic radiation force was induced by the interaction of two CW confocal and coaxial ultrasonic beams with slightly different frequencies produced by an annular two-elements transducer. The amplitude and phase of the induced movement depend on the mechanical properties of the medium, and were detected using a conventional CW ultrasound Doppler (fetal Doppler, Sigmed, model DM 200) system, in which the transducer is composed by two plane elements; one is used to continuously transmit the acoustic waves and the other is used to detect the echoes. The velocity and direction of the induced motion are estimated through phase quadrature demodulation of the echo signal.

5.2.1 Doppler measurement of oscillatory movement

The theory presented here is based on the ultrasonic interferometer, which uses the demodulation system, see for example Ref. [99].

The voltages applied to the Doppler transducer transmitter element ($v_T(t)$) and emitted by the receiver element ($v_R(t)$) can be written as:

$$v_T(t) = V_T \cos(\omega_0 t) \tag{5.1}$$

$$v_R(t) = V_R \cos(\omega_0 t + kx(t)) \tag{5.2}$$

where V_T and V_R are the amplitudes of the transmitted and received voltage respectively, ω_0 is the angular frequency of the carrier wave, k is the wave number and $x(t)$ is the round trip path length of the transmitted wave, before reaching the receiver element.

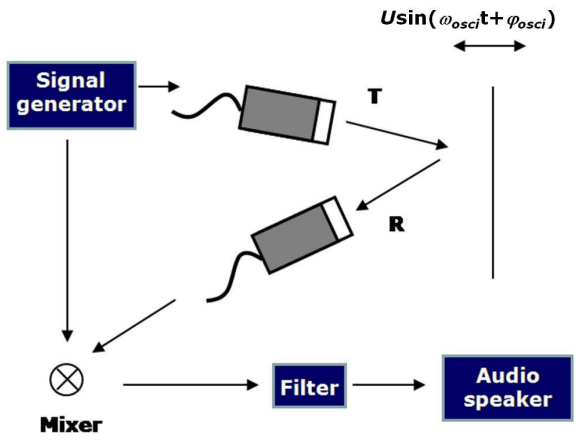

Figure 5.1: CW Doppler system used to detect the movement of an oscillatory backscattering. The signal describing the received wave is multiplied by a reference signal identical to the applied to the transmitter element.

The amplitude of the modulated focused force induces a sinusoidal movement to the target. This movement can be given as:

$$u(t) = U\sin(\omega_{osci}t + \varphi_{osci}) \tag{5.3}$$

where ω_{osci} is the vibration frequency, φ_{osci} is the phase and U is the amplitude of the oscillatory movement. Figure 5.1 shows the schematic procedure of an oscillatory target movement detection using a conventional CW Doppler system. Now, the distance from the scatter to the Doppler transducer is varying over time $x(t) = 2x_0 + 2u(t)$, where x_0 is the distance from the scatter's mean position. In this case, the received signal is

$$v_R(t) = V_R\cos[\omega_0 t + \beta\sin(\omega_{osci}t + \phi_{osci}) + 2kx_0]. \tag{5.4}$$

Equation (5.4) shows that the received signal is a pure-tone frequency modulated signal, β is the modulation index proportional to the displacement of the target

$$\beta = \frac{2U\omega_0\cos(\Theta)}{c} \tag{5.5}$$

where Θ is the angle between the vibration direction and c is the speed of sound in the medium. Multiplying eqs. (5.1) and (5.2) (the first step of a quadrature demodulation procedure) and substituting the parameters observed in eqs. (5.3) and (5.4), a signal composed by one higher and one lower frequency component is obtained

$$s(t) = \frac{1}{2}V_T V_R\left\{\cos[2\omega_0 + \beta\sin(\omega_{osci}t + \phi_{osci}) + 2kx_0] + \cos[\beta\sin(\omega_{osci}t + \phi_{osci}) + 2kx_0]\right\}. \tag{5.6}$$

The first term in eq. (5.6) contains the higher frequency component and the second term is the

difference term, which contains only the oscillatory movement information. After applying a low pass filter the following equation is obtained

$$s(t) = \frac{1}{2} V_T V_R \cos[\beta \sin(\omega_{osci} t + \varphi_{osci}) + 2kx_0]. \tag{5.7}$$

At positions where $(\omega_0/\lambda)x_0 = (\pi/2) \pm n\pi$, the Doppler system has its maximum sensibility, and eq. (5.7) can be reduced to:

$$s(t) = \frac{1}{2} V_T V_R \sin[\beta \sin(\omega_{osci} t + \varphi_{osci})] \tag{5.8}$$

Considering $\beta << 1$ the result is a sinusoidal signal with the same frequency as the vibrating target:

$$s(t) = \frac{1}{2} V_T V_R \beta \sin(\omega_{osci} t + \varphi_{osci}). \tag{5.9}$$

Equation (5.9) shows that the output voltage of the instrument is dependent of the reference and the received voltage magnitudes, and is proportional to the vibration amplitude of the target.

There are reports of different techniques to estimate the velocity and frequency of the vibration through the time-domain and the power spectrum of the received echo. The fraction of the vibration cycle used for the analysis, the nonlinearity of the medium, a *priori* knowledge of the vibration frequency, and the vibration velocity can determine which technique is more efficient. Going into these details is not the aim of this chapter, for a more detailed description about estimating harmonic vibration by ultrasound Doppler method, the reader is referred to Ref. [98].

In our experiments, we used a commercial mono-channel fetal Doppler ultrasound that uses the demodulation technique. We were unable to access the amplitude of the transmitted and received ultrasonic signals, which are parameters necessary to estimate the amplitude of oscillation, as stated by equations (5.7) to (5.9). Equation (5.7) shows that the Doppler output signal is highly dependent of the distance between the transducer and the oscillatory target, what makes more difficult the assessment of the vibration amplitude. To estimate the vibration velocity through a CW ultrasound Doppler system, the easiest way is to calibrate it using a gold standard method, as a laser vibrometer [100]. However, relative values are easily assessed, what motivated us to use the CW Doppler system to obtain images, where the brightness level is proportional to the vibration amplitude.

5.2.2 Acoustic radiation force

The acoustic radiation force arises when the acoustic wave transfers part of its momentum to the medium. An object in the path of the sound wave can absorb and scatter part of the wave's energy. The instantaneous net force acting on the object can be understood as the integral of excess of pressure (p), due to the acoustic radiation field, over the instantaneous time-varying object's surface (S'). For a plane wave propagating through a inviscid, lossless fluid, the component of the force in the ultrasonic beam direction can be written as:

$$F = \oint p\mathtt{n}dS'. \tag{5.10}$$

The acoustic radiation force caused by the amplitude modulated ultrasonic beam has a static (F_s) and a dynamic ($F_{\Delta\omega}$) components [101]

$$F = F_s + F_{\Delta\omega}. \tag{5.11}$$

For ultrasonic beams striking, e.g., a spherical target, the force is obtained integrating the pressure over the surface of the sphere.

The magnitude of this force F can be described as the product of a drag coefficient ($\mathtt{d}_r$), the time-average energy density $\langle E \rangle$ of the incident wave and the projected area of the object (S)

$$F = \mathtt{d}_r S \langle E \rangle . \tag{5.12}$$

The quantity $\mathtt{d}_r$ represents the scattering and absorbing properties of the object and has two components: one in the beam direction and the other transverse to it. It can be understood as the ratio of the force magnitude on the object, to the magnitude of the force when the object totally absorbs the sound wave, in this case $\mathtt{d}_r = 1$. For a more detailed explanation of this term and its expression, the reader is referred to Refs. [102, 92].

The ultrasonic pressure field of an amplitude modulated beam can be written as

$$p(t) = P_0 \cos(\Delta\omega t/2)\cos(\omega_0 t) \tag{5.13}$$

where P_0 is the pressure amplitude and $\Delta\omega/2$ is the modulating frequency. The energy density function for a traveling wave is [103]

$$E = p(t)/\rho c^2. \tag{5.14}$$

Considering the modulated frequency in the focus region $\Delta\omega/2 << \omega_0$, the energy density of the ultrasonic beam has a slow variation in time. The average value of an arbitrary oscillatory

function ξ is $\langle\xi\rangle_T = 1/(T_1 - T_2)\int_{T_2}^{T_1}\xi(t)dt$. The short-term time average of $p^2(t)$, on the assumption that the interval of integration $2\pi/\omega_0 << (T_1 - T_2) << 4\pi/\Delta\omega$ is longer than the ultrasound wave period but shorter than the modulation period, is

$$\left\langle p^2(t)\right\rangle_T = \frac{1}{(T_1 - T_2)}\int_{T_2}^{T_1} P_0\cos(\Delta\omega t/2)\cos(\omega_0 t) = \frac{P_0^2}{4}(1+\cos(\Delta\omega t)). \tag{5.15}$$

Using eqs. (5.12), (5.14) and the time-varying component of eq. (5.15), we obtain an expression for the time-varying force on the target

$$F_{\Delta\omega} = \frac{P_0^2 \mathrm{d}_r S}{4\rho c^2}\cos(\Delta\omega t). \tag{5.16}$$

Equation (5.16) states that the time varying force amplitude is proportional to the square of the incident ultrasound pressure.

The acoustic radiation pressure field from a single element focused transducer and the total pressure field of a two-elements annular array focused transducer were presented in chapter 4. Consider that the elements of this transducer are simultaneously excited by separate unmodulated CW sinusoidal signals with frequencies $\omega_1 = \omega_0 + \Delta\omega/2$ and $\omega_2 = \omega_0 - \Delta\omega/2$. An amplitude modulated field is obtained in the region where the beams interact. From eq. (4.3) (chapter 4) the short-time average of $p^2(t)$, in this case, is

$$\left\langle p^2(t)\right\rangle_T = \frac{P_1^2 + P_2^2}{2} + P_1 P_2\cos(\Delta\omega t + \psi_2 - \psi_1) \tag{5.17}$$

where P_1 and P_2 are defined in chapter 4 (eqs (4.4) and (4.5)).

Defining a unit point target at the center (x_0, y_0) of the focal plane, the drag coefficient with drag distribution has

$$\mathrm{d}_r = \delta(x - x_0, y - y_0), \tag{5.18}$$

such that $\mathrm{d}_r(x,y)dxdy = 1$ at (x_0, y_0) and zero elsewhere. Considering the object surface $S = dxdy$, substituting $\mathrm{d}_r(x,y)dxdy$ in eq. (5.12) and using the expressions for the pressure distribution for the two-elements confocal transducer (eqs (4.4) and (4.5)), the dynamic-force per unit of area on a point target can be given:

$$\begin{aligned} F_{\Delta\omega}(x,y) &= \frac{1}{\rho_0 c^2} P_1(x,y)P_2(x,y)\cos(\Delta\omega t + \psi_2 - \psi_1) \\ &= \frac{\rho_0 u_0 \pi^2 a_1^2}{\lambda_1\lambda_2 R^2} jinc\left(\frac{r a_1}{\lambda_1 R}\right)\left[a_{2e}^2 jinc\left(\frac{r a_{2e}}{\lambda_2 R}\right) - a_{2i}^2 jinc\left(\frac{r a_{2i}}{\lambda_2 R}\right)\right]. \end{aligned} \tag{5.19}$$

5.2.3 System point spread function

The output of a point object is known as the point spread function (PSF) of the imaging system, and usually determines the blurring of the obtained image. The image obtained from any imaging system can be described as the spacial convolution of the true object ($f_{Obj}(x,y)$) with the PSF ($h_{PSF}(x,y)$) plus noise

$$g_{Im}(x,y) = f_{Obj}(x,y) \otimes h_{PSF}(x,y) + noise. \tag{5.20}$$

Experimentally or theoretically determining this function is useful to restore the image, reducing the intrinsic degradation caused by the imaging system.

In our experiments, the brightness of each pixel is proportional to the amplitude of the vibration caused by the dynamic radiation force, which is proportional to the magnitude of the dynamic component of the force.

The PSF, for the system under investigation, is defined as the acoustic radiation force distribution in the focal plane, normalized by the force amplitude at the focal point

$$h_{PSF}(x,y) = \frac{F_d(x,y)}{F_d(x_0,y_0)} = (a_{2e}^2 - a_{2i}^2)^{-1} jinc\left(\frac{ra_1}{\lambda_1 R}\right)\left[a_{2e}^2 jinc\left(\frac{ra_{2e}}{\lambda_2 R}\right) - a_{2i}^2 jinc\left(\frac{ra_{2i}}{\lambda_2 R}\right)\right]. \tag{5.21}$$

It is worthwhile to reinforce that the eq. (5.21) is valid for the plane at the focal depth and parallel to the transducer surface. The PSF's for planes parallel to it are depth dependent. An expression for the PSF, of the x-z plane, can be obtained using the same procedure presented here and the proper expressions for the pressure fields.

5.2.4 Experiment

The confocal transducer, with central frequency of 3 MHz and focal depth of 70 mm, and the Doppler transducer, with central frequency of 2.5 MHz, were fixed to a three axes motorized system placed over an acrylic tank filled with degassed water. Moreover, they were arranged so that their beams could come across in the focal point of the confocal transducer. Both elements, which compose the confocal transducer, were driven, with slightly different frequencies, by an arbitrary waveform generator (Tektronix, AFG320) and a homemade 20 dB RF amplifier. The dynamic acoustic radiation force vibrates the region where the two focused beams interact at frequency $\Delta\omega$ and the Doppler transducer measures this vibration. The Doppler signal amplitude output was recorded through a lock-in amplifier (EG&G Instruments, model 7220). The lock-in reference was the low frequency component (difference between both frequencies) of

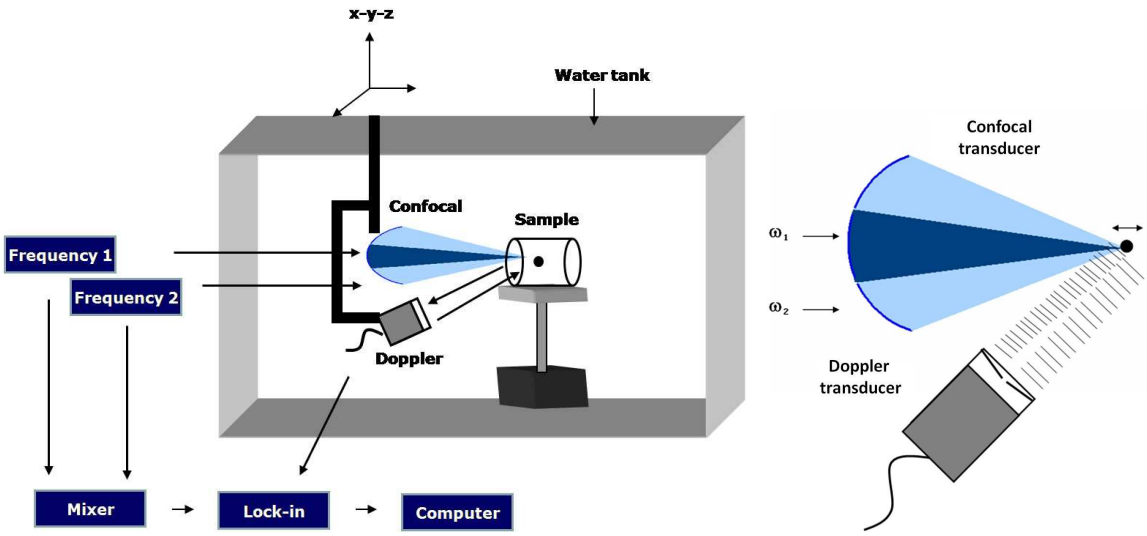

(a) (b)

Figure 5.2: Depiction of the experimental setup showing the excitation and detection components.

the AM signal. The data acquisition and the motorized system control were achieved through a custom software in LabView (National Instruments). Figure 5.2 depicts the experimental setup.

To evaluate the resolution of the method, a stainless steel spherical target with diameter of 0.66 mm was used as a point-target. This sphere was attached to a thin latex membrane. To generate the image of this target, the confocal and Doppler transducers were simultaneously scanned across the focal plane of the confocal transducer with increment step of 0.05 mm. The frequency of modulation of the ultrasonic field was Δf =600 Hz. The Doppler output was recorded at each step point of the scan. The profile result was then compared to the theoretical PSF developed in section 5.2.3.

5.2.5 Phantom experiment

This experiment was designed to verify the image obtained of a sphere immersed in a phantom with viscoelastic properties similar to the human tissue, with the diameter (2.6 mm) larger than the system resolution. The phantom is made of paraffin gel and has cylindrical geometry, with height of 123 mm and diameter of 82 mm. To acquire the data to form the image, the same experimental setup described before, as depicted in figure 5.2, was used. A photograph of the experimental setup is shown in figure 5.3. The increment step, of the scanning movement, was 0.0625 mm and the frequency of modulation was, again, Δf = 600Hz.

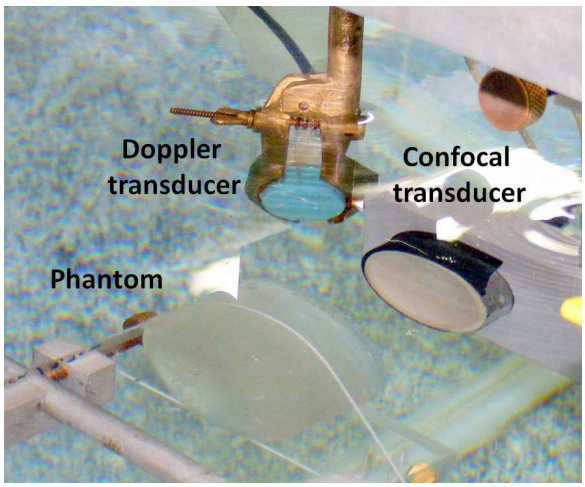

Figure 5.3: Photograph of the experimental setup used to obtain the image of a 2.6 mm diameter sphere, larger than the system resolution, immersed in the paraffin gel phantom.

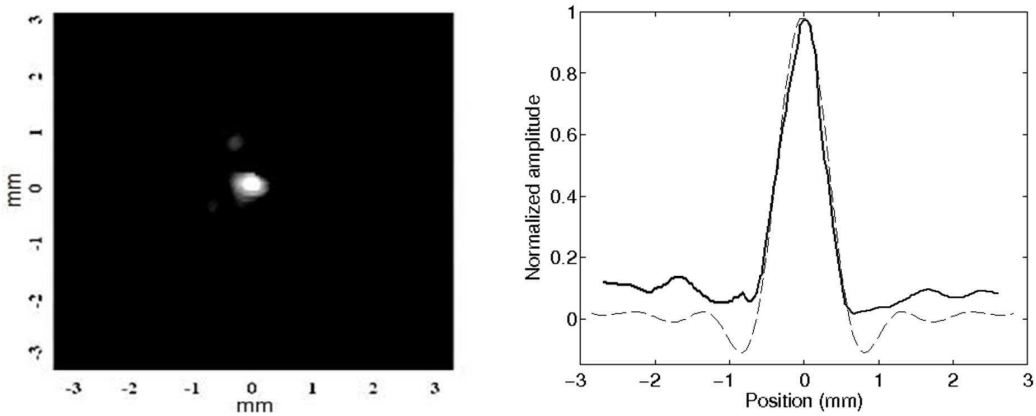

(a) (b)

Figure 5.4: (a) Normalized vibration amplitude image of the 0.66 mm diameter stain steel sphere, detected with the Doppler transducer. (b) Experimental profile (solid line) and the theoretical PFS profile (dashed line) given by eq (5.21).

5.3 Results and discussion

5.3.1 System resolution

Figure 5.4(a) shows the image representing the normalized vibration amplitude distribution, detected with the Doppler transducer, of the sphere attached to the latex sheet. The profile of this image (solid line) and the profile of the theoretical PSF (dashed line), given by eq. (5.21), are shown in figure 5.4(b)

The main lobe of the experimental and simulated profiles had good agreement. The full width at half maximum (FWHM) of the theoretical main lobe was approximately 0.7 mm [92] and matched with experiment; however, measured and theoretical sidelobes differed. There

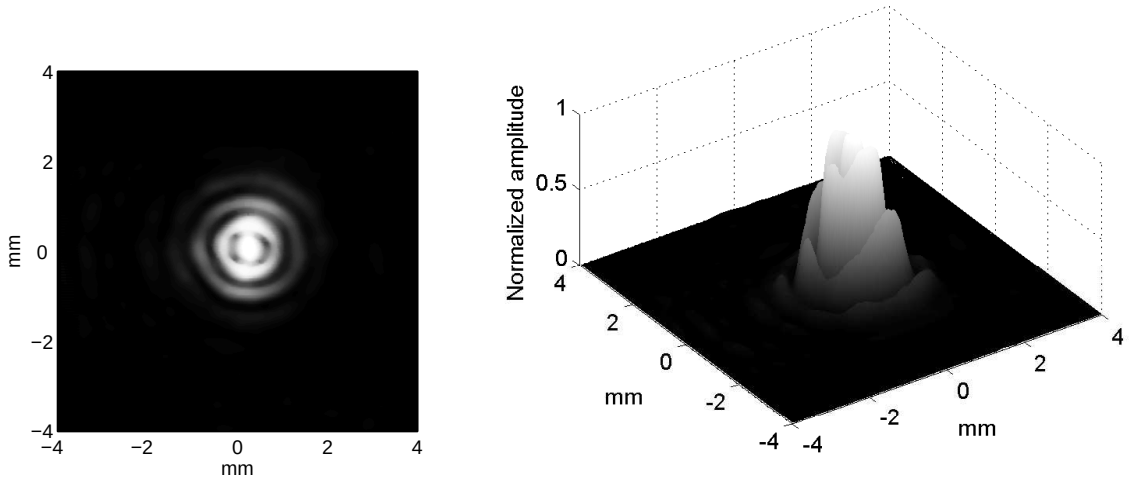

(a) (b)

Figure 5.5: (a) Vibration amplitude image of a 2.6 mm diameter stain steel sphere, obtained scanning the excitation confocal transducer and the Doppler transducer simultaneously. The vibration frequency of the AM acoustic field was $\Delta f = 600$ Hz. (b) Surface levels of the same image.

are few explanations for the observed difference: i) reverberation, from the water tank walls, of the low-frequency component of the continuous ultrasound wave transmitted by excitation transducer; ii) effects of the water nonlinearity in the acoustic wave propagation; iii) vibrations of the latex sheet induced by the dynamic acoustic radiation force; iv) the Doppler measurement was not taken into account to the development of the theoretical PSF. The Doppler transducer moved with the confocal transducer during the sample scanning. Therefore, the acoustic field, transmitted by the Doppler transducer, reaching the sphere was not constant over time, what interferes in the relative output amplitude consequently, affecting the final image.

5.3.2 Phantom experiment

The normalized vibration amplitude image of the sphere immersed in the paraffin gel phantom is shown in figure 5.5(a). This image shows a good contrast; however, circular rings artifacts can be observed. These artifacts appear due to the negative sidelobes of the PSF (see figure 5.4(b)), caused by the interaction of the beams transmitted by the confocal array transducer.

Numerical simulation

A 2D digital phantom with the same dimensions as the experimental image shown in figure 5.5(a) with a inclusion modeled as being infinitely long 2.6 mm diameter cylinder was

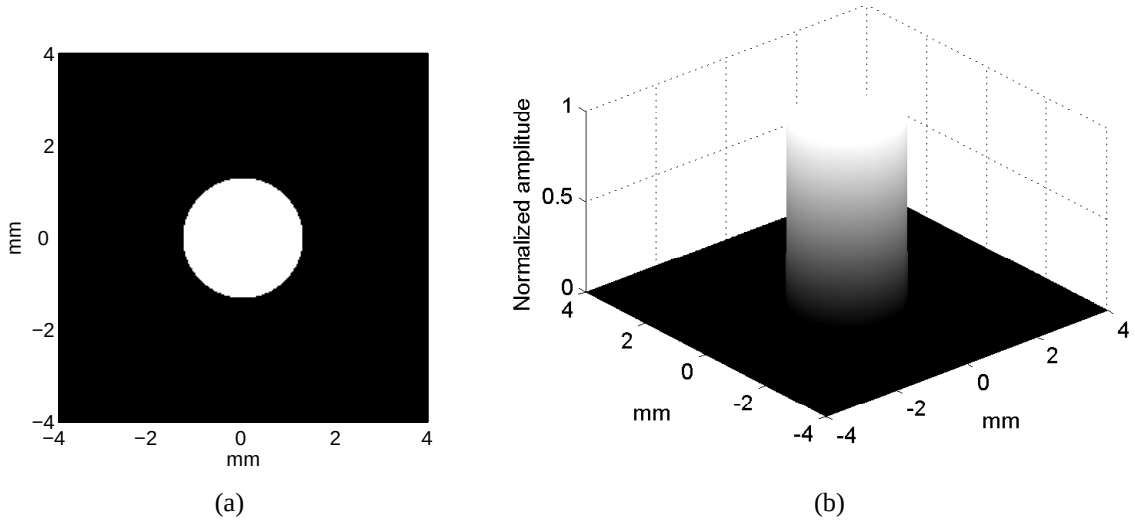

(a) (b)

Figure 5.6: (a) Simulated 2D phantom with a inclusion modeled as being infinitely long 2.6 mm diameter cylinder; (b) Surface levels of the simulated phantom.

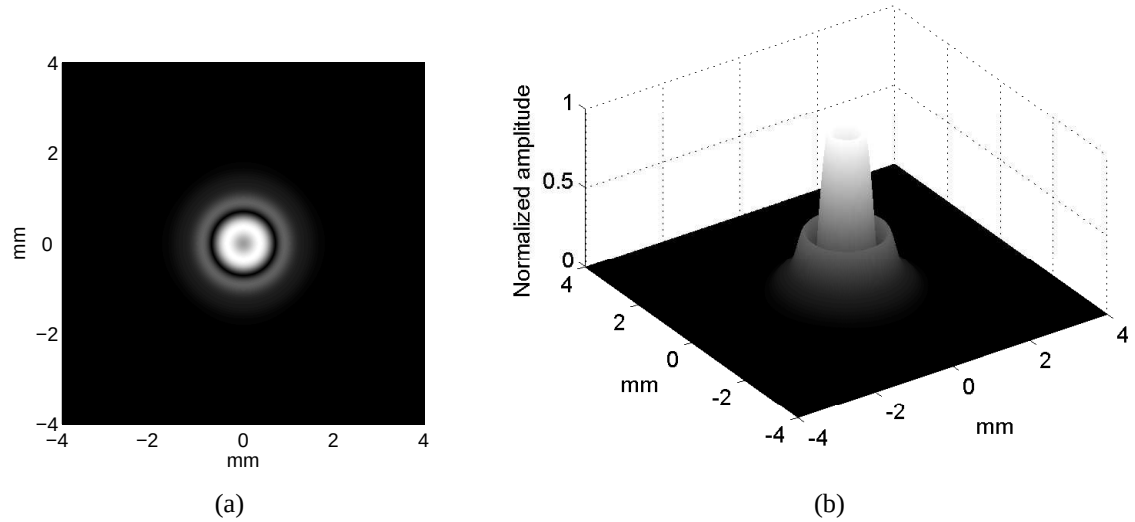

(a) (b)

Figure 5.7: (a) Simulated image obtained by the convolution of the simulated phantom with the PSF of the system. The vibration frequency of the AM acoustic field used to simulate the PSF was $\Delta f = 600$ Hz; (b) Surface levels of the same image.

simulated (see figure 5.5). Figure 5.7 shows the magnitude image of the convolution between the theoretical PSF with the simulated phantom, as described in eq. (5.20).

The overall features of the simulated image are comparable to the experimental image. Small differences in the peak morphology at the center of the images can be observed. Simulating a 3D phantom and taking into account the Doppler transducer to model the PSF of the system can improve the agreement between simulated and experimental images.

5.4 Summary

In this chapter, we evaluated the ability of the CW Doppler to detect small vibrations induced by dynamic acoustic radiation force. The experiments demonstrated that the single channel CW Doppler ultrasound system is an alternative to detect the oscillatory movement induced by the focused confocal beams. The system was capable to detect the micro-vibrations induced to steel spheres (either attached to a latex sheet or embedded in a gel phantom) by a modulated acoustic radiation force. The used Doppler system is a non-expensive ultrasound, has fast response, what easily allows building an image of the scanned sample. The drawback of this system is the non absolute output values for the amplitude of vibration and poor depth resolution to detect movements of the scatterers.

The next steps of this research are: development of a theoretical PSF taking into account both Doppler and confocal beams, also implement a pulsed tone burst excitation and verify the ability of the system for building images of biological tissues.

6 Tracking acoustic radiation force-induced small displacements using a magnetic sensor

6.1 Introduction

Acoustic radiation forces arise when a medium absorbs or scatters sound waves. In this interaction, part of the wave momentum is transferred to the attenuating medium [104]. If the wave intensity does not change with time, the radiation force is defined as steady force, whereas a dynamic force appears if this intensity is amplitude modulated with time.

For a description of how to calculate the acoustic force exerted by a amplitude-modulated continuous wave (CW) on a sphere, the reader is referred to Ref. [101, 49]. This force is a combination of dynamic and static forces, with similar magnitudes for low modulation frequencies (up to a few kilohertz) [101]. This prediction was experimentally observed by tracking the dynamic and static movement of spheres suspended in a pendulum configuration [105]. The vibration was estimated using a laser vibrometer, and the static deflection was obtained using an alignment laser positioned on a micro-station. For higher frequencies, the magnitude of the dynamic force increases due to parametric amplification [49].

The use of acoustic radiation force as a piston to promote the motion of viscoelastic media has resulted in different techniques for probing the material viscoelastic parameters. Special interest has been given to medical elasticity imaging modalities [106]. Pulsed steady force has been used in such widespread techniques as acoustic radiation force impulsive imaging (ARFI) [38] and supersonic imaging [43]. The interaction of two ultrasonic beams with slightly different frequencies produces a dynamic acoustic force, which has been used in vibro-acoustography to map the mechanical properties of the investigated region [92].

Acoustic radiation force-induced movement of spheres has been used to calculate the mechanical properties of viscoelastic materials. Aglyamov et al. [107] developed a theory to

evaluate the movement of solid spheres, embedded in viscoelastic media, in response to short-pulse-duration acoustic radiation forces. Their simulations agree well with experimental results. The time required for the sphere to reach the maximum displacement value was verified to be proportional to the material stiffness [107, 108]. Orescanin et al. [109] fitted the relaxation movement of a rigid sphere displacement induced by ultrasonic pulsed radiation force to a harmonic damped-motion model. They obtained both the shear modulus and the viscosity from the model. In the papers [107, 108, 109] in which pulsed radiation force was used to excite the sphere, the movement was tracked by ultrasonic techniques. A dynamic-frequency (up to 5 kHz) radiation force was applied to rigid spheres embedded in water and tissue-like phantoms [110]. In this work, the authors inferred the medium's viscoelastic properties from the plots of movement velocity versus vibration frequency. The adopted model is based on the theory for mechanical impedance developed by Oestreicher [48] for the oscillations of a rigid sphere in incompressible viscous fluid and viscoelastic media. In this case, the vibration velocity of the sphere was tracked using a laser vibrometer.

Carneiro et al. [47] proposed the magnetic tracking of the displacement of a magnetic target induced by dynamic acoustic radiation force between 0 and 0.5 MHz [49]. Based on Oestreicher's theory [48], they simulated a magnetic-sensor response due to the vibration of a spherical magnet embedded in water and in a viscoelastic medium. Based on the use of acoustic radiation force to move a magnetized object and the measurement of its position using a magnetic sensor, we developed a device to monitor acoustic pressure and force [50]. A cubic magnet was attached to a thin latex sheet, which was connected to a magnetoresistive sensor. The pressure transducer was calibrated based on the output of a needle hydrophone.

The main goal of this chapter is to investigate the dynamic behavior of a rigid magnetic sphere caused by acoustic radiation forces. The sphere was suspended in water in a simple pendulum configuration. The drag force acting on the pendulum during its motion was considered to follow a modified Stokes law for a low Reynolds number, accounting for the phenomena related to its oscillatory movement. Steady forces of long (few seconds) and short (few milliseconds) duration were used. The movement of the magnetic sphere was tracked using a magnetoresistive sensor. From the new equilibrium position of the sphere in response to the long-duration static radiation force, the amplitude of this force was estimated [111, 105]. To access the water viscosity, the relaxation movement after the termination of the acoustic force was fitted to a harmonic-motion model. Based on the results for the acoustic force and water viscosity, the theoretical profile of the sphere micro-order displacement as a function of time due to short-duration acoustic radiation force agreed well with experimental results.

The advantages and disadvantages of using a magnetic sensor to monitor the movement of

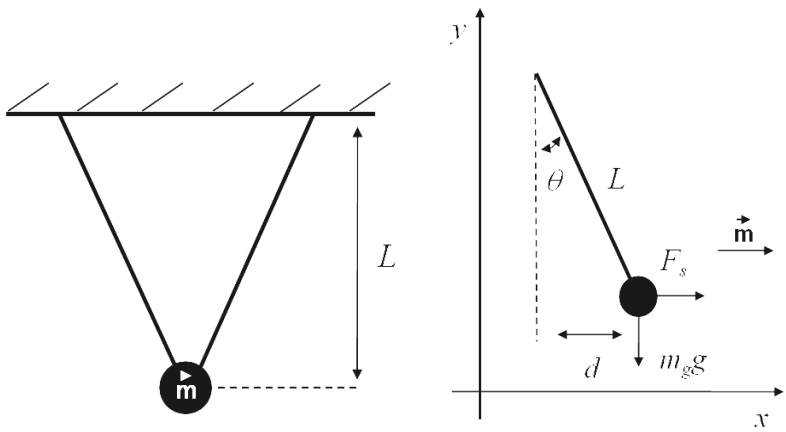

(a) (b)

Figure 6.1: (a) Magnetic sphere suspended in a bifilar arrangement. (b) Pendulum deflected from its original equilibrium position.

the magnetic sphere in our experiments are discussed in the text.

6.2 Materials and methods

A spherical rare earth permanent magnet (radius $a = 1.50$ mm) with density $\rho_s = 7498$ kg/m^3 was suspended with a human hair strand as shown in figure 6.1(a). Figure 6.1(b) shows the configuration of the pendulum deflected from its rest position. The pendulum height used in the experiments was $L = 60$ mm. The absolute magnetic field produced by the sphere was measured with a fluxgate magnetometer (model 428C, Applied Physics Systems Inc, Mountain View, CA).

An experimental setup was built to verify the static and dynamic displacements of a magnetic target mechanically excited by acoustic radiation force. These displacements were induced by both continuous ultrasonic waves and tone-burst pushing beams (10000 - 50000 cycles) generated by a focused single-element transducer with a central frequency of 3 MHz and a focus distance of 70 mm. The transducer was driven by sinusoidal burst signals generated with an arbitrary-function generator (model 33220A, Agilent Technologies, Palo Alto, CA) amplified by a homemade 20 dB RF amplifier. The motion was tracked using a magnetoresistive sensor (HMC 1001, Honeywell) placed approximately 10 mm away from the sphere and axially aligned with the magnetic moment of the magnet (see figure 6.2). In this configuration, the magnetic field variation for the magnetic sensor should be considered to be linearly proportional to the induced displacement of the sphere. This assumption is valid because the radiation force-induced motion of the sphere is much smaller than the distance between the magnetic

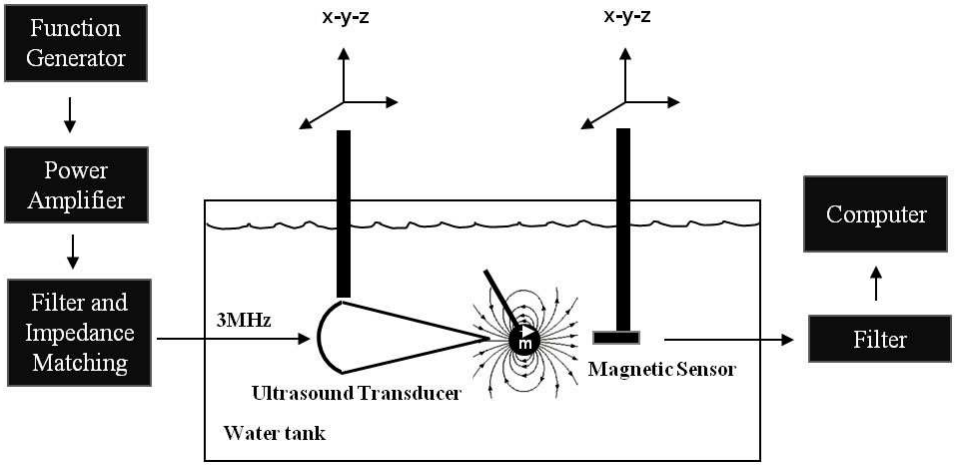

Figure 6.2: Depiction of the experimental setup. An acoustic radiation force deflected the magnetic spherical bob, and the resulting movement was tracked using a magnetic sensor positioned opposite to the ultrasonic transducer. The maximum sensitivity of the sensor was aligned with the axis of the magnetic moment of the magnet.

target and the point of measurement [47]. The maximum induced displacement of the sphere was on the order of 1 mm. Figure 6.2 shows a schematic drawing of the experimental setup.

The pushing transducer and magnetic sensor were mounted to *micro*-positioning stages (resolution of 12.5 μm) so that the sphere could be positioned in the focus of the ultrasonic field and the magnetic sensor could be calibrated (displacement vs. output voltage). For small displacements, the voltage output was linearly proportional to the displacement. The magnetoresistive sensor output was filtered and amplified (Model SR 650, Stanford Research Systems, Inc, Sunnyvale, CA) and acquired through an oscilloscope board PCI-5112 (National Instruments). The experiments were carried out in a tank containing degassed water with dimensions of 160 x 80 x 80 cm.

6.2.1 Pendulum driven by a static force

The acoustic radiation force acting on the sphere while the ultrasonic transducer is on can be calculated by finding the new equilibrium displacement generated by the radiation force, as presented elsewhere [111, 105]. In this case, the equilibrium can be represented by the balance between the static radiation force and the gravitational force. The mass of the sphere must be corrected for buoyancy. The static acoustic radiation force, not accounting for the mass of the thread, can be written as

$$F_s = \frac{4}{3}\pi a^3(\rho_s - \rho_w)g\frac{d}{\sqrt{L^2 - d^2}} \tag{6.1}$$

where a is the radius of the sphere, L is the suspension length, d is the horizontal component of the sphere displacement, g is the acceleration due to gravity, and ρ_w and ρ_s are the densities of the water and the sphere, respectively.

6.2.2 Pendulum driven by an impulsive force

The differential equation for the movement of a simple pendulum composed of a particle of mass m_s attached to the end of a light, inextensible rod (here, we consider the hair strand as a massless rod) immersed in a viscous medium can be given as

$$\frac{d^2\theta}{dt^2} + 2\alpha\frac{d\theta}{dt} + \omega^2 \sin\theta = F(t) \tag{6.2}$$

where $\alpha = b/2m_i$, b is the damping constant given by the friction between the bob and the viscous medium, $\omega = \sqrt{(m_g g)/(m_i L)}$ is the angular frequency assuming no damping, and $F(t)$ is the acoustic radiation force acting on the sphere. Accounting for buoyancy, the apparent weight of the object is reduced by the weight of the displaced fluid (here, water) $m_w = \frac{4}{3}\pi a^3 \rho_w$. Therefore, the gravitational mass is

$$m_g = m_s - m_w \tag{6.3}$$

and the inertial mass of the pendulum m_i is given by

$$m_i = m_s + K m_w \tag{6.4}$$

where Km_w is the added mass for the water, and K is a constant factor that depends on the bob shape, fluid viscosity and the density and boundary conditions of the oscillatory movement. An expression for K is shown in Section 6.2.3. Because all of the experiments described in this chapter have small oscillatory angles, the approximation $\sin\theta \approx \theta$ is adopted. For a full description of the parameters affecting the movement of a simple pendulum, the reader is referred to Ref. [112].

Considering the pendulum at rest in the equilibrium position and the application of an impulsive external force with a magnitude F_s of a short duration t' compared to the underdamped oscillation period, the initial sphere velocity in the x direction is

$$v_0^x = \frac{F_s t'}{m_i} \tag{6.5}$$

and the solution for the pendulum considering small oscillation angles can be expressed as

$$d(t) = \frac{v_0^x}{\omega_d} e^{-\alpha t} \sin(\omega_d t) \tag{6.6}$$

where $d(t)$ is the position of the sphere in the x direction according to figure 6.1(b) and $\omega_d = \sqrt{\omega^2 - \alpha^2}$ is the oscillation frequency for the damped pendulum.

Considering a series of short impulses of duration t', eq. (6.6) results in a Green's integral

$$d(t) = \frac{1}{m_i} \int_0^t \frac{e^{-\alpha(t-t')} \sin(\omega_d (t-t'))}{\omega_d} F(t) dt'. \tag{6.7}$$

Equation (6.7) represents the solution of a unidimensional forced underdamped harmonic motion. This solution is valid when the initial oscillator position ($d(0)$) and velocity ($\dot{d}(0)$), before any force is applied, are equal to zero.

The acoustic radiation force acting in the x direction (figure 6.1(b)), which is considered to be impulsive, is given by

$$F(t) = \begin{cases} F_s, & 0 \leq t \leq t_0 \\ 0, & t > t_0 \end{cases} \tag{6.8}$$

where t_0 is the radiation pulse duration and F_s is the magnitude of the force.

For $0 \leq t \leq t_0$, eq. (6.9) represents the integral over eq. (6.7) (the solution of eq. (6.2) when the ultrasonic radiation force is on ($F(t) \neq 0$)). For $t > t_0$, eq. (6.9) is the solution of eq. (6.2) when the ultrasonic radiation force is off ($F(t) = 0$)

$$d(t) = \begin{cases} \frac{F_s}{m_i(\alpha^2+\omega_d^2)} \left[1 - e^{-\alpha t} \left(\cos \omega_d t + \frac{\alpha}{\omega_d} \sin \omega_d t\right)\right], & 0 \leq t \leq t_0 \\ e^{-\alpha(t-t_0)} \left\{ d(t_0) \cos[\omega_d (t-t_0)] + \frac{d(t_0)\alpha + v^x(t_0)}{\omega_d} \sin[\omega_d (t-t_0)] \right\}, & t > t_0 \end{cases} \tag{6.9}$$

here, $v^x(t_0)$ and $d(t_0)$ are the sphere velocity and position, respectively, when the ultrasonic transducer is turned off. When the pulse length (t_0) is long enough that the pendulum adopts a new equilibrium ($v^x(t_0) = 0$), eq. (6.9) for $t > t_0$ can be reduced to

$$d(t) = A e^{-\alpha(t-t_0)} cos[\omega_d (t-t_0) + \varphi] \tag{6.10}$$

where $\varphi = \arctan(-\alpha/\omega_d)$ and $A = d(t_0)/\cos\varphi$.

6.2.3 Viscosity of fluids

For low Reynolds numbers,

$$Re = \frac{2a\rho_w V}{\eta} \tag{6.11}$$

the viscous drag force is considered to be linearly proportional to the velocity. In eq. (6.11), $V = \omega_d A$ is the characteristic velocity, A is the oscillation amplitude, and η is the viscosity of an incompressible fluid. In the case of a oscillatory sphere in an incompressible fluid for small oscillation amplitudes compared to $2a$, this force can be written as (see, e.g., Ref.[113] p. 83 to 92)

$$F_d = -\left[6\pi a\eta\left(1+\frac{a}{\delta}\right)v + 3\pi a^2\left(1+\frac{2a}{9\delta}\right)\rho_w\delta\frac{dv}{dt}\right]. \tag{6.12}$$

From the first term proportional to the velocity in eq. (6.12), the relation for α of eq. (6.2) becomes

$$\alpha = \frac{6\pi a\eta\left(1+\frac{a}{\delta}\right)}{2m_i} \tag{6.13}$$

where $\delta = \sqrt{2\eta/\rho_w\omega_d}$ is the penetration depth and is used to determine the thickness of the boundary layer around the spherical bob. The second term proportional to the acceleration represents the added mass (eq. (6.4)), which can be written as

$$\begin{aligned} Km_w &= 3\pi a^2\left(1+\frac{2a}{9\delta}\right)\rho_w\delta \\ K &= \frac{9}{4}\frac{\delta}{a}+\frac{1}{2} \end{aligned} \tag{6.14}$$

There are reports [114, 115] evaluating the water viscosity by measuring the amplitude of the oscillation decay of oscillating spheres. Empirical factors were included in the drag force equation, as shown in eq. (6.15), to correct for the overestimation of the water viscosity

$$F_d = -\left[\frac{6\pi a\eta}{f_1}\left(1+\frac{a}{\delta}\right)v + f_2 3\pi a^2\left(1+\frac{2a}{9\delta}\right)\rho_w\delta\frac{dv}{dt}\right]. \tag{6.15}$$

The values f_1 and f_2 are used to correct for the dissipative and the inertial forces, respectively.

For the results presented here, only the linear drag force was used because the Reynolds numbers were on the order of $Re < 40$ units in these experiments.

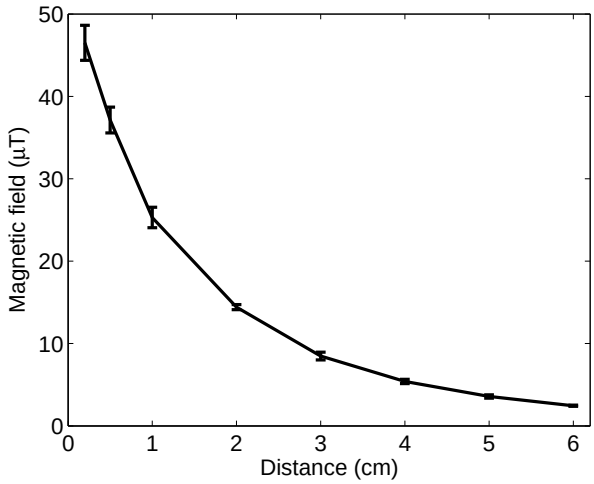

Figure 6.3: Magnetic-field profile for different distances from the magnetic sphere.

6.3 Results

The magnetic-field profile for different distances from the magnetic sphere is shown in figure 6.3.

Figure 6.4 shows the output of the magnetic transducer representing the displacement of the sphere in response to a pulsed force acting on the magnetic sphere. The pulse duration was long enough that the acoustic radiation force balanced the gravitational and buoyancy forces. Immediately after the ultrasonic waves reaches the pendulum, the sphere moves from its original position to its maximum displacement value and then undergoes an oscillatory movement (Region 1 in figure 6.4) until rest. The new equilibrium position (Region 2) was used to calculate the static radiation force $Fs = 2.36$ μN according to eq. (6.1). Region 3 represents the period after turning the ultrasonic transducer off and was used to estimate the water viscosity (η) according to eq. (6.10)(see figure 6.5(a)).

Figure 6.5 shows graphs corresponding to Region 3 of figure 6.4, where the pendulum motion is free of the ultrasonic force ($t > t_0$). The time representing 0 ms in the plots of figure 6.5 represents t_0 in figure 6.4. Acoustic radiation forces with two different magnitudes, $Fs = 2.36$ μN and $Fs = 12.3$ μN, and respective voltages applied to the piezoeletric ceramic of 3 V and 6 V displaced the target to two different equilibrium positions of $d(t_0) = 159$ μm (figure 6.5(a)) (Reynolds number of $Re = 11$ for the first half-period) and $d(t_0) = 586$ μm (figure 6.5(b)) ($Re = 40$), respectively. In both cases, t_0 was long enough for the sphere to reach a new equilibrium position. These curves were used to obtain viscosity values according to eqs. (6.10) and (6.13). The viscosities were $\eta = 0.0030$ Pa s (figure 6.5(a)) and $\eta = 0.0038$ Pa s (figure 6.5(b)).

Short acoustic radiation force ($Fs = 12.3$ μN) pulses with 10000 cycles ($t_0 = 3.3$ ms),

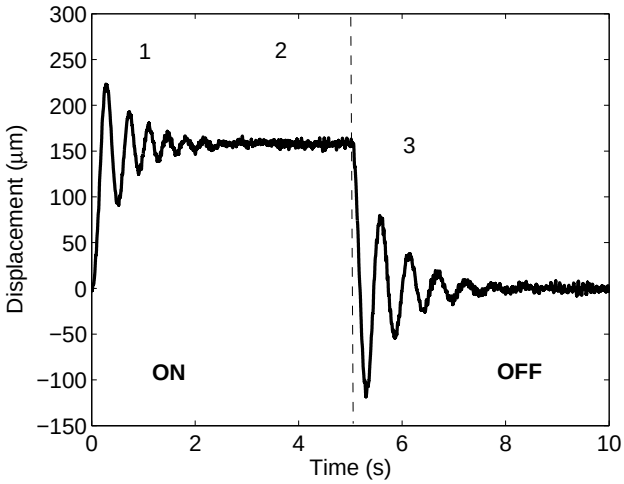

Figure 6.4: Experimental induced displacement of a sphere tracked through the magnetoresistive sensor. In this graph, Region 1 represents the period during which the sphere oscillates around the region in which the acoustic radiation and buoyancy forces balance with the gravity force. Region 2 represents this new equilibrium position and was used to estimate the acoustic radiation force magnitude. The static acoustic force was $Fs = 2.36$ μN. Region 3 ($t > t_0$) represents the oscillation around the original pendulum equilibrium position after turning the ultrasonic transducer off.

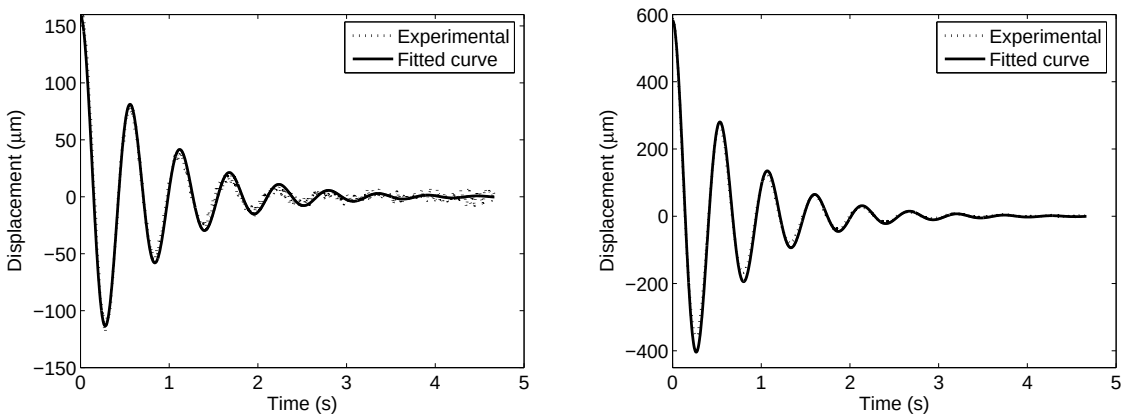

(a) (b)

Figure 6.5: Experimental tracked movement and curves fitted to eq. (6.10) corresponding to Region 3 in figure 6.4 when the ultrasonic transducer was off ($t > t_0$). The time representing 0 ms in the plots represents t_0 in figure 6.4. Acoustic radiation force with two different magnitudes, $Fs = 2.36$ μN and $Fs = 12.3$ μN displaced the target to two different equilibrium positions of (a) $d(t_0) = 159$ μm and (b) $d(t_0) = 586$ μm, respectively. The respective viscosities were (a) $\eta = 0.003$ Pa s and (b) $\eta = 0.0038$ Pa s.

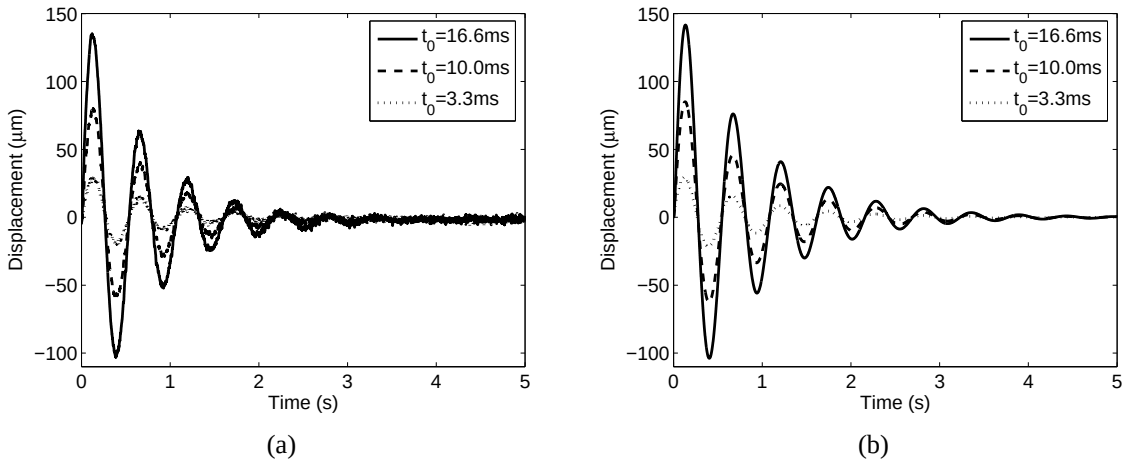

Figure 6.6: Pendulum movement due to short-duration pulsed force $Fs = 12.3\ \mu$N with different durations. (a) Experimental results; (b) simulated curves obtained from eq. (6.9).

30000 cycles ($t_0 = 10.0$ ms) and 50000 cycles ($t_0 = 16.6$ ms) of 3 MHz sound waves moved the pendulum. Figure 6.6(a) shows the experimental curves obtained for the pendulum movement, and figure 6.6(b) shows the simulated curves obtained through eq. (6.9) under the assumption of the same experimental boundary conditions.

The averaged viscosity found from six measurements, varying the Reynolds number between $3.5 < Re < 40$, was $\eta = 0.0030 \pm 0.0005$ Pa s, which was the value adopted to simulate the displacement profile of figure 6.6(b). The empirical parameter to correct for the drag force in eq. (6.15) was $f_1 = 0.50 \pm 0.05$. The adopted reference water viscosity was $\eta = 0.001$ Pa s [116], and the eq. parameter to correct for ω was very close to unity $f_2 = 1$.

6.4 Discussion

Interest in studying the acoustic radiation force is increasing, especially because of the increasing number of medical applications. The methodology presented here is an efficient alternative for studying static and dynamic ultrasonic radiation forces.

Figure 6.4 shows that the magnetic-transducer output is capable of displaying the dynamic and static displacements of a sphere versus time. Laser Doppler vibrometry output, for example, is the representation of the velocity of the movement, meaning that the static and dynamic force can rarely be accessed at the same time. Chen et al. [105] used a pendulum similar to the pendulum presented here to measure the static and dynamic ultrasonic-radiation forces simultaneously. They used optical vibrometry to calculate the dynamic velocity, whereas the static deflection was estimated using a second laser mounted to a micro-stage. The static measure-

ment was limited by the resolution of the stage. Their setup measures both forces precisely; however, the alignment procedure is a limitation for the case of a sphere embedded in a viscoelastic medium, as they suggested. Additionally, optical measurements demand transparent media.

Another alternative is the measurement of the displacement through a second tracking ultrasonic transducer. This methodology is capable of measuring both static and dynamic displacements with a resolution of up to hundreds of nanometers [117, 118]; however, dynamic measurements are limited by the pulse repetition frequency of the tracking transducer [109]. Cross-talk between both transducers is another potential limitation, depending on the application [109].

Frequency range from dc to megahertz can be explored when a magnetic sensor is used to evaluate the dynamic response of the medium in response to the acoustic radiation force [47, 119]. These measurements implies that the medium under investigation is marked with a magnetized target or tracers. The sensitivity of the system depends on the magnetization of the target, the distance between the magnetic sensor and target, and the type of magnetic sensor used [119]. For a theoretical analysis of sensitivity limits to evaluate the dynamic displacement of a magnetized target excited by acoustic radiation force, we encourage the reader to consult [47].

The results of the sphere movement tracked with the magnetic sensor showed that displacements of few micrometers can be estimated with good signal-to-noise ratios. Sosa et al. [120] tracked vibrations (200 Hz to 4 kHz) of a small cubic magnet using a magnetoresistive sensor. The magnet was displaced through continuous excitation, and the vibration amplitude was detected using a lock-in amplifier with a resolution of 65 nm.

The good quality of the curve fits shown in figure 6.5 indicate that the experimental results were well represented by the harmonic-motion model; however, the resultant viscosity values were higher than the expected value for water ($\eta \approx 0.001$ Pa s) [116]. Several factors may have caused this difference. The water was not distilled, and the thin thread and the adhesive used to attach it to the sphere were not taken into account. The empirical parameter $f_1 = 0.50 \pm 0.05$ to correct for the dissipative force because of water viscosity is similar to values found elsewhere [114, 115]. In these works, the parameter f_1 was closer to 1 for more viscous fluids. The parameter to correct for resonance frequency was found to be very close to unity $f_2 = 1$, meaning that values for ω were close those expected.

For shorter pulse durations (figure 6.6), there was a good agreement between the experimental and theoretical results, indicating the good accuracy of the acoustic radiation force

magnitude found using the plot in figure 6.4. When the acoustic waves reached the sphere, it started to move and continued to move after the pushing beam had stopped until reaching a maximum displacement. The graphs show that the longer the pulse duration, the larger the maximum displacement. When the length of the pulse is sufficiently long to compensate the gravity force, the sphere reaches a point of equilibrium, as was already discussed. Aglyamov et al. [107] made similar observations for spheres embedded in viscoelastic media.

We experimentally evaluated one specific setup to show the viability of quantifying small displacements of a spherical target when displaced by ultrasonic radiation force. The method presented here can be used to investigate the viscosity of different fluids regardless of its opacity. Non-spherical objects can also be used as target to the acoustic radiation force, but the sensitivity of the method can vary depending on the object's shape. Although invasive, this technique may also be a potential tool for in vivo applications, such as evaluation of magnetic nanoparticle distribution in tissues and therapy control using implanted magnetic particles. For these applications the sensitivity of the method can be increased, for example in static displacement or low-frequency vibrations (hundred Hz or lower), using a sensitive magnetic sensor like the superconducting quantum interference device (SQUID) [119].

6.5 Summary

The movement of a simple pendulum, composed of a magnetic sphere and displaced by acoustic radiation force, was evaluated. The displacements were on the order of a micrometer and were tracked using a magnetoresistive sensor. The experimental displacement plots showed good signal-to-noise ratios for displacements of a few micrometers and agreed well with theoretical predictions. The pendulum moving free of external radiation forces, for low Reynolds numbers, presented an amplitude decay following the Stokes law. These curves were fit to a harmonic-oscillator model, and the viscosity for water was calculated. The overestimation found for the viscosity was corrected by an empirical factor f_1, which is similar to values reported in the literature. The results found for the resonant frequencies agree with the expected values.

7 Detection of acoustic radiation force-induced displacement using pulse-echo ultrasound

7.1 Introduction

A method to detect the movement induced by acoustic radiation force via pulse-echo ultrasound as a mean of characterizing biological tissues was first proposed by Sugimoto et al. [37]. They used a concave transducer driven with burst signals to generate focused acoustic radiation force, which displaced the material. The induced movement versus time was evaluated through a pulse-echo ultrasound probe positioned in the opposite side.

Several papers using acoustic remote force and pulse-echo detection to characterizing elastic behavior of materials were published since then. Sarvazyan et al. [40] suggested using this methodology to track the resulting shear waves propagating through the tissue. Estimating the velocity and attenuation of these shear waves are ways of estimating the medium elasticity [40, 41]. Based on this idea, Nightingale et al. [38] proposed the acoustic radiation force impulse (ARFI) technique, where the remote force is promoted through a short-duration acoustic radiation force using conventional scanner array and either the shear waves or local displacement are tracked within a region of interest using the same array transducer. Bercoff et al. [43] proposed the supersonic shear imaging, where the acoustic force is generated by an array transducer and the shear waves are measured using their ultrafast pulse repetition rate ultrasound scanner. Walker et al. [121] imaged viscoelastic parameters of heterogeneous phantoms by tracking the displacement at the excitation region of a focused ultrasonic transducer. Konofagou et al. [93] proposed the harmonic-motion imaging (HMI) where a focused transducer is driven with a modulated signal and sinusoidal motion is promoted in the region of excitation. This movement is tracked through a pulse-echo system. Orescanin et al. [109] and Karpiouk et al. [108] measured viscoelastic properties of phantoms, evaluating the transient displacement versus time of a spherical inhomogeneity placed in the focal region of excitation.

The displacements observed in acoustic radiation force-based imaging are typically small (less than 10 μm) [38], which is, approximately, two orders of magnitude smaller than other modalities, such as: conventional elastography or Doppler flow.

Simulations of micro-order (up to 8 μm) displacement measurement using ultrasonic echoes from a vibratory target are presented in this chapter. Effects of noise, amplitude and frequency of vibration were evaluated. The motion of a rigid sphere embedded in gelatin phantom, displaced by acoustic radiation was estimated using the ultrasonic echoes from a mono-channel pulse-echo system. From the motion of the sphere, the elastic shear modulus of the medium was estimated and compared with values obtained from DMA (dynamic mechanical analysis) method. A modified cross-correlation estimator was used in the simulations and experiments.

7.2 Materials and methods

7.2.1 Echo signal simulation

The echo signal from a random scatter at time $t = nT_s$ ($t = 1, 2, 3..$, T_s: sampling period) can be represented as a sinusoidal wave and Gaussian envelope $env(n)$

$$rf_m(n) = env(n) \cdot \sin(\omega_0 n T_s + \tau_m) + noise \tag{7.1}$$

where τ_m is the temporal delay and m is the echo number. Normally distributed noise signal was added to the simulated echo. The temporal delay of the echo signal returning from a vibrating scatter can be written as:

$$\tau_m = \frac{2U}{c} \sin(\omega_{osci} T_s m) \tag{7.2}$$

where U is the amplitude of vibration, ω_{osci} is the frequency of the oscillatory movement and T_s is ultrasound pulse repetition period.

7.2.2 Displacement estimation

The displacement was calculated using pairs of echoes by correlating the reference echo (rf_1) with the phase-shifted (rf_m; $m \geq 2$) echoes, through the cross correlation estimator:

$$CC(N) = \sum_{n=-K/2}^{n=K/2} rf_1(n) rf_m(n+N) \tag{7.3}$$

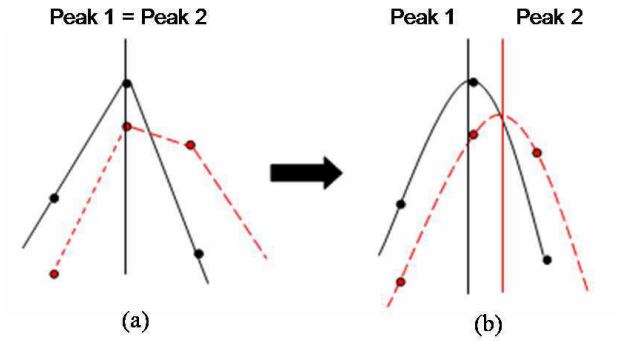

Figure 7.1: Diagram illustrating the maximum of the correlation function fitted to a parabola in order to calculate small displacements. (a) Correlation function before and (b) after the fitting.

where K is the size of the kernel window. The instantaneous scatter position estimated from the maximum value of the correlation signal output (calculated from eq. (7.3)) is

$$u = \frac{CC_{max} c}{2 f_s \cos\Theta} \tag{7.4}$$

where CC_{max} is the position where the correlation function presents its maximum value, c is the speed of sound, f_s is the sampling frequency and Θ is the angle between the ultrasound transducer and the moving object.

Commercial ultrasound scanners acquire the RF echo signals using sampling rates between 20 MHz and 60 MHz, which is not much higher than the ultrasonic wave frequencies used in clinical exams , i.e., the sampling rate would be less than 10 times greater than the wave frequency for a transducer operating at 10 MHz. For this reason, the maximum of the correlation function may not have the necessary resolution to estimate displacements of few micrometers (see figure 7.1). To resolve these smaller displacements, the RF data and the cross-correlation function can be up-sampled through interpolation techniques. In our simulations, the RF signal was sampled at 100 MHz, which is higher than the sampling rates usually employed in image ultrasound scanners; for this reason, only the cross-correlation output was up-sampled. The maximum of the discrete correlation function and its two neighbor points are fitted to a parabola, and its point of maximum is used in (7.4) to estimate the small displacements [122, 123] (see figure 7.1).

The pulse repetition frequency ($PRF = 1/T$) adopted in the simulations was of 10 kHz, the transducer central frequency of 5.0 MHz and a total of 100 (3 μs - each) echoes were used.

Vibration amplitude and phase estimation

After correlating the echoes, the resulting harmonic-motion profile is noisy. Applying a low-pass filter to this noisy vibration signal could underestimate the movement amplitude [94]. The Kalman filter showed to be an efficient method to detecting the vibration amplitude and phase from the noisy vibration profiles [94, 118]. In the present work, the amplitude and phase of the harmonic-motion were calculated using a two stage linear least squares fitting. This algorithm requires only the motion signal and movement frequency as input.

7.2.3 Statistical analysis

Bias (eq. (7.5)) and jitter (eq. (7.6)) were used to evaluate the performance of the modified cross-correlation algorithm to monitoring the amplitude of the oscillatory movement. The values used as input to these metrics are: i) the amplitudes of the oscillation obtained from the sinusoidal fit of the displacement profiles, estimated by correlating the successive echoes; ii) the true amplitude of oscillation. These two metrics are commonly used to quantify the performance of algorithms. The bias (δ_B) is the mean of the error, and the jitter (σ_J) is the standard deviation of the error:

$$\delta_B = \frac{1}{N}\sum_{M=1}^{N} U_M - U \tag{7.5}$$

$$\sigma_J = \sqrt{\frac{1}{N}\sum_{M=1}^{N} (U_M - U - \bar{\delta_B})^2} \tag{7.6}$$

where U_M is the measured amplitude, U is the true amplitude, $\bar{\delta_B}$ is the mean of the bias and N total number of data samples. In this work the vibration frequencies adopted were of 400 Hz, 600 Hz and 800 Hz and 5 cycles with 10 points in each cycle. The amplitude ranged between 0.25 μm to 7.5 μm and signal-to-noise ratios of 10 dB and 20 dB were used. The simulations were performed using Matlab (MathWorks) software.

7.2.4 Experiment

An experimental setup was built to verify the displacement induced to the sphere embedded in a gelatin phantom, versus time. This displacement was induced by tone-burst acoustic radiation force (named here as pushing beam) generated by a focused single element transducer (central frequency of 3 MHz) and focus distance of 70 mm. The transducer was driven by si-

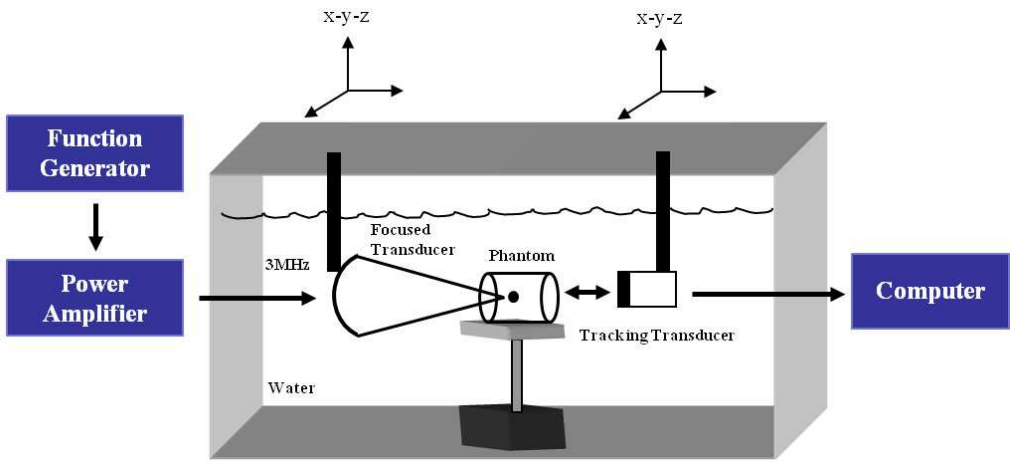

Figure 7.2: Depiction of the experimental setup. The focused pushing transducer was positioned opposite to the 10 MHz tracking transducer.

nusoidal burst signals, generated with an arbitrary function generator (Agilent, model 33220A) amplified by a homemade 20 dB RF power amplifier. Pulses with duration varying from 0.33 ms to 16.66 ms (1000 - 50000 cycles of 3 MHz waves) were used. The motion induced to the target was tracked correlating the echoes obtained through a mono-channel pulse-echo ultrasound (Panametrics model 5601A, Waltham, MA, USA) using a 10 MHz circular transducer positioned opposite to the pushing transducer. Figure 7.2 depicts a schematic representation of the experimental setup.

A second function generator (same model) was trigged every 2 seconds by the generator driving the pushing transducer. The tracking transducer was then trigged by this second function generator, and unless otherwise specified, the pulse repetition frequency of the tracking transducer was PRF=5 kHz. The pulsed ultrasound acquired the reference echoes before the focused transducer had emitted the pushing beam and continued acquiring echoes for 30 ms. The timeline representing the procedure is shown in figure 7.3.

The echo signals were acquired with a sampling rate of 100 MHz through a 8 bits oscilloscope board (National Instruments PCI-5112). The system was controlled through a LabView (National Instruments) applicative.

7.2.5 Phantom production

Gelatin solution was obtained by mixing 4 g of 300 Bloom gelatin (derived from pork skin) per 100 mL of distilled and deionized water (3.8% by weight gelatin) at room temperature and heating to 75 ^{0} C until transparency existed. The molten gelatin was then cooled to 36 ^{0}C and formalin solution which is 37% formaldehyde was added such that 0.047 g were present

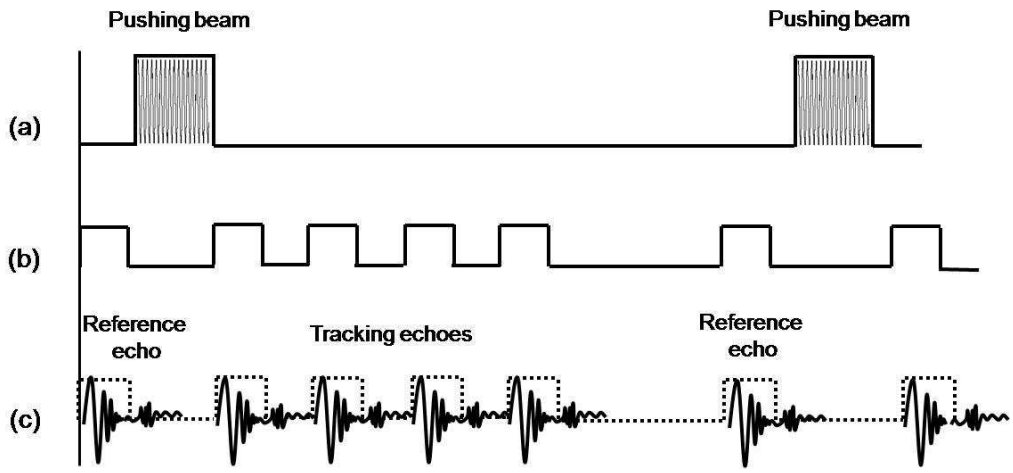

Figure 7.3: Timing diagram for pushing beams excitation and pulses used for tracking the motion. (a) Representation of pushing beams; (b) trigger pulse train sent to the ultrasound equipment; (c) representation of the reference and tracking echoes.

for each gram of (dry weight) gelatin. Formalin was used for cross linking the gelatin, which increases the gelatin's melting point and the elastic modulus [55].

The solution was then poured through a filling syringe barrel into a cylindrical container (height of 25 mm and internal radius of 70 mm) with two layers of plastic film wrap covering each end of the cylinder. A small sphere with radius a=1.50 mm and density ρ=7498 kg/m^3 was suspended with a hair thread in the molted gelatin. To finish, a syringe piston was inserted to assure positive gauge without trapping air bubbles. The phantom rested in the fridge for three days, after this period the hair thread was removed and the sphere remained embedded in the gelatin phantom.

A cylindrical test sample with the same materials concentrations used to make the phantom was also made for measurements of the Young's modulus. The cylinders are 2.6 cm in diameter and 1.0 cm in height. Mechanical tests on this sample were performed using a Bose EnduraTEC 3200 ELF system (Bose Corporation EletrectroForce Systems Group, Minnetonka, MN, USA) appling low amplitude (1% of the sample total heigh), 1 Hz oscillatory compressive load (see section 2.2.4 for a more detailed descrption of the elastic measurement).

7.2.6 Viscoelastic modeling

Moving sphere in viscous fluid and elastic medium in response to static force

The Navier-Stokes equation, for steady flow and small Reynolds number, considering an object moving in an incompressible fluid can be written as (for complete formulation to obtain the Stoke's force acting on a sphere moving in a viscous fluid can be found, for example, in Ref.

[113] p. 58 - 61)

$$\eta \nabla^2 \mathrm{v} - \nabla p = 0 \tag{7.7}$$

where v is the relative velocity between the moving object and the fluid surrounding it, ρ is the fluid density, η is the fluid viscosity and p is the pressure in the fluid. Using eq. (7.7) and the equation of continuity

$$\nabla . \mathrm{v} = 0, \tag{7.8}$$

the Stoke's formula for the drag force exerted on the object by the moving fluid, with velocity v, in the case of a sphere can be derived

$$F_d = -6\pi\eta a v. \tag{7.9}$$

Considering an external constant force acting on the sphere, in the case of a liquid fluid, the object moves while the force is applied. When this force balances with the friction force, due to the fluid viscosity, and the other external forces, i.e. buoyant force, the sphere acceleration becomes null. For a sphere immersed in elastic medium, the external force balances with the force induced by its elastic properties, and the sphere moves to a new equilibrium position. Based on the formulation to deduce the Stoke's drag force caused by the fluid on the moving sphere, and using constitutive equations for elastic materials, Ilinskii et al. [124] deduced an expression for the restoring force exerted by the surrounding medium on the sphere embedded in elastic, isotropic, homogeneous, incompressible and inviscid medium. The restoring force, due to static displacement of the rigid sphere induced by the external force, is

$$F_r = -6\pi\mu u_0 \tag{7.10}$$

where u_0 is the sphere displacement and μ is the shear modulus of the elastic medium. Replacing the shear modulus μ by the viscous coefficient η and the displacement u_0 by the velocity v, eq. (7.10) becomes identical to the Stoke's formula (eq. (7.9)).

Moving sphere in elastic medium in response to time-dependent force

Consider a sphere in oscillatory movement at ω_{osci}, the force representing the resistance towards vibration,

$$F = -Ve^{i\omega_{osci}t}Z, \tag{7.11}$$

can be understood as the vibration velocity times the impedance. The total impedance $Z = Z_m + Z_r$ can be presented as linear combination of the mechanical impedance of the medium Z_m, and the radiation impedance of the object Z_r. Oestreicher et al. [48] derived the dynamic radiation impedance for a rigid sphere vibrating in an isotropic, homogeneous, compressible and viscoelastic media

$$Z_r = -i\frac{4\pi a^3}{3}\rho\omega_{osci} \times \frac{\left[\left(1-\frac{3i}{ah}-\frac{3}{a^2h^2}\right)-2\left(\frac{i}{ah}+\frac{1}{a^2h^2}\right)\left(3-\frac{a^2k^2}{aki+1}\right)\right]}{\left[\left(\frac{i}{ah}+\frac{1}{a^2h^2}\right)\frac{a^2k^2}{aki+1}+\left(2-\frac{a^2k^2}{aki+1}\right)\right]} \tag{7.12}$$

where k is the wave number of the compressional wave $k = \sqrt{\rho\omega_{osci}^2/[2(\mu - i\omega_{osci}\eta)+\lambda^*]}$, h is the wave number of the shear wave $h = \sqrt{\rho\omega_{osci}^2/(\mu - i\omega_{osci}\eta)}$ and $\lambda^* = \lambda_1 + i\omega_{osci}\lambda_2$; λ_1 and λ_2 are the volume elasticity and viscosity of the medium, respectively. The classical Stokes formula for viscous liquids is obtained by putting $\lambda_2 = -2\eta/3$ [48, 113].

The force required to overcome the inertia of the sphere, with mass m is

$$F_m = m\frac{d(Ve^{i\omega_{osci}t})}{dt} = im\omega_{osci}Ve^{i\omega_{osci}t} = -m\omega_{osci}^2Ue^{i\omega_{osci}t}. \tag{7.13}$$

Therefore, the mechanical impedance of the sphere is given by

$$Z_m = -\frac{F_m}{Ve^{i\omega_{osci}t}} = -im\omega_{osci}. \tag{7.14}$$

For a incompressible fluid, we can make the following assumptions; $\mu = 0$, $\lambda_1 = \infty$ and $h = \sqrt{\rho\omega_{osci}^2/i\eta}$ [48]. In the case of a frictionless incompressible elastic medium $\eta = 0$, $\lambda_1 = \infty$ and $h = \omega_{osci}\sqrt{\rho/\mu}$ [48]. Having those assumptions in mind, from eq. (7.12), we can write the radiation impedance as:

$$Z_r = -\frac{2}{3}\pi a^3\rho\omega_{osci}i\left(1-\frac{9i}{ah}-\frac{9}{a^2h^2}\right). \tag{7.15}$$

Substituting eq. (7.14) and eq. (7.15) in eq. (7.11), we obtain a solution for the force towards vibration of the rigid sphere. In the case of incompressible fluid, this force is the same as the drag force on the oscillating sphere (eq. (6.15)) used in chapter 6. In the case of incompressible elastic medium, the external dynamic acoustic radiation force acting on the sphere is

$$F(\omega) = -m\omega^2u(\omega) + \frac{2}{3}\pi a^3\rho\omega^3mu(\omega)\left(1-\frac{9i}{ah}-\frac{9}{a^2h^2}\right). \tag{7.16}$$

The movement of a spherical inhomogeneity, embedded in viscoelastic medium, in time domain can be obtained applying the inverse Fourier transform to the displacement, in frequency

domain, derived from (7.16)

$$u(t) = \frac{1}{2\pi}\int_{-\infty}^{\infty} u(\omega)e^{-i\omega t}. \tag{7.17}$$

Assuming the material, where the sphere is embedded, is inviscid (η=0), the equation of motion in time domain is obtained through eqs. (7.17) and (7.16) and can be written as [124, 107]

$$u + \frac{a}{c_t}\frac{\partial u}{\partial t} + \frac{a^2}{c_t^2}(1+2B)\frac{\partial^2 u}{\partial t^2} = F(t) \tag{7.18}$$

where $c_t = \sqrt{(\mu/\rho)}$ is the shear wave speed and $B = \rho_s/\rho$ is ratio between the solid sphere and the medium densities.

In the experiments of this chapter, the acoustic radiation force acting on the sphere is impulsive given by

$$F(t) = \begin{cases} F_s, & 0 \le t \le t_0 \\ 0, & t > t_0 \end{cases} \tag{7.19}$$

where t_0 is the radiation pulse duration and F_s is the magnitude of the force. Using the force indicated in eq. (7.19), the analytical solution of (7.18) for the movement of the sphere versus time, due to external impulsive force, is [107]

$$u(t) = \begin{cases} \frac{F_s}{6\pi\mu_1 a}\left(1 + \frac{\Lambda_2}{\Lambda_1-\Lambda 2}e^{(c_t/a)\Lambda_1 t} - \frac{\Lambda_1}{\Lambda_2-\Lambda 1}e^{(c_t/a)\Lambda_2 t}\right), & 0 \le t \le t_0 \\ \frac{F_s}{6\pi\mu_1 a}\left((1-e^{-(c_t/a)\Lambda_1 t_0})\frac{\Lambda_2}{\Lambda_1-\Lambda 2}e^{(c_t/a)\Lambda_1 t} - (1-e^{-(c_t/a)\Lambda_2 t_0})\frac{\Lambda_1}{\Lambda_2-\Lambda 1}e^{(c_t/a)\Lambda_2 t}\right), & t > t_0 \end{cases} \tag{7.20}$$

where

$$\Lambda = \frac{3}{2}\frac{-3 \pm \sqrt{5-8B}}{1+2B} \tag{7.21}$$

are the roots of the equation $(1+2B)\Lambda^2 + 9\Lambda + 9 = 0$. The tracked displacements of the sphere obtained in the experiments are compared with analytical predictions using eq. (7.20).

7.3 Results and discussion

7.3.1 Simulation

Figure 7.4 shows the plots of a true simulated harmonic-motion with amplitude of 3 mm (dashed line) and the estimated motion (solid line) via time cross-correlation (eqs. (7.3) and (7.4)) between the first and successive simulated echoes.

Figure 7.5(a) shows the plots of the bias versus vibration amplitude and figure 7.5(b) shows

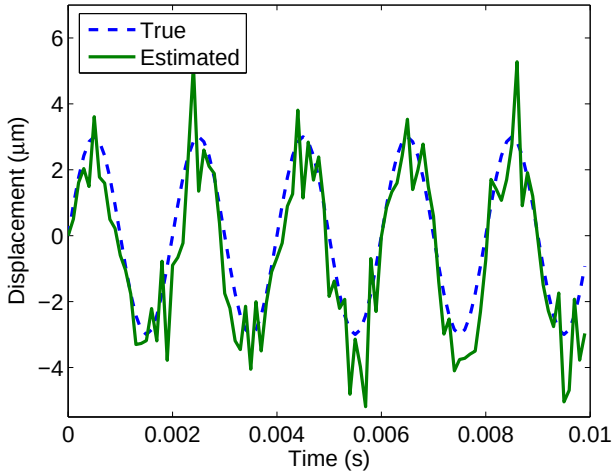

Figure 7.4: True simulated vibration displacement (dashed line) and the motion estimated by correlating the simulated echoes (solid line).

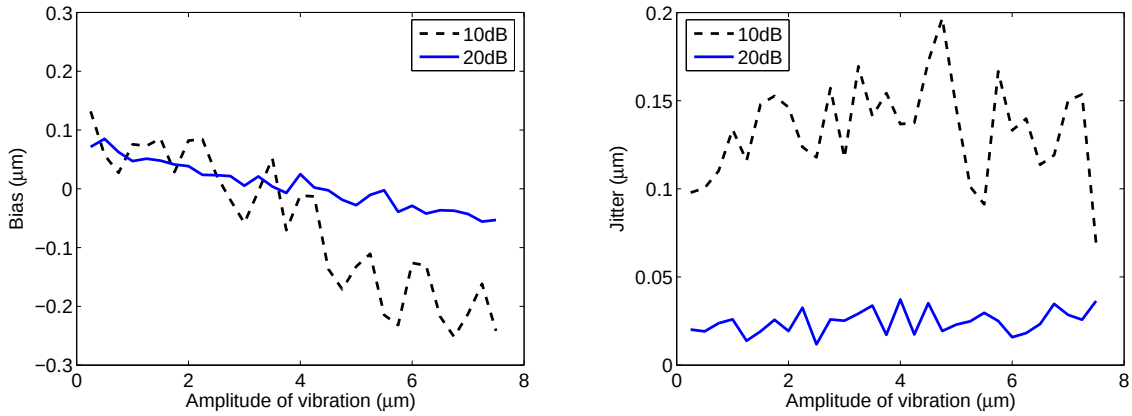

(a) (b)

Figure 7.5: (a) Amplitude bias and (b) amplitude jitter versus vibration amplitude. Simulated ultrasonic echoes with signal-to-noise ratios of 10 dB and 20 dB were used. The vibration frequency of 600 Hz was used in these simulations.

the jitter versus vibration amplitude. These results were obtained using simulated echoes with signal-to-noise ratios of 10 dB and 20 dB. In this case, the vibration frequency was ω_{osci}=600 Hz. These results show that the amplitude bias and amplitude jitter are higher when the ultrasonic echoes presenting lower signal-to-noise ratio values were employed. Therefore, the higher the signal-to-noise ratio, the more accurate (lower bias) and more precise (lower jitter) the motion tracking. For higher amplitudes of vibration ($> 5\mu$m), the amplitude bias increases but is still one order of magnitude lower than the vibration amplitude, indicating good accuracy to track displacement in the range of few micrometers ($< 10\mu$m). The jitter averaged around constant values for both, 10 dB and 20 dB, signal-to-noise ratios values. Those findings agree with the results found by Urban and Greenleaf [118].

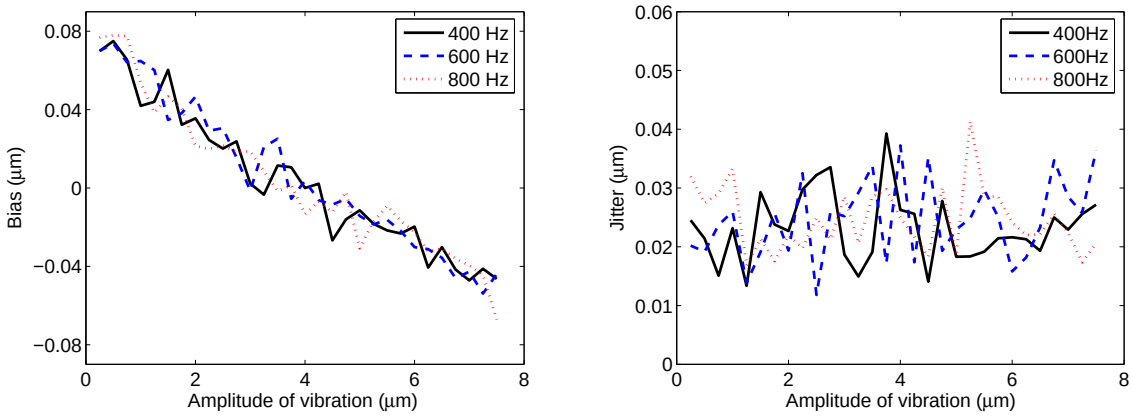

(a) (b)

Figure 7.6: (a) Amplitude bias and (b) amplitude jitter versus vibration amplitude for vibration frequencies of 400 Hz, 600 Hz and 800 Hz and signal-to-noise ratio of 20 dB.

7.3.2 Rigid sphere embedded in gelatin phantom experiment

The echo signal, from the rigid sphere embedded in gelatin phantom, acquired through the mono-channel, pulse-echo ultrasound is shown in figure 7.7. The portions corresponding to the echo from the water - phantom surface transition and the echo from the sphere are indicated in the graph. The speed of sound and the sampling frequency used to calculate the distances were $c = 1500$ m/s and $f_s = 100$ MHz, respectively. The sphere position versus time, tracked through the correlation of ultrasonic echoes, is represented in figure 7.8. The pulse duration of the pushing beam in this case was $t_0 = 6.66$ ms, and the time axis represents the events depicted in figure 7.3. Three regions in the graph illustrate different phenomena: Region 1 depicts the sphere at rest, the echoes used as reference to track the displacement were acquired at this moment; Region 2 depicts the period where the pushing transducer was on and acoustic radiation force displaced the sphere. In this region of the plot, we can see oscillations indicating the cross-talk between both ultrasonic transducers; In Region 3 no acoustic waves were being transmitted and the sphere moved back to its original position.

The position of the sphere, embedded in the gelatin phantom, displaced by pushing beams of different durations (0.33 ms, 1.66 ms and 3.33 ms) is shown in figure 7.9(a). In figure 7.9(a) the oscillations due to the cross-talk between the pushing and tracking transducers were removed for better vizualisation of the motion profiles. In each plot of the graph, those oscillations were replaced by a dotted portion obtained via interpolation technique. The remaining portion corresponds to Region 3 in figure 7.8, where the pushing transducer was off. The simulated displacements, using eq. (7.20), is shown in figure 7.9(b). To simulate these curves the force magnitude used was F_s=475 μN, the gelatin shear modulus was μ=1.5 kPa and the viscosity

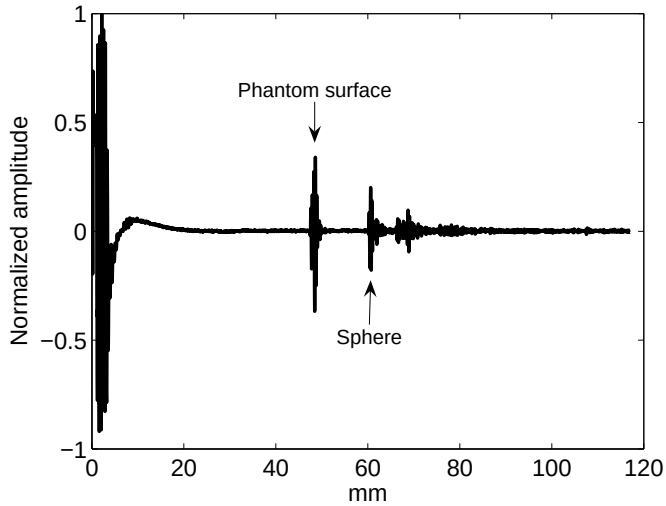

Figure 7.7: Echo signal used to track the motion induced to the sphere. The echoes from the surface of the phantom and the sphere are indicated in the graph.

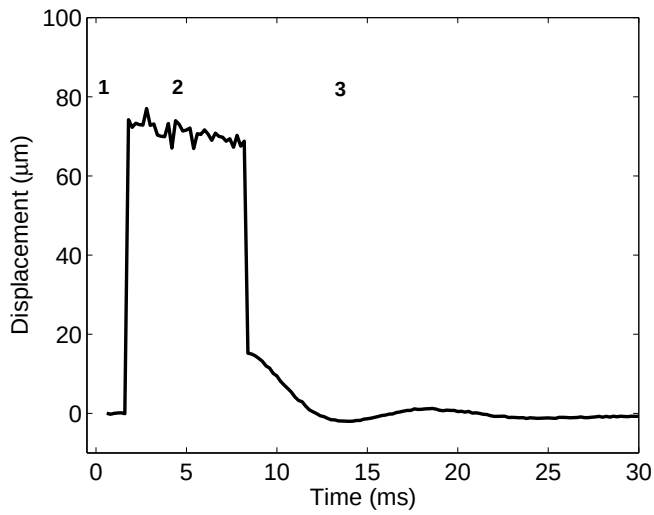

Figure 7.8: Displacement of the sphere versus time obtained from the maximum correlation between the reference and subsequent echoes. Region 1 in the graph is the period just before turning the pushing transducer on (target at rest); Region 2 is the period where the acoustic radiation force was displacing the target, oscillations indicate cross-talk between the tracking and pushing transducers; In region 3 the pushing transducer was off; therefore, the sphere was returning to its original equilibrium position

Table 7.1: Comparison between the experimental and simulated temporal behavior of the sphere displacement. Time to reach the maximum displacements, for different pulse durations, is illustrated.

	t_{max} (ms)	
t_0 (ms)	Experimental	Simulated
0.33	2.1	2.2
1.66	2.9	2.9
3.33	3.9	3.9

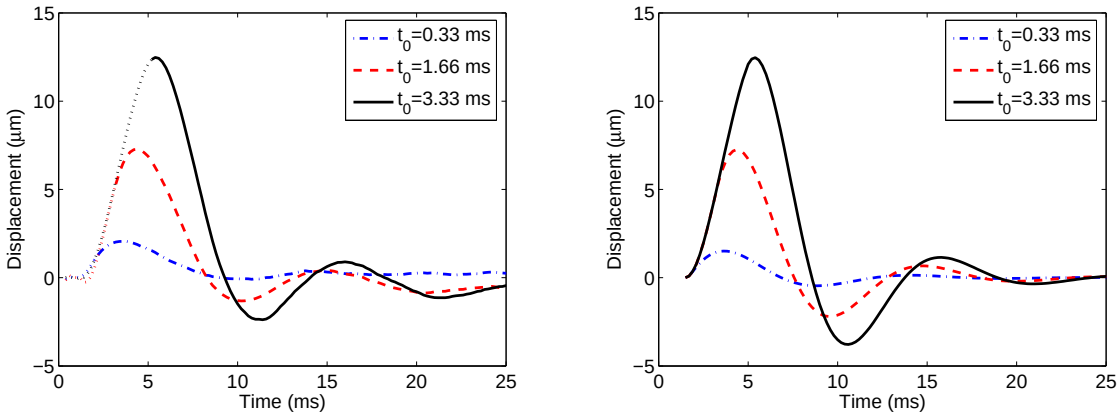

(a) (b)

Figure 7.9: (a) Experimental position versus time of the sphere embedded in gelatin phantom. Pushing beams of different duration were used. Each plot in the graph has a dotted portion correspondent to Region 2 in figure 7.8 and the remaining portion corresponds to Region 3 in figure 7.8. (b) Simulated displacement using acoustic radiation force magnitude F_s=475 μN and gelatin shear modulus μ=1.5 kPa in eq. (7.20).

was η=0 Pa s. The measured, via DMA, storage Young's modulus was E=6 kPa. For incompressible medium the identity $E = 3\mu$ is valid; therefore, the shear modulus becomes μ=2 kPa. The simulated and experimental plots of figure 7.9 agree well; however, the analytical results should be improved by adopting viscosity $\eta \neq 0$ [107]. The gelatin viscosity is usually, adopted to be η=0.1 Pa s [125].

The magnitude of the displacement is proportional to the magnitude of the acoustic radiation force F_s and inversely proportional to the material shear modulus value. The magnitude of the applied force is difficult to be determined, due to the difference in acoustic impedances of the water, gelatin and the sphere. Moreover, the attenuation of the ultrasonic waves traveling through each media also modifies the amplitude of the force. Analyzing (7.20), we observe that the temporal behavior of the displacement is not affected by the magnitude of F_s (see, figure 7.10). The spatio-temporal behavior of the displacement depends on the elasticity of the medium and the pushing beam pulse duration. The experimental and simulated plots of

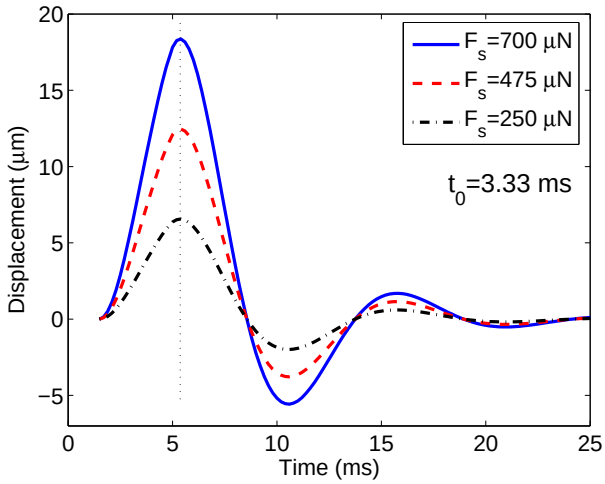

Figure 7.10: Simulated displacement of the solid sphere in response to acoustic radiation force of different magnitudes, F_s=250 μN, F_s=475 μN and F_s=700 μN. The pulse duration is $t_0 =$ 3.33 ms. The displacement profiles show that the temporal behavior does not depend on the magnitude of the force.

figure 7.9 show that the time to the sphere reach its maximum displacement (t_{max}) is longer for longer pulses. For longer pulses, the sphere absorbs more energy, resulting in higher displacement amplitudes. The experimental and simulated values obtained for t_{max} are shown in table 7.1

Figure 7.11 shows the normalized power spectra corresponding to the displacement plots of figure 7.9 in the case of $t_0 = 3.33$ ms (figure 7.11(a)) and $t_0 = 1.66$ ms (figure 7.11(b)). The power spectra correspond to the magnitude of the Fourier transform calculated using 1024 points FFT in embedded Matlab (Mathworks) software. The power spectra of the simulated data has the frequency peak at 95 Hz. The power spectra from the experimental data show two resonant peaks: one around 30 Hz and the other coinciding with the simulated results. The same procedure adopted to estimate the displacement of the sphere was used to calculate the induced displacement of the phantom surface. The result of the frequency response of this displacement is shown in figure 7.12. For the movement of the phantom surface a higher frequency peak at 30 Hz and a lower peak at 95 Hz are observed.

To develop the theory for the radiation impedance of an oscillating sphere embedded in viscoelastic medium, Oestreicher [48] assumed homogeneous medium. A displacement field due to irradiated irrotational compression wave and incompressible shear wave appears, see eq. 15 in Oestreicher's paper [48]. The distance from the sphere to the surface of the phantom is 12.5 mm (see figure 7.7); therefore, the displacement field and the acoustic force acting on the surface of the phantom induce surface motion, consequently, surface waves appear. These waves show lower frequency, long duration, and large amplitude what explains the lower frequency

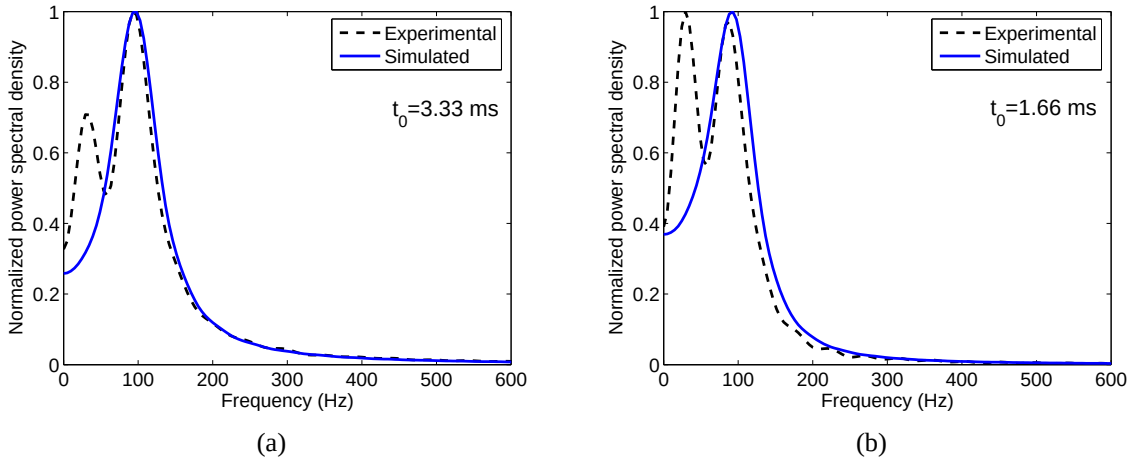

(a) (b)

Figure 7.11: Power spectra of the experimental and simulated movement profiles of the sphere. Pushing pulse duration (a) $t_0 = 3.33$ ms and (b) $t_0 = 1.66$ ms were evaluated.

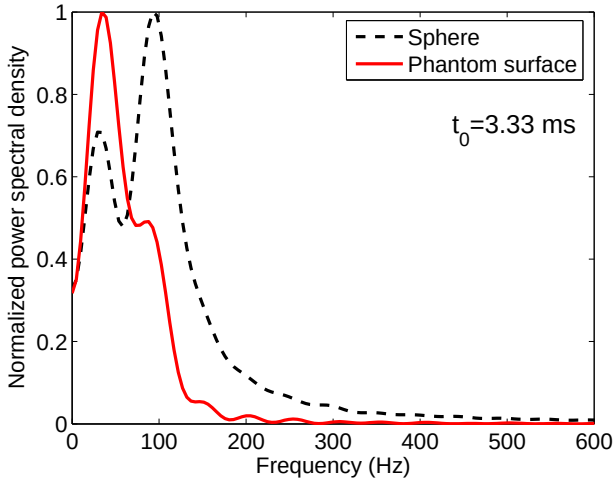

Figure 7.12: Power spectra of the movement profiles of the sphere and the phantom wall. In this case ,the pulse duration was $t_0 = 3.33$ ms.

peak in the displacement power spectrum of the sphere.

7.4 Summary

The feasibility of detecting micrometer vibratory motion through ultrasonic echoes correlation was verified through simulations and experiments. The maximum bias found from the simulated vibration amplitude measurements, using echoes with SNR=20 dB, was 10% of the true simulated amplitude. The methodology describing the acoustic radiation force excitation of a target, and measurement of the induced movement using ultrasonic echoes correlation was presented. The experimental movement profile of a sphere embedded in gelatin phantom displaced by acoustic radiation force agree well with theoretical predictions. From the motion of

the sphere, the elasticity parameter of the medium was estimated and compared with values obtained from DMA method. Displacements up to 12 μm were tracked showing good signal-to-noise ratios.

8 Conclusion and future works

8.1 Nonlinear elastography

A useful approach to characterizing and “optimizing” methodologies for studying nonlinear tissue elasticity is through tissue-mimicking phantom experiments. The hyperelastic behavior of materials commonly used to manufacture phantoms for elastography were analyzed in chapter 2. The insights provided by this study could facilitate development of heterogeneous tissue mimicking phantoms for representing mechanical nonlinearities occurring in normal and abnormal tissues. Future direction to improve this research is to understand the microscopic process involved with the changes in the nonlinear behavior of the phantom materials. The insights provided by this investigation may help to improve the understanding of the microscopic process involved with the changes in the nonlinear behavior of biological tissues. Evaluation of the anisotropy and viscosity of materials made of agar, gelatin and agar/gelatin mixtures with oil droplets dispersion is an opportunity to improve the work explored in chapter 2.

Chapter 3 reports on a phantom containing spherical inclusions crated using information about the nonlinear behavior of agar/gelatin mixtures and agar/gelatin with oil emulsification. The phantom contains four spherical inclusions, each with distinct small-strain Young’s modulus and nonlinear mechanical behavior that is different from that of the background material. An experimental approach to evaluate changes in contrast, signal-to-noise ratio and contrast-to-noise ratio between inclusion and background for large deformations (up to 20%) when the stress/strain relationship for the materials is nonlinear was explored. In this study was verified that the nonlinear elastic behavior of the media being imaged may not improve the quality of the strain images but might provide additional information which can be useful to differentiate types of materials or tissues. The raw data used to construct the strain images and the displacement and stress fields obtained via FEA simulation are being evaluated to reconstruct absolute values for the shear modulus and nonlinear parameter distributions of the phantom. To achieve this goal, approaches that are inverse problems based on the mechanical constitutive laws are being employed.

8.2 Acoustic radiation force-based elastography

Ultrasonic and magnetic approaches to detect micro-order displacements induced by time-dependent acoustic radiation force were investigated. Experiments of chapter 5 demonstrated that the single channel continuous wave (CW) Doppler system is an alternative to detect small vibrations induced by dynamic acoustic radiation force. The ability to form images of a rigid spherical inhomogeneity embedded in viscoelastic phantom by scanning both ultrasonic transducers (confocal and Doppler) across the confocal transducer focal plane was qualitatively compared to images simulated by the spatial convolution of the point spread function (PFS) with the simulated true object. The used Doppler system is a non expensive ultrasound, has fast response, what easily allows building an image of the scanned sample. The drawback of this system is the non absolute output values for the amplitude of vibration. Employing a custom-made CW Doppler system, which allows controlling the transmitted ultrasonic waves and permits accessing the raw echo data could enhance the ability of this system to estimate absolute parameters of the vibration.

The methodology describing the acoustic radiation force excitation of a target, and measurement of the induced movement using ultrasonic echoes correlation was presented in chapter 7. The motion of a rigid sphere embedded in gelatin phantom, induced by acoustic radiation force, was estimated. Displacements up to 12 μm were tracked showing good signal-to-noise ratios. Absolute displacement values are achieved by tracking the displacement using ultrasonic echoes time-delay estimators. This is a powerful tool that can be employed in various scientific applications. In the GIIMUS Lab., for example, the movement of magnetic particles induced by magnetic fields is, currently, being estimated using the developed tool.

The movement of a simple pendulum, composed of a magnetic sphere and displaced by acoustic radiation force, was evaluated in chapter 6. The displacements were on the order of a micrometer and were tracked using a magnetoresistive sensor. The experimental displacement plots showed good signal-to-noise ratios for displacements of a few micrometers and agreed well with theoretical predictions. From the displacement of the sphere, values for the water viscosity were estimated with good accuracy. To estimate the viscosity, the drag force acting on the pendulum during its motion was considered to follow a modified Stokes law for a low Reynolds number, accounting for the phenomena related to its oscillatory movement. The viscosity of different fluids is being investigated using ultrasonic excitation and magnetic detection. Ultrasonic pulsed and dynamic excitations will be explored. The advantages of using magnetic detection over the Laser vibrometry are that opaque fluids can be analyzed and the relatively low-cost of the system. Compared to ultrasonic tracking strategies, the magnetic permits evaluating higher

vibration frequencies.

8.3 Final considerations

It has been over two decades since the first attempt to image the local elastic properties of tissues. In these 20 years, an enormous quantity of techniques and algorithms were developed to increment the range of applications and improve the elasticity images quality. In the last decade, the number of publications of clinical trials started to increase. An overview of selected techniques was covered in the main introduction (chapter 1) of this thesis. The directions guiding the future researches to increase the range of applications and consolidate the basis of elasticity imaging are based on the following aspects: i) improve the set of techniques that are well suited for clinical investigations, integrated or not to scanners; ii) understand the biologic processes, i.e., cellular alterations, related to the observed changes in diseased tissues and organs; iii) improve the range of mechanical parameters inspected. Currently, most of the techniques estimate relative stiffness and Young's modulus, parameters as: viscosity, homogeneity, nonlinearity and anisotropy can be more explored; iv) involve different physical phenomena to the ultrasonic elasticity techniques, i.e., optics and magnetism. The popularity of the techniques using the interaction between ultrasonic compression waves with mechanical shear waves shows that integrating more than one physical phenomena is a promising step forward.

Bibliography

[1] G. Schwartsmann, "Breast cancer in South America: challenges to improve early detection and medical management of a public health problem," *Journal of Clinical Oncology*, vol. 19, no. 2001, pp. 118s–124s, 2001.

[2] C. P. McPherson, K. K. Swenson, G. Jolitz, and C. L. Murray, "Survival of women ages 40-49 years with breast carcinoma according to method of detection," *Cancer*, vol. 79, no. 10, pp. 1923–1932, 2000.

[3] D. V. Schapira and R. B. Levine, "Breast cancer screening and compliance and evaluation of lesions." *The Medical clinics of North America*, vol. 80, no. 1, p. 15, 1996.

[4] R. Muthupillai, D. J. Lomas, P. J. Rossman, J. F. Greenleaf, A. Manduca, and R. L. Ehman, "Magnetic resonance elastography by direct visualization of propagating acoustic strain waves," *Science*, vol. 269, no. 5232, p. 1854, 1995.

[5] J. Ophir, S. K. Alam, B. Garra, F. Kallel, E. Konofagou, T. Krouskop, and T. Varghese, "Elastography: ultrasonic estimation and imaging of the elastic properties of tissues," *Proceedings of the Institution of Mechanical Engineers, Part H: Journal of Engineering in Medicine*, vol. 213, no. 3, pp. 203–233, 1999.

[6] J. Ophir, I. Cespedes, H. Ponnekanti, Y. Yazdi, and X. Li, "Elastography: a quantitative method for imaging the elasticity of biological tissues," *Ultrasonic Imaging*, vol. 13, no. 2, pp. 111–134, 1991.

[7] O. Bonnefous and P. Pesque, "Time domain formulation of pulse-Doppler ultrasound and blood velocity estimation by cross correlation," *Ultrasonic Imaging*, vol. 8, no. 2, pp. 73–85, 1986.

[8] F. Viola and W. Walker, "A comparison of the performance of time-delay estimators in medical ultrasound," *IEEE Transactions on Ultrasonics, Ferroelectrics and Frequency Control*, vol. 50, no. 4, pp. 392–401, 2003.

[9] Y. Zhu and T. J. Hall, "A modified block matching method for real-time freehand strain imaging," *Ultrasonic Imaging*, vol. 24, no. 3, pp. 161–176, 2002.

[10] A. R. Skovoroda, S. Y. Emelianov, and M. O'Donnell, "Tissue elasticity reconstruction based on ultrasonic displacementand strain images," *IEEE Transactions on Ultrasonics, Ferroelectrics and Frequency Control*, vol. 42, no. 4, pp. 747–765, 1995.

[11] C. Sumi, A. Suzuki, and K. Nakayama, "Estimation of shear modulus distribution in soft tissue from straindistribution," *IEEE Transactions on Biomedical Engineering*, vol. 42, no. 2, pp. 193–202, 1995.

[12] A. A. Oberai, N. H. Gokhale, and G. R. Feijoo, "Solution of inverse problems in elasticity imaging using the adjoint method," *Inverse Problems*, vol. 19, pp. 297–313, 2003.

[13] P. E. Barbone and J. C. Bamber, "Quantitative elasticity imaging," *Physics in Medicine and Biology*, vol. 47, pp. 2147–2164, 2002.

[14] F. Kallel, J. Ophir, K. Magee, and T. Krouskop, "Elastographic imaging of low-contrast elastic modulus distributions in tissue," *Ultrasound in Medicine & Biology*, vol. 24, no. 3, pp. 409–425, 1998.

[15] F. Kallel, R. E. Price, E. Konofagou, and J. Ophir, "Elastographic imaging of the normal canine prostate in vitro." *Ultrasonic Imaging*, vol. 21, no. 3, p. 201, 1999.

[16] B. S. Garra, E. I. Cespedes, J. Ophir, S. R. Spratt, R. A. Zuurbier, C. M. Magnant, and M. F. Pennanen, "Elastography of breast lesions: initial clinical results." *Radiology*, vol. 202, no. 1, p. 79, 1997.

[17] E. Konofagou, J. D'hooge, and J. Ophir, "Myocardial elastography–a feasibility study in vivo," *Ultrasound in Medicine & Biology*, vol. 28, no. 4, pp. 475–482, 2002.

[18] C. de Korte, E. Céspedes, A. van der Steen, and C. Lancée, "Intravascular elasticity imaging using ultrasound: feasibility studies in phantoms," *Ultrasound in Medicine & Biology*, vol. 23, no. 5, pp. 735–746, 1997.

[19] T. Varghese, J. A. Zagzebski, and F. T. Lee, "Elastographic imaging of thermal lesions in the liver in vivo following radiofrequency ablation: preliminary results," *Ultrasound in Medicine & Biology*, vol. 28, no. 11-12, pp. 1467–1473, 2002.

[20] J. Jiang, T. Varghese, C. Brace, E. L. Madsen, T. J. Hall, S. Bharat, M. Hobson, J. Zagzebski, and J. F. Lee, "Young's Modulus Reconstruction for Radio-Frequency Ablation Electrode-Induced Displacement Fields: A Feasibility Study." *IEEE Transactions on Medical Imaging*, 2009.

[21] T. A. Krouskop, T. M. Wheeler, F. Kallel, B. S. Garra, and T. Hall, "Elastic moduli of breast and prostate tissues under compression," *Ultrasonic Imaging*, vol. 20, no. 4, pp. 260–274, 1998.

[22] Y. C. Fung, *Biomechanics: mechanical properties of living tissues*. New York: Springer-Verlag, 1993.

[23] P. Wellman, *Tactile imaging*. PhD thesis, Harvard University, 1999.

[24] T. J. Hall, Y. Zhu, and C. S. Spalding, "In vivo real-time freehand palpation imaging," *Ultrasound in Medicine & Biology*, vol. 29, no. 3, pp. 427–435, 2003.

[25] R. Rivlin and D. Saunders, "Large elastic deformations of isotropic materials. VII. Experiments on the deformation of rubber," *Philosophical Transactions of the Royal Society of London. Series A, Mathematical and Physical Sciences*, vol. 243, no. 865, pp. 251–288, 1951.

[26] R. Ogden, "Large deformation isotropic elasticity-on the correlation of theory and experiment for incompressible rubberlike solids," *Proceedings of the Royal Society of London. Series A, Mathematical and Physical Sciences*, vol. 326, no. 1567, pp. 565–584, 1972.

[27] O. Yeoh, “Some forms of the strain energy function for rubber,” *Rubber Chemistry and Technology*, vol. 66, no. 5, pp. 754–771, 1993.

[28] D. R. Veronda and R. A. Westmann, “Mechanical characterization of skin-finite deformations.” *Journal of Biomechanics*, vol. 3, no. 1, pp. 111–124, 1970.

[29] E. Arruda and M. Boyce, “A three-dimensional constitutive model for the large stretch behavior of rubber elastic materials,” *Journal of the Mechanics and Physics of Solids*, vol. 41, no. 2, pp. 389–412, 1993.

[30] J. J. O’Hagan and A. Samani, “Measurement of the hyperelastic properties of 44 pathological ex vivo breast tissue samples,” *Physics in Medicine and Biology*, vol. 54, no. 8, pp. 2557–2569, 2009.

[31] T. Z. Pavan, E. L. Madsen, G. R. Frank, A. A. O. Carneiro, and T. J. Hall, “Nonlinear elastic behavior of phantom materials for elastography,” *Physics in Medicine and Biology*, vol. 55, pp. 2679–2692, 2010.

[32] R. Q. Erkamp, S. Y. Emelianov, A. R. Skovoroda, and M. O’Donnell, “Nonlinear elasticity imaging: theory and phantom study,” *IEEE Transactions on Ultrasonics, Ferroelectrics and Frequency Control*, vol. 51, no. 5, pp. 532–539, 2004a.

[33] N. Nitta and T. Shiina, “Estimation of nonlinear elasticity parameter of tissues by ultrasound,” *Japanese Journal of Applied Physics*, vol. 41, pp. 3572–3578, 2002.

[34] A. A. Oberai, N. H. Gokhale, S. Goenezen, P. E. Barbone, T. J. Hall, A. M. Sommer, and J. Jiang, “Linear and nonlinear elasticity imaging of soft tissue in vivo: demonstration of feasibility,” *Physics in Medicine and Biology*, vol. 54, no. 5, pp. 1191–1207, 2009.

[35] R. M. Lerner, S. R. Huang, and K. J. Parker, “Sonoelasticity images derived from ultrasound signals in mechanically vibrated tissues,” *Ultrasound in Medicine and Biology*, vol. 16, no. 3, pp. 231–239, 1990.

[36] S. Catheline, J. L. Thomas, F. Wu, and M. A. Fink, “Diffraction field of a low frequency vibrator in soft tissues usingtransient elastography,” *IEEE Transactions on Ultrasonics, Ferroelectrics and Frequency Control*, vol. 46, no. 4, pp. 1013–1019, 1999.

[37] T. Sugimoto, S. Ueha, and K. Itoh, “Tissue hardness measurement using the radiation force of focusedultrasound,” in *Proceedings of the IEEE Ultrasonics Symposium*, 1990, pp. 1377–1380.

[38] K. Nightingale, M. S. Soo, R. Nightingale, and G. Trahey, “Acoustic radiation force impulse imaging: in vivo demonstration of clinical feasibility,” *Ultrasound in Medicine & Biology*, vol. 28, no. 2, pp. 227–235, 2002.

[39] E. L. Madsen, M. A. Hobson, G. R. Frank, H. Shi, J. Jiang, T. J. Hall, T. Varghese, M. M. Doyley, and J. B. Weaver, “Anthropomorphic breast phantoms for testing elastography systems,” *Ultrasound in Medicine & Biology*, vol. 32, no. 6, p. 857, 2006.

[40] A. P. Sarvazyan, O. V. Rudenko, S. D. Swanson, J. B. Fowlkes, and S. Y. Emelianov, “Shear wave elasticity imaging: a new ultrasonic technology of medical diagnostics,” *Ultrasound in Medicine & Biology*, vol. 24, no. 9, pp. 1419–1435, 1998.

[41] K. Nightingale, S. McAleavey, and G. Trahey, "Shear-wave generation using acoustic radiation force: in vivo and ex vivo results," *Ultrasound in Medicine & Biology*, vol. 29, no. 12, pp. 1715–1723, 2003.

[42] T. Deffieux, G. Montaldo, M. Tanter, and M. Fink, "Shear wave spectroscopy for in vivo quantification of human soft tissues visco-elasticity." *IEEE Transactions on Medical Imaging*, vol. 28, no. 3, p. 313, 2009.

[43] J. Bercoff, M. Tanter, and M. Fink, "Supersonic shear imaging: a new technique for soft tissue elasticity mapping," *IEEE Transactions on Ultrasonics, Ferroelectrics and Frequency Control*, vol. 51, no. 4, pp. 396–409, 2004.

[44] ——, "Sonic boom in soft materials: The elastic Cerenkov effect," *Applied Physics Letters*, vol. 84, no. 12, pp. 2202–2204, 2004.

[45] G. Montaldo, M. Tanter, J. Bercoff, N. Benech, and M. Fink, "Coherent plane-wave compounding for very high frame rate ultrasonography and transient elastography," *IEEE Transactions on Ultrasonics, Ferroelectrics and Frequency Control*, vol. 56, no. 3, pp. 489–506, 2009.

[46] M. Fatemi and J. F. Greenleaf, "Ultrasound-stimulated vibro-acoustic spectrography," *Science*, vol. 280, no. 5360, p. 82, 1998.

[47] A. O. Carneiro, O. Baffa, G. T. Silva, and M. Fatemi, "Vibro-Magnetometry: Theoretical Aspects and Simulations," *IEEE Transactions on Ultrasonics, Ferroelectrics and Frequency Control*, vol. 56, no. 5, pp. 1065–1073, 2009.

[48] H. L. Oestreicher, "Field and impedance of an oscillating sphere in a viscoelastic medium with an application to biophysics," *The Journal of the Acoustical Society of America*, vol. 23, p. 707, 1951.

[49] G. T. Silva, S. Chen, and L. P. Viana, "Parametric amplification of the dynamic radiation force of acoustic waves in fluids," *Physical review letters*, vol. 96, no. 23, p. 234301, 2006.

[50] H. A. S. Kamimura, T. Z. Pavan, T. W. J. Almeida, M. L. A. Padua, A. L. Baggio, M. Fatemi, and A. A. O. Carneiro, "Pressure transducer for measuring acoustic radiation force based on a magnetic sensor," *Measurement Science & Technology*, vol. 22, p. 015101, 2011.

[51] J. Jiang and T. J. Hall, "A parallelizable real-time motion tracking algorithm with applications to ultrasonic strain imaging," *Physics in Medicine and Biology*, vol. 52, no. 13, pp. 3773–3790, 2007.

[52] T. J. Hall, "Beyond the basics: Elasticity imaging with us," *Radiographics*, vol. 23, no. 6, pp. 1657–1671, 2003.

[53] J. D. Humphrey and S. L. Delange, *An introduction to biomechanics: solids and fluids, analysis and design*. Springer Verlag, 2004.

[54] C. Storm, J. J. Pastore, F. C. MacKintosh, T. C. Lubensky, and P. A. Janmey, "Nonlinear elasticity in biological gels," *Nature*, vol. 435, no. 7039, pp. 191–194, 2005.

[55] T. J. Hall, M. Bilgen, M. F. Insana, and T. A. Krouskop, "Phantom materials for elastography," *IEEE Transactions on Ultrasonics, Ferroelectrics and Frequency Control*, vol. 44, no. 6, pp. 1355–1365, 1997.

[56] E. L. Madsen, M. A. Hobson, H. Shi, T. Varghese, and G. R. Frank, "Tissue-mimicking agar/gelatin materials for use in heterogeneous elastography phantoms," *Physics in Medicine and Biology*, vol. 50, no. 23, pp. 5597–5618, 2005a.

[57] H. Nakakura, F. Nishigaki, M. Sambuichi, Y. Miura, and K. Osasa, "Studies on mechanical compression properties of gels," *Nippon Shokuhin Kogyo Gakkaishi*, vol. 39, no. 1, pp. 8–15, 1992.

[58] R. Q. Erkamp, A. R. Skovoroda, S. Y. Emelianov, and M. O'Donnell, "Measuring the nonlinear elastic properties of tissue-like phantoms," *IEEE Transactions on Ultrasonics, Ferroelectrics and Frequency Control*, vol. 51, no. 4, pp. 410–419, APR 2004b.

[59] N. H. Gokhale, P. E. Barbone, and A. A. Oberai, "Solution of the nonlinear elasticity imaging inverse problem: the compressible case," *Inverse Problems*, vol. 435, no. 4, p. 045010, 2008.

[60] J. L. Gennisson, M. Renier, S. Catheline, C. Barriere, J. Bercoff, M. Tanter, and M. Fink, "Acoustoelasticity in soft solids: Assessment of the nonlinear shear modulus with the acoustic radiation force," *The Journal of the Acoustical Society of America*, vol. 122, no. 6, pp. 3211–3219, 2007.

[61] K. C. Labropoulos, D. E. Niesz, S. C. Danforth, and P. G. Kevrekidis, "Dynamic rheology of agar gels: theory and experiments. Part I. Development of a rheological model," *Carbohydrate Polymers*, vol. 50, no. 4, pp. 393–406, 2002.

[62] T. Fujii, T. Yano, H. Kumagai, and O. Miyawaki, "Scaling analysis of the concentration dependence on elasticity of agarose gel," *Bioscience, Biotechnology, and Biochemistry*, vol. 64, no. 8, pp. 1618–1622, 2000.

[63] A. H. Clark, R. K. Richardson, S. B. Ross-Murphy, and J. M. Stubbs, "Structural and mechanical properties of agar/gelatin co-gels. Small-deformation studies," *Macromolecules*, vol. 16, no. 8, pp. 1367–1374, 1983.

[64] H. Horiuchi and J. Sugiyama, "Mechanical and structural properties of agar-gelatin mixed gels," *Agricultural and Biological Chemistry*, vol. 51, no. 8, pp. 2171–2176, 1987.

[65] P. G. De Gennes, "Relation between percolation theory and the elasticity of gels," *Journal de Physique Lettres*, vol. 37, no. 1, pp. 1–2, 1976.

[66] T. Ikeda, M. Tokita, A. Tsutsumi, and K. Hikichi, "Critical elasticity of gelatin gel," *Japanese Journal of Applied Physics*, vol. 28, no. part 1, pp. 1639–1643, 1989.

[67] M. Djabourov, J. Leblond, and P. Papon, "Gelation of aqueous gelatin solutions. II. Rheology of the sol-gel transition," *Journal de Physique*, vol. 49, no. 2, pp. 333–343, 1988.

[68] E. L. Madsen, G. R. Frank, T. A. Krouskop, T. Varghese, F. Kallel, and J. Ophir, "Tissue-mimicking oil-in-gelatin dispersions for use in heterogeneous elastography phantoms," *Ultrasonic Imaging*, vol. 25, no. 1, pp. 17–38, 2003.

[69] E. L. Madsen, M. A. Hobson, H. Shi, T. Varghese, and G. R. Frank, "Stability of heterogeneous elastography phantoms made from oil dispersions in aqueous gels," *Ultrasound in Medicine & Biology*, vol. 32, no. 2, pp. 261–270, 2006.

[70] K. Levenberg, "A method for the solution of certain nonlinear problems in least squares," *Quart. Appl. Math*, vol. 2, no. 2, pp. 164–168, 1944.

[71] D. W. Marquardt, "An algorithm for least-squares estimation of nonlinear parameters," *Journal of the Society for Industrial and Applied Mathematics*, pp. 431–441, 1963.

[72] K. H. Kim, S. Gohtani, R. Matsuno, and Y. Yamano, "Effects of oil droplet and agar concentration on gel strength and microstructure of O/W emulsion gel," *Journal of Texture Studies*, vol. 30, no. 3, pp. 319–336, 1999.

[73] T. Varghese, J. Ophir, and T. A. Krouskop, "Nonlinear stress-strain relationships in tissue and their effect on the contrast-to-noise ratio in elastograms," *Ultrasound in Medicine & Biology*, vol. 26, no. 5, pp. 839–851, 2000.

[74] A. R. Skovoroda, L. A. Lubinski, S. Y. Emelianov, and M. O'Donnell, "Reconstructive elasticity imaging for large deformations," *IEEE Transactions on Ultrasonics, Ferroelectrics and Frequency Control*, vol. 46, no. 3, pp. 523–535, 1999.

[75] S. Catheline, J. L. Gennisson, and M. Fink, "Measurement of elastic nonlinearity of soft solid with transient elastography," *The Journal of the Acoustical Society of America*, vol. 114, p. 3087, 2003.

[76] R. Sinkus, J. Bercoff, M. Tanter, J. L. Gennisson, C. El Khoury, V. Servois, A. Tardivon, and M. Fink, "Nonlinear viscoelastic properties of tissue assessed by ultrasound," *IEEE Transactions on Ultrasonics, Ferroelectrics and Frequency Control*, vol. 53, no. 11, pp. 2009–2018, 2006.

[77] J. M. Kofler *et al.*, "Improved method for determining resolution zones in ultrasound phantoms with spherical simulated lesions," *Ultrasound in Medicine & Biology*, vol. 27, no. 12, pp. 1667–1676, 2001.

[78] E. L. Madsen, G. R. Frank, M. A. Hobson, H. Shi, J. Jiang, T. Varghese, and T. J. Hall, "Spherical lesion phantoms for testing the performance of elastography systems," *Physics in Medicine and Biology*, vol. 50, p. 5983, 2005b.

[79] M. Hobson, E. Madsen, G. Frank, J. Jiang, H. Shi, T. Hall, and T. Varghese, "Anthropomorphic Phantoms for Assessment of Strain Imaging Methods Involving Saline-Infused Sonohysterography," *Ultrasound in Medicine & Biology*, vol. 34, no. 10, p. 1622, 2008.

[80] E. L. Madsen, J. C. Blechinger, and G. R. Frank, "Low-contrast focal lesion detectability phantom for H-1 MR Imaging," *Medical Physics*, vol. 18, no. 3, pp. 549–554, 1991.

[81] J. Jiang, T. J. Hall, and A. M. Sommer, "A novel image formation method for ultrasonic strain imaging," *Ultrasound in Medicine & Biology*, vol. 33, no. 4, pp. 643–652, 2007.

[82] H. Ponnekanti, J. Ophir, Y. Huang, and I. Céspedes, "Fundamental mechanical limitations on the visualization of elasticity contrast in elastography," *Ultrasound in Medicine & Biology*, vol. 21, no. 4, pp. 533–543, 1995.

[83] F. Kallel, M. Bertrand, and J. Ophir, "Fundamental limitations on the contrast-transfer efficiency in elastography: an analytic study." *Ultrasound in Medicine & Biology*, vol. 22, no. 4, p. 463, 1996.

[84] M. Bilgen and M. F. Insana, "Elastostatics of a spherical inclusion in homogeneous biological media," *Physics in Medicine and Biology*, vol. 43, pp. 1–20, 1998.

[85] T. Varghese and J. Ophir, "An analysis of elastographic contrast-to-noise ratio," *Ultrasound in Medicine & Biology*, vol. 24, no. 6, pp. 915–924, 1998.

[86] ——, "The nonstationary strain filter in elastography: Part I. frequency dependent attenuation," *Ultrasound in Medicine & Biology*, vol. 23, no. 9, pp. 1343–1356, 1997.

[87] H. T. O'Neil, "Theory of focusing radiators," *The Journal of the Acoustical Society of America*, vol. 21, no. 5, pp. 516–526, 1949.

[88] E. L. Madsen, M. M. Goodsitt, and J. A. Zagzebski, "Continuous waves generated by focused radiators," *The Journal of the Acoustical Society of America*, vol. 70, p. 1508, 1981.

[89] B. G. Lucas and T. G. Muir, "The field of a focusing source," *The Journal of the Acoustical Society of America*, vol. 72, p. 1289, 1982.

[90] X. Chen, K. Q. Schwarz, and K. J. Parker, "Radiation pattern of a focused transducer: A numerically convergent solution," *The Journal of the Acoustical Society of America*, vol. 94, pp. 2979–2979, 1993.

[91] S. Chen, M. Fatemi, R. Kinnick, and J. F. Greenleaf, "Comparison of stress field forming methods for vibro-acoustography," *IEEE Transactions on Ultrasonics, Ferroelectrics and Frequency Control*, vol. 51, no. 3, pp. 313–321, 2004.

[92] M. Fatemi and J. F. Greenleaf, "Vibro-acoustography: An imaging modality based on ultrasound-stimulated acoustic emission," *Proceedings of the National Academy of Sciences of the United States of America*, vol. 96, no. 12, p. 6603, 1999.

[93] E. E. Konofagou and K. Hynynen, "Localized harmonic motion imaging: theory, simulations and experiments," *Ultrasound in Medicine & Biology*, vol. 29, no. 10, pp. 1405–1413, 2003.

[94] Y. Zheng, S. Chen, W. Tan, R. Kinnick, and J. F. Greenleaf, "Detection of tissue harmonic motion induced by ultrasonic radiation force using pulse-echo ultrasound and Kalman filter," *IEEE Transactions on Ultrasonics, Ferroelectrics and Frequency Control*, vol. 54, no. 2, pp. 290–300, 2007.

[95] A. G. Petculescu and J. M. Sabatier, "Air-coupled ultrasonic sensing of grass-covered vibrating surfaces; qualitative comparisons with laser Doppler vibrometry," *The Journal of the Acoustical Society of America*, vol. 115, p. 1557, 2004.

[96] D. Censor, "Harmonic and transient scattering from time varying obstacles," *J. Acoust. Soc. Am*, vol. 76, p. 5, 1984.

[97] J. C. Piquette and A. L. Van Buren, "Comments on 'Harmonic and transient scattering from time varying obstacles'," *J. Acoust. Soc. Am*, vol. 76, pp. 1527–1534, 1984.

[98] S. R. Huang, R. M. Lerner, and K. J. Parker, "Time domain Doppler estimators of the amplitude of vibrating targets," *The Journal of the Acoustical Society of America*, vol. 91, p. 965, 1992.

[99] A. Kannath and R. J. Dewhurst, "Real-time measurement of acoustic field displacements using ultrasonic interferometry," *Measurement Science and Technology*, vol. 15, p. N59, 2004.

[100] S. Chen, *Shear property characterization of viscoelastic media using vibrations induced by ultrasound radiation force*. PhD thesis, Mayo Graduate School, 2002.

[101] G. T. Silva, S. Chen, J. F. Greenleaf, and M. Fatemi, "Dynamic ultrasound radiation force in fluids," *Physical Review E*, vol. 71, no. 5, p. 56617, 2005.

[102] P. Westervelt, "The theory of steady forces caused by sound waves," *The Journal of the Acoustical Society of America*, vol. 23, p. 312, 1951.

[103] A. D. Pierce, *Acoustics: an introduction to its physical principles and applications*. Acoustical Society of America, 1989.

[104] G. Torr, "The acoustic radiation force," *American Journal of Physics*, vol. 52, p. 402, 1984.

[105] S. Chen, G. T. Silva, R. R. Kinnick, J. F. Greenleaf, and M. Fatemi, "Measurement of dynamic and static radiation force on a sphere," *Physical Review E*, vol. 71, no. 5, p. 56618, 2005.

[106] J. F. Greenleaf, M. Fatemi, and M. Insana, "Selected methods for imaging elastic properties of biological tissues." *Annual Review of Biomedical Engineering*, vol. 5, p. 57, 2003.

[107] S. R. Aglyamov, A. B. Karpiouk, Y. A. Ilinskii, E. A. Zabolotskaya, and S. Y. Emelianov, "Motion of a solid sphere in a viscoelastic medium in response to applied acoustic radiation force: Theoretical analysis and experimental verification," *The Journal of the Acoustical Society of America*, vol. 122, p. 1927, 2007.

[108] A. B. Karpiouk, S. R. Aglyamov, Y. A. Ilinskii, E. A. Zabolotskaya, and S. Y. Emelianov, "Assessment of shear modulus of tissue using ultrasound radiation force acting on a spherical acoustic inhomogeneity." *IEEE Transactions on Ultrasonics, Ferroelectrics and Frequency Control*, vol. 56, no. 11, p. 2380, 2009.

[109] M. Orescanin, K. Toohey, and M. Insana, "Material properties from acoustic radiation force step response," *The Journal of the Acoustical Society of America*, vol. 125, p. 2928, 2009.

[110] S. Chen, M. Fatemi, and J. F. Greenleaf, "Remote measurement of material properties from radiation force induced vibration of an embedded sphere," *The Journal of the Acoustical Society of America*, vol. 112, p. 884, 2002.

[111] F. Dunn, A. J. Averbuch, and W. D. O'Brien Jr, "A primary method for the determination of ultrasonic intensity with the elastic sphere radiometer," *Acustica*, vol. 38, no. 1, pp. 58–61, 1977.

[112] R. A. Nelson and M. G. Olsson, "The pendulum-rich physics from a simple system," *American Journal of Physics*, vol. 54, p. 112, 1986.

[113] L. D. Landau and E. M. Lifshitz, *Fluid Mechanics*. Pergamon, 1959.

[114] P. Alexander and E. Indelicato, "A semiempirical approach to a viscously damped oscillating sphere," *European Journal of Physics*, vol. 26, p. 1, 2005.

[115] J. J. Mendoza-Arenas, E. L. D. Perico, and F. Fajardo, "Motion of a damped oscillating sphere as a function of the medium viscosity," *European Journal of Physics*, vol. 31, p. 129, 2010.

[116] E. Guyon, J. P. Hulin, L. Petit, and C. D. Mitescu, *Physical hydrodynamics*. Oxford University Press, 2001.

[117] G. F. Pinton, J. J. Dahl, and G. E. Trahey, "Rapid tracking of small displacements with ultrasound," *IEEE Transactions on Ultrasonics, Ferroelectrics and Frequency Control*, vol. 53, no. 6, pp. 1103–1117, 2006.

[118] M. Urban and J. Greenleaf, "Harmonic pulsed excitation and motion detection of a vibrating reflective target," *The Journal of the Acoustical Society of America*, vol. 123, p. 519, 2008.

[119] J. E. Lenz, "A review of magnetic sensors," *Proceedings of the IEEE*, vol. 78, pp. 973–989, 1990.

[120] M. Sosa, A. A. O. Carneiro, O. Baffa, and J. F. Colafemina, "Human ear tympanum oscillation recorded using a magnetoresistive sensor," *Review of Scientific Instruments*, vol. 73, p. 3695, 2002.

[121] W. F. Walker, F. J. Fernandez, and L. A. Negron, "A method of imaging viscoelastic parameters with acoustic radiation force," *Physics in Medicine and Biology*, vol. 45, no. 6, pp. 1437–1448, 2000.

[122] S. G. Foster, P. M. Embree, W. D. O'Brien Jr, and M. Nicolet, "Flow velocity profile via time-domain correlation: error analysisand computer simulation," *IEEE Transactions on Ultrasonics, Ferroelectrics and Frequency Control*, vol. 37, no. 3, pp. 164–175, 1990.

[123] R. Boucher and J. Hassab, "Analysis of discrete implementation of generalized cross correlator," *IEEE Transactions on Acoustics, Speech and Signal Processing*, vol. 29, no. 3, pp. 609–611, 1981.

[124] Y. A. Ilinskii, G. D. Meegan, E. A. Zabolotskaya, and S. Y. Emelianov, "Gas bubble and solid sphere motion in elastic media in response to acoustic radiation force," *The Journal of the Acoustical Society of America*, vol. 117, p. 2338, 2005.

[125] J. Bercoff, M. Tanter, M. Muller, and M. Fink, "The role of viscosity in the impulse diffraction field of elastic waves induced by the acoustic radiation force," *IEEE Transactions on Ultrasonics, Ferroelectrics and Frequency Control*, vol. 51, no. 11, pp. 1523–1536, 2004.

Publications

Full length articles:

PAVAN, T.Z., MADSEN, E.L., JIANG, J.F., FRANK, G.R., CARNEIRO, A.A.O., HALL,T.J. Nonlinear elasticity phantom containing spherical inclusions, In preparation.

PAVAN, T.Z., ALMEIDA, T.W.J., CARNEIRO, A. A. O. Magnetic tracking of acoustic radiation force-induced micro-order displacement, IEEE Transactions on Ultrasonics, Ferroelectrics and Frequency Control. In Press.

CARNEIRO, J.A.O., PAVAN, T.Z., FUNABASHI, M., SANTOS-PONTELLI, T.E.G., COLAFEMINA, J.F., CARNEIRO, A.A.O. New software tool to assess the visual vertical perception. Journal of NeuroEngineering and Rehabilitation. In Review

KAMIMURA, H. A. S., PAVAN, T. Z., ALMEIDA, T. W. J., PADUA, M. L. A., BAGGIO, A. L., FATEMI, M., CARNEIRO, A. A. O. Pressure transducer for measuring acoustic radiation force based on a magnetic sensor. Measurement Science & Technology, v.22, p.015101(8pp), 2011.

PAVAN, T. Z., MADSEN,E.L., FRANK,G.R., CARNEIRO, A. A. O., HALL,T.J. Nonlinear elastic behavior of phantom materials for elastography. Physics in Medicine and Biology, v.55, p.2679 - 2692, 2010.

PAVAN, T. Z., NEVES, L. P., CARNEIRO, A. A. O. Elastografia por ultra-som: uma nova modalidade de imagem. Ciência Hoje. v.251, p.28 - 33, 2008.

PAVAN, T. Z., VIEIRA, S. L., CARNEIRO, A. A. O. Elastography: A New Ultrasound and MRI Procedure. AIP Conference Proceedings. v.1032, p.51 - 59, 2008.

Conference proceedings:

PAVAN, T. Z., MADSEN,E.L., JIANG, J.F., FRANK,G.R., CARNEIRO, A. A. O., HALL,T.J. Nonlinear elasticity phantom containing spherical inclusions undergoing large deformations In: 2010 IEEE International Ultrasonics Symposium, 2010, San Diego.

PAVAN, T. Z., CARNEIRO, A. A. O. Determinação de parâmetros viscoeláticos de tecidos moles através de excitação acústica focalizada e detecção por ultrassom pulso-eco In: XV Congresso Brasileiro de Física Médica, 2010, Aracaju.

PAVAN, T. Z., MADSEN,E.L., CARNEIRO, A. A. O., FRANK,G.R., HALL,T.J. Exploring the

nonlinear elastic behavior of phantom materials for elastography In: IEEE International Ultrasonics Symposium, 2009, Roma.

FUNABASHI, M, NAGHILA,N., WATANABE, L., SANTOS-PONTELLI, T.E.G., PAVAN, T. Z., CARNEIRO, A. A. O., COLAFEMINA, J. F. Análise da influência do colar cervical na avaliação da percepção de verticalidade visual In: XIX WORLD CONGRESS OF OTO-RHINO-LARYNGOLOGY, 2009, São Paulo.

PAVAN, T. Z., BAGGIO, A. L., CARNEIRO, A. A. O. Continuous wave Doppler ultrasound measurement of micro-vibrations induced by a focused acoustic radiation force In: 4th European Conference of the International Federation for Medical and Biological Engineering, 2008, Antwerp. IFMBE Proceedings. Berlin Heidelberg: Springer, 2008. v.22. p.852 - 855

PAVAN, T. Z., BAGGIO, A. L., FAGUNDES, M. A., CARNEIRO, A. A. O. Continuous wave doppler ultrasound interrogation of harmonic motion induced by focused acoustic radiation force In: Seventh International Conference on the Ultrasonic Measurement and Imaging of the Tissue Elasticity, 2008, Austin, TX, USA.

PAVAN, T. Z., BAGGIO, A. L., FAGUNDES, M. A., SIQUEIRA, R. B., CARNEIRO, A. A. O. Resolução espacial do sistema de imagem por vibro-acustografia focalizada In: 21 Congresso Brasileiro de Engenheria Biomédica, 2008, Salvador.

BAGGIO, A. L., PAVAN, T. Z., FAGUNDES, M. A., SIQUEIRA, R. B., CARNEIRO, A. A. O. Caracterização de um sistema de vibro-acustografia para o estudo de propriedades visco-elásticas de tecidos moles In: XXXI ENFMC, 2008, Águas de Lindoia.

PAVAN, T. Z., Carneiro AAO Estimativa da vibração harmônica dos tecidos por ultra-som pulso-eco In: III Simpósio de Instrumentação e Imagens Médicas, 2007, São Carlos.

Del Lama, L.S., PAVAN, T.Z., Mulato, M. Oscilador salino In: 15 Simpósio Internacional de Iniciação Científica da Universidade de São Paulo, 2007, Ribeirão Preto.

PAVAN, T.Z., TEDESCHI, W., COLAFEMINA, J.F., Carneiro A.A.O. Virtual apparatus to study the subjective visual vertical In: 3rd IEEE-EMBS International Summer School and Symposium on Medical Devices and Biosensors (ISSS-MDBS 2006), p.130 - f2, 2006, Boston-MIT.

PAVAN, T.Z., TEDESCHI, W., COLAFEMINA, J.F., Carneiro A.A.O., Estímulo virtual em estudos da subjetiva visual vertical In: XI Congesso de Física Médica, 2006, Ribeirão Preto.

PAVAN, T.Z., COLAFEMINA, J. F., TEDESCHI, W., ARAUJO, D.B., BAFFA, O., CARNEIRO, A.A.O. Método inovador para análise dos distúrbios da subjetiva visual vertical In: X Congresso Brasileiro de Física Médica, 2005, Salvador.

PAVAN, T.Z., COLAFEMINA, J.F., TEDESCHI, W., Carneiro A.A.O., Um método inovador para análise dos distúrbios da subjetiva visula vertical In: 13 SIICUSP, 2005, Ribeirão Preto.

PAVAN, T.Z., CARNEIRO, A.A.O., TEDESCHI, W., COLAFEMINA, J.F., ARAUJO, D.B., BAFFA FILHO, O. Desenvolvimento de um software para análise dos distúrbios da subjetiva visual vertical In: III Congresso Latino Ibero Americano e Região do Caribe de Física Médica e IX Congresso Brasileiro de Física Médica, 2004, Rio de Janeiro.

PAVAN, T.Z., COLAFEMINA, J.F., TEDESCHI, W., Carneiro A.A.O., Desenvolvimento de um software pra análise dos distúrbios da subjetiva visual vertical In: 12 SIICUSP(simpósio de iniciacão científica da usp), 2004, Ribeirão Preto.